RÉPUBLIQUE ALGÉRIENNE DÉMOCRATIQUE ET POPULAIRE

POPULAIREMINISTÈRE DE L'ENSEIGNEMENT SUPÉRIEUR ET DE LA RECHERCHE SCIENTIFIQUE

UNIVERSITÉ D'ECHAHID HAMMA LAKHDAR - EL OUED

Faculté de Technologie

Laboratoire d'Exploitation et de Valorisation des Ressources Energétiques Sahariennes (LEVRES)

Thèse de Doctorat

Présentée par: **ABDELHALIM ARIF**

En vue l'obtention du diplôme de **DOCTORAT LMD** en:

Option: **Électrotechnique**

Intitulé

Analyse de la tenue aux creux de tension d'un système éolien connecté au réseau par des techniques avancées

Soutenue le 29/02/ 2024, devant le jury composé de:

Laid Zellouma	Professeur	Université d'El Oued	Président
Youcef Bekakra	Professeur	Université d'E Oued	Directeur de Thèse
Djilani Ben attous	Professeur	Université d'E Oued	Co-Directeur de Thèse
Mohammed Toufik Ben Chouia	Professeur	Université de Biskra	Examinateur
Rabhi Boualaga	Professeur	Université de Biskra	Examinateur
Zakaria Lammouchi	MCA	Université d'El Oued	Examinateur

Année Universitaire 2023/2024

PEOPLE'S DEMOCRATIC REPUBLIC OF ALGERIA

MINISTRY OF HIGHER EDUCATION AND SCIENTIFIC RESEARCH

UNIVERSITY OF ECHAHID HAMMA LAKHDAR - EL OUED

Faculty of Technology

Laboratory for the exploitation and development of Saharan Energy Resources (LEVRES)

Doctoral Thesis

Submitted by: **ABDELHALIM ARIF**

In order to obtain the **LMD DOCTORATE** degree in:

Option: **Electrotechnics**

Entitled

Analysis of the Voltage Dip withstand of a Wind Turbine System connected to the Grid by Advanced Techniques

Defended on 29/02/ 2024, before the jury composed of:

Laid Zellouma	Professor	University of El Oued	President
Youcef Bekakra	Professor	University of El Oued	Supervisor
Djilani Ben attous	Professor	University of El Oued	Co- Supervisor
Mohammed Toufik Ben Chouia	Professor	University of Biskra	Examiner
Rabhi Boualaga	Professor	University of Biskra	Examiner
Zakaria Lammouchi	MCA	University of El Oued	Examiner

University Year 2023/2024

إهداء

بسم الله والصلاة والسلام على حبيبي رسول الله

أولا شكرا لله على توفيقه وامتنانه للوصول إلى هذه المرحلة

إلى من أحب وأعزّ، شكرًا من القلب لعائلتي الغالية وأخص بالذكر أمي وأبي وأصدقائي الأعزاء الذين كانوا دائمًا بجانبي، يقدمون لي الدعم المعنوي والعاطفي. شكرًا لمشرفي أ.د. يوسف بكاكره وأ.د. الجيلاني بن عتوس وأساتذتي الرائعين الذين شاركوني معرفتهم وخبرتهم وأشرفوا على تطوري الأكاديمي. إنه لشرف كبير أن أكون جزءًا من هذا البيئة الأكاديمية الملهمة. هذه المذكرة تعكس جهدي وعطائي لتقديم شيء يسهم في مجال البحث والمعرفة. أهدي هذا البحث المتواضع، راجيا من الله عز وعلا أن يجعلها ثمرة خير ينتفع بها طلبة العلم.

Thanks

Firstly, thanks to God -ALLAH- for his success and gratitude in reaching this stage. I would like to thank my dear family, especially my mother, father, and dear friends who were always by my side, providing me with moral and emotional support. I express my gratitude to my wonderful professors who generously shared their knowledge and experience with me, overseeing my academic development. I would like to extend special thanks to my supervisors, **Pr. Youcef Bekakra** and **Pr. Djilani Ben Attous**, both esteemed professors at the University of El Oued, for guiding me in the creation of this humble work. My sincere hope is that it will prove beneficial to both the people and the country. Additionally, I would like to thank the jury for accepting this invitation and for evaluating my work.

ملخص

Abstract

تحليل مقاومة انخفاض الجهد لنظام توربين رياح متصل بالشبكة بتقنيات متقدمة

ملخص:

في إطار البحث عن مصادر جديدة وبديلة للطاقة الكهربائية، تحظى طاقة الرياح بأهمية كبيرة نظرا لطبيعتها المتجددة والنظيفة. ومع ذلك، فإن توربينات الرياح القائمة على DFIG تكون حساسة للغاية لاضطرابات الشبكة، مما يؤثر سلبًا على كل من DFIG ودوائر التحكم الإلكترونية المرتبطة به. لذلك، تقدم هذه الأطروحة تحليلاً يعتمد على انخفاضات الجهد لنظام وتوربينات الرياح المتصلة بالشبكة. في البداية قمنا بدراسة النماذج الرياضية لـ DFIG والتحكم في ناقلاتها باستخدام جهاز التحكم PI، وتوربينات الرياح مع التحكم بها باستخدام MPPT. أشارت نتائج الأبحاث إلى أنه على الرغم من فعالية وحدة التحكم PI في الأنظمة الخطية ذات الطبيعة المتسقة، إلا أنها تفتقر إلى المتانة والكفاءة في الأنظمة غير الخطية التي تتميز بالتقلب والاضطرابات. ولمواجهة هذا التحدي، تم اقتراح نهج التحكم الخلفي. هذا النهج مناسب بشكل خاص للأنظمة غير الخطية بسبب بنيته العودية. يستخدم عنصر تحكم افتراضي يعتمد على دالة Lyapunov لتبسيط تعقيدات مشاكل التحكم غير الخطية. بعد ذلك قمنا بدراسة التحكم الضبابي والذي يوفر حل تقريبي للأنظمة غير الخطية ويقلل من الضوضاء الناتجة عن النظام بالإضافة إلى تعزيز المتانة والاستقرار. على الرغم من المزايا التي تقدمها BSC وFLC، فقد تم اقتراح تقنية تحكم هجينة تسمى FBSC للجمع بينهما. تقوم هذه التقنية بتجميع نقاط القوة لكل من BSC وFLC، بهدف توفير حل تقريبي للأنظمة غير الخطية المعقدة وغير المؤكدة باستخدام عنصر تحكم غامض افتراضي، مسترشدًا بدالة Lyapunov لتبسيط المعلمات الغامضة. تم تطبيق هذه التقنية لتعزيز التحكم في دوار DFIG; يكمن التعزيز في تحقيق تموجات أقل للقوى النشطة والتفاعلية للجزء الثابت، وتقليل التشوه التوافقي الكلي (THD) لتيارات الجزء الثابت، والمتانة ضد اختلافات المعلمات. بعد ذلك، تعرض DFIG لانخفاضات الجهد المتماثلة وغير المتماثلة للشبكة الكهربائية، مما أدى إلى تيارات زائدة للجزء الثابت والدوار. ومع ذلك، فقد ثبت أن الانخفاضات غير المتماثلة أكثر ضررًا من الانخفاضات المتماثلة، وذلك بسبب التذبذبات المحمولة على تيارات الجزء الدوار، والتي تتوافق مع زيادة كبيرة في THD، والتموجات العالية للقوى النشطة والتفاعلية للجزء الثابت. ولمعالجة هذه المشكلة، تم اقتراح أداة استعادة الجهد الديناميكي (DVR) لاستعادة جهد الشبكة، مما توفر نتائج جيدة تقريبًا كما كانت قبل حدوث الانخفاضات. في جوهر الأمر، يوفر الجمع بين التحكم الأمثل في DFIG وDVR حلاً موثوقًا وقويًا للحفاظ على جودة الطاقة واستقرارها داخل أنظمة الطاقة.

كلمات مفتاحية:

توربينات الرياح، مولد حثي مزدوج التغذية، التحكم في الخطوة الخلفية، التحكم المنطقي الغامض، التحكم في الخطوة الخلفية الغامضة، انخفاض جهد الشبكة، مُستعيد الجهد الديناميكي.

Analysis of the Voltage Dip withstand of a Wind Turbine System connected to the Grid by Advanced Techniques

Abstract:

In the context of seeking new and alternative energy sources, wind energy is of significant importance due to its renewable and clean nature. However, the wind turbines based on DFIG are highly sensitive to grid disturbances, which negatively affect both the DFIG and its associated electronic control circuits. Therefore, this thesis presents an analysis based on voltage dips for a grid-connected wind turbine system. Initially, we studied the mathematical models of DFIG and its vector control using PI controller, and the wind turbine with its control using MPPT. Research has indicated that while PI controller is effective for linear systems with a consistent nature, it lacks robustness and efficiency in nonlinear systems characterized by variability and disturbances. To address this challenge, the Backstepping control approach has been suggested. This approach is particularly suitable for nonlinear systems due to its recursive structure. It employs a virtual control element based on the Lyapunov function to streamline the complexities of nonlinear control problems. Afterwards, we examined fuzzy control, which provides an approximate solution for nonlinear systems and reduces the noise generated by the system, in addition to enhancing robustness and stability. Despite the advantages offered by BSC and FLC, a hybrid control technology called FBSC has been proposed to combine them. This technique synthesizes the strengths of both BSC and FLC, aimed at providing an approximate solution for complex and uncertain nonlinear systems using a virtual fuzzy control element, guided by the Lyapunov function to simplify fuzzy parameters. This technique was applied to enhance the control of DFIG's rotor. The enhancement lies in achieving lower ripples of stator active and reactive powers, reduced total harmonic distortion (THD) of the stator currents, and robustness against parameter variations. Subsequently, the DFIG was subjected to both symmetrical and asymmetrical voltage dips, which led to stator and rotor overcurrents. However, it has been shown that asymmetrical dips are more harmful than symmetrical dips due to the oscillations carried on the rotor currents, which correspond to a significant increase in THD, and high ripples of the stator active and reactive powers. To address this

problem, a Dynamic Voltage Restorer (DVR) was proposed to restore the grid voltage, which provides results almost as good as before the dips occurred. In essence, the combination of optimized DFIG control and DVR provides a reliable and robust solution for maintaining energy quality and stability within power systems.

Keywords:

Wind Turbine, Doubly Fed Induction Generator, Backstepping Control, Fuzzy Logic Control, Fuzzy Backstepping Control, Grid Voltage Dip, Dynamic Voltage Restorer.

Table of Contents

General Introduction

Chapter I:

State of the Art of the Wind Generator

Chapter II:

Wind Turbine Conversion System Modeling and Control based on DFIM

Chapter III:

Advanced Control of DFIG using Backstepping Control

Chapter IV:

Robust Control of DFIG using Fuzzy Logic Control

Chapter V:

Voltage Dips of DFIG with Dynamic Voltage Restorer

Table of Figures and Tables

Table of Figures

Table of Tables

Notations and Symbols

Notations and Symbols

Notations and Acronyms :

AC	Alternative Current
BSC	Backstepping Controller
CLTF	Closed Loop Transform Function
DC	Direct Current
DFIG	Doubly Fed Induction Generator
DFIM	Doubly Fed Induction Machine
DPC	Direct Power Control
DVR	Dynamic Voltage Restorer
FBSC	Fuzzy Backstepping Controller
FLC	Fuzzy Logic Controller
FOC	Field-Oriented Control
GSC	Grid Side Converter
HVC	Hysteresis Voltage Control
IDPC	Indirect Power Control
MPPT	Maximum Power Point Tracking
OLTF	Open Loop Transform Function
PI	Proportional Integral
PWM	Pulse Width Modulation
RSC	Rotor Side Converter
SVM	Space Vector Modulation
SVPWM	Space Vector Pulse Width Modulation
THD	Total Harmonic Distortion
VC	Vector Control
WT	Wind Turbine

Symbols:

Turbine:

β	Blade orientation angle
C_p	Power coefficient

$C_{p\text{-}max}$	Maximum power coefficient
T_{tur}	Turbine torque
T_g	Generator torque
T_{em}	Electromagnetic torque
$T_{em\text{-}ref}$	Reference electromagnetic torque
ρ	Air density
G	Multiplier gain
J_{tur}	Turbine inertia
J_g	Generator inertia
R	Blade length
P_{aer}	Aerodynamic power
$P_{aer\text{-}ref}$	Reference aerodynamic power
P_w	Wind power
λ	Tip speed ratio
S	Circular surface swept by the turbine
λ_{opt}	Optimum value of tip speed ratio
Ω_{tur}	Turbine speed
Ω_{mec}	Generator shaft speed
v	Wind speed
v_{est}	Estimated wind speed

DFIG:

P_s, Q_s	Stator active and reactive powers
P_r, Q_r	Rotor active and reactive powers
V_{sdq}, V_{rdq}	Stator and rotor voltages of (d q)-axis
I_{sdq}, I_{rdq}	Stator and rotor currents of (d q)-axis
ϕ_{sdq}, ϕ_{rdq}	Stator and rotor flux of (d, q)-axis
R_s, R_r	Stator and rotor resistance
L_s, L_r	Stator and rotor inductance
w_s, w_r	Stator and rotor angular frequency

M	Mutual induction
T_s, T_r	Stator and rotor time constant
σ	Dispersion coefficient
g	Slip coefficient between stator and rotor
T_{em}	Electromagnetic torque
θ_s, θ_r	Angle of stator and rotor
P	Number of pole pairs
f	Coefficient of friction
J	Moment of inertia
K_i	Integral gain
K_p	Proportional gain
U_C	DC bus voltage
f_s, f_r	Stator and rotor frequency
[P]	Park's transformation matrix
$[V_{sa}\ V_{sb}\ V_{sc}]^T$	Stator voltage vectors of (a b c)-axis
$[V_{ra}\ V_{rb}\ V_{rc}]^T$	Rotor voltage vectors of (a b c)-axis
$[I_{sa}\ I_{sb}\ I_{sc}]^T$	Stator current vectors of (a b c)-axis
$[I_{ra}\ I_{rb}\ I_{rc}]^T$	Rotor current vectors of (a b c)-axis
$[\phi_{sa}\ \phi_{sb}\ \phi_{sc}]^T$	Stator flux vectors of (a b c)-axis
$[\phi_{ra}\ \phi_{rb}\ \phi_{rc}]^T$	Rotor flux vectors of (a b c)-axis

FLC and BSC:

e_{Irdq}	Error of rotor current
Δe_{Irdq}	Error change of rotor current
ΔV^*_{rdq}	Change of reference rotor voltage
K_e	Error constant gain
$K_{\Delta e}$	Constant gain of error change
$K_{\Delta V}$	Constant gain of voltage change
k_1, k_2, k_3, k_4	Positive constants of Lyapunov function

General Introduction

Concerns over the depletion of fossil fuels and their negative environmental impacts have led to a growing interest in renewable energy sources. Wind power, in particular, has been recognized as a clean and sustainable alternative energy source for over a century [Yu 18], owing to its cleanliness, vast and freely available natural resources, and minimal impact on the environment. These factors have contributed to the increased reliability and popularity of wind power. [Art 19]. However, the total wind power reached about 520 GW at the end of 2007, of this, 18 GW was extracted over the sea, especially the leading and innovative European countries in this field. Operation and maintenance are very necessary to ensure the survival continuity of wind turbines (WTs). However, the associated costs are high, which makes it up to about 25% of the total wind farm costs, as this percentage varies, rising to 35% in the case of maintaining and operating large and advanced offshore wind turbines [Yu 18]. Machines utilizing doubly fed induction generators (DFIG) have gained popularity for their ability to adapt to changing wind speeds. These systems employ a slip induction machine as a generator, with the stator directly connected to the grid and the rotor controlled by a back-to-back converter linked between the rotor and the grid [Lop 08]. To maximize the utilization of wind energy, WTs should be directed to track the maximum power points at varying wind speeds. The rotor speed of DFIG should vary widely to extract the maximum energy possible in region 2. Several maximum power point tracking technologies have been developed, which can be categorized into three types: optimal tip speed ratio (TSR), power signal feedback (PSF), and hill-climbing search (HCS) techniques [Bai 15]. In region 3 (full-load), the blade pitch angle is regulated to mitigate the effect of wind speed, which can exceed the maximum rated speed. To ensure power point tracking efficiency and avoid exceeding the rated power of the generator, the aerodynamic energy applied to the blade is reduced along with the excess power [Fat 15]. After the DFIG is connected to an electrical grid, a strategy must be employed to achieve independent control between active and reactive powers. This is accomplished by using stator flux orientation along the d-axis of the (d, q) reference frame, while setting the quadratic component (q-axis) of the stator flux to zero [Hach 20]. Vector control is a widely used technique for controlling electrical machines. It is based on the fact that the machine is similar to a DC machine with separate excitation, which ensures natural decoupling between currents and flux. Vector control (VC) is used for modeling the DFIG and power control. There are two types of VC: direct field-oriented control (DFOC) and indirect field-

oriented control (IFOC) [Boude 19]. The DFOC and IFOC both utilize a PI controller, with gains calculated from machine parameters. The classical PI controller based on VC is commonly used for controlling linear systems, but it has limitations when controlling nonlinear systems such as loss of robustness and slow response, along with high ripple. To address these issues, an advanced control technique called backstepping control (BSC) is proposed as an effective control technique for nonlinear systems. BSC simplifies the complexity of nonlinear control problems by using a virtual control element, and it achieves this through the use of a Lyapunov function and appropriate control elements to ensure better system stability and tracking of the reference signal [Men 17]. Fuzzy logic control (FLC) provides approximate solutions for complex nonlinear systems and eliminates spurious signals emitted by the system, this robust technology is based on three basic stages, arranged as follows: firstly, fuzzification stage, secondly, the stage of inference rules that based on linguistic variables using the rule (if … then) and logical operations (and, or,..), finally defuzzification stage.

DFIG-based WTs are very sensitive to grid disturbances, for example voltage dips, therefore, a sudden drop in some or all phases of the grid voltage causes overcurrent and overvoltage of the rotor windings, which may lead to damage to the control devices installed at level of the rotor, and separation of the WT from the grid. For example, 2,800 MW of wind-origin power in Spain was disconnected on November 4, 2006 due to a European outage [Lop 08]. There are two types of voltage dips, which are symmetrical and asymmetrical voltage dips, they are of varying severity when they affect DFIG and its electronic inverter, which makes asymmetrical voltage dips more dangerous than symmetrical dips. To solve this problem on the grid voltage, a technique to restore and recover the lost voltage called dynamic voltage restorer (DVR) has been proposed. DVR technique is connected in series between grid and DFIG, which is used to restore the grid voltage dips of some or all phases of grid voltage, using AC voltage in series. This technology is characterized using economical energy storage to compensate the occur voltage dip [Moh 13]. In short, the main objective of our work is to improve the control of the rotor of DFIG and DVR to obtain clean and available electrical energy without interruption. Therefore, this research is divided into five chapters. In the first chapter, the general form of the wind turbine based on DFIG was studied, and its components and types were studied, with a brief mention of its advantage and disadvantages. In the second chapter, a wind turbine model was presented, and its block diagram was presented without and with MPPT strategy and their equivalent on MATLAB/Simulink. A model of DFIG

was also presented with the direct and indirect power control using PI controller, and the block diagram was presented for them, at chapter end, the simulations results of wind speed and mechanical speed of WT with MPPT strategy were presented, in addition to the stator active and reactive power and stator and rotor currents using DPC-PI and IDPC-PI, and ensure their validity. In the third chapter, modeling of DPC and IDPC using BSC, and the block scheme for them is presented, simulation results of active and reactive power, stator and rotor currents using DPC-PI and IDPC-PI are also presented to verify their robustness and validity. In the fourth chapter, principle and general structure of FLC are studied, with details of its basic elements. The scheme of general model and rule surface, and the inference matrix of FLC, were also given, in addition to the comparison of simulation results between FLC-SVPWM and FLC-PWM of active and reactive power, stator and rotor currents are also presented to verify their robustness and validity. In the fifth chapter, a model of DFIG under symmetrical and asymmetrical voltage dips are given, after that, DVR strategy was studied for grid voltage restoration, with the general and detailed model scheme was presented for it. Initially, the simulation results of stator active and reactive powers, as well as stator and rotor currents under a variable-speed wind turbine, are presented using PI controller and FLC to control the rotor of DFIG under symmetrical and asymmetrical voltage dips without and with DVR. Afterward, the simulation results of stator active and reactive powers, as well as stator and rotor currents under a fixed-speed WT are presented using a PI controller, BSC and FBSC to control the rotor of DFIG under asymmetrical voltage dips without and with DVR. The contribution of the latter is listed as follows:

- The proposed FBSC exhibits a faster response in the presence of stator active power variations and achieves reduced ripples in both stator active and reactive powers compared to BSC, and PI controller.
- The FBSC demonstrates robustness against parameter variations, outperforming other control techniques in terms of maintaining stable performance despite changes in system parameters.
- The THD of stator currents is minimized using the proposed FBSC compared with the other control methods (BSC, PI controller), which improves the power quality.
- Restoring the grid voltage that suffers from asymmetrical dips using a DVR, which results reduction and return of stator and rotor overcurrents to their nominal values

Chapter I

State of the Art of the Wind Generator

I.1 Introduction

Wind energy plays a significant role in producing clean, carbon-neutral, and sustainable energy. WTs based on DFIG are currently the most widely used, particularly in areas with variable wind speeds. This is due to their ability to be easily controlled during varying wind speeds, ease of connection to the public grid, stable power output, and simple maintenance requirements [Als 18]. The working principle of WT driven by wind current is based on rotating the rotor of DFIG to obtain electrical energy in the stator. WTs can be divided into two main types in terms of wind speed: a WT driven by a fixed speed, and a WT driven by a variable speed. Among the advantages of variable speed WTs compared to conventional fixed-speed WTs are that they can reduce fluctuation in electrical energy and increase energy capture, enhancing the dynamic behavior caused by mitigating mechanical stress. Such advantages contribute to improving the quantity and quality of energy generated [Idr 19]. DFIG is one of the most used generators for generating electrical energy, because it has several advantages, including that the speed of the rotor of this generator is directly proportional to the wind speed, with the frequency and amplitude of the voltage unchanged, which is obtained in the stator connected directly to the electrical grid whereas the rotor is connected by back-to-back converter (RSC- DC Link-GSC), this converter is controlled by the proposed control approach [Oua 20], as well as, DFIG operates over a range of ±30% around synchronous speed, and that's by controlling its rotor using a back-to-back converter, This results in 100% of the total power, 30% of this power is absorbed by the rotor, As for 70% of the remaining power is stored directly in the grid ,with a stored stator voltage free of harmonics [Azz 17]. In this chapter, the types of WTs and their constituent components will be presented as well as the technical state of electromagnetic conversion. Next, the operating modes of the doubly fed induction machine (DFIM), associated with back-to-back converters, will be studied, in addition to operating principle, advantages and disadvantages of DFIG [Azz 17].

I.2 The Wind Generator

The wind generator, also commonly known as a wind turbine, functions by harnessing the movement of air and converting it into mechanical energy, which then passes through a generator to produce electrical energy. The type of generator used in this turbine is the DFIG, and the process of converting wind kinetic energy into electrical energy is illustrated in Figure I.1 [Mak 15].

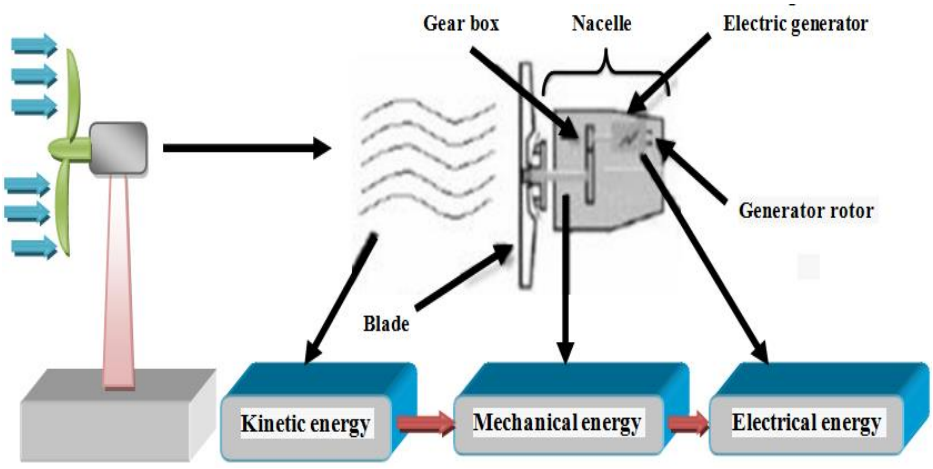

Figure I.1 Conversion of wind kinetic energy into electrical energy

The WTs are classified into three categories based on the amount of energy they generate:

- Low-Power WTs: those with a rated power output of less than 40 kW.
- Medium-Power WTs: those with a rated power output ranging from 40 kW to a few hundred kW.
- High-Power WTs: those with a rated power output greater than 1 MW.

The previous growth of small WTs, with capacities ranging between 20-60 KW, was not sufficient to meet the needs of the electrical network. These turbines were located close to the surface of the earth, which limited their access to wind currents and made them susceptible to fluctuations. To ensure a steady supply of wind and avoid interruptions, it was necessary to raise these turbines on towers that are commensurate with their diameter. Over time, these turbines have significantly increased in size, with a diameter of up to 252 m in 2020 and a capacity ranging from 10 to 20 MW. This growth has contributed to the recovery of the grid, as well as the development of foreign markets and exports. Figure I.2 illustrates the growth in the size and capacity of wind turbines from 1980 to 2020.

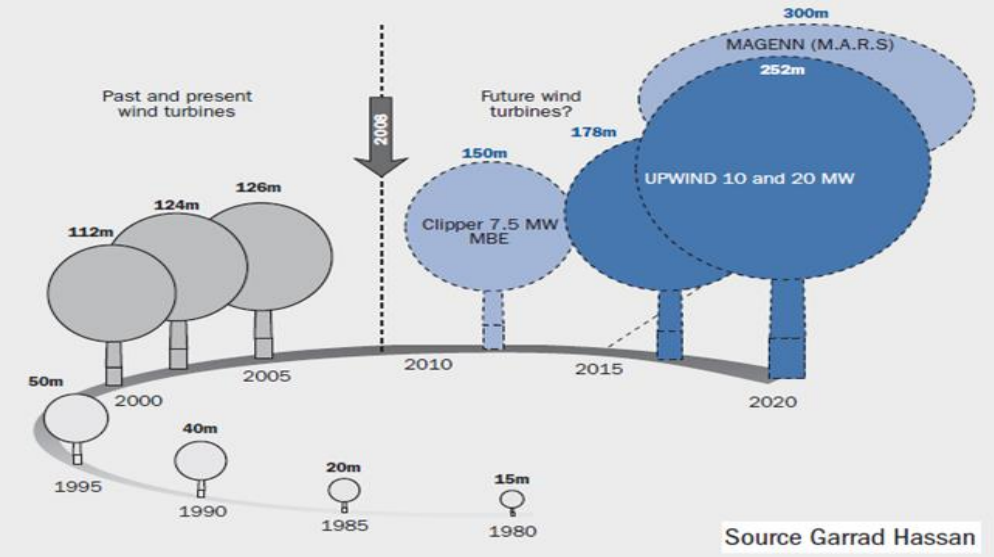

Figure I.2 Size-power correspondence of WTs

I.2.1 The wind

Wind currents are created due to variations in temperature caused by the sun, leading to alterations in air pressure. As shown in Figure I.3.a, the sun heats up the seas, oceans, and lands, but not uniformly, as depicted in Figure I.3.b. The heated surface subsequently warms up the air layer above it, causing the air volume to expand, as demonstrated in Figure I.3.c. This, in turn, results in the movement of air molecules, as illustrated in Figure I.3.d. WTs capture the kinetic energy of air particles, thus generating wind energy.

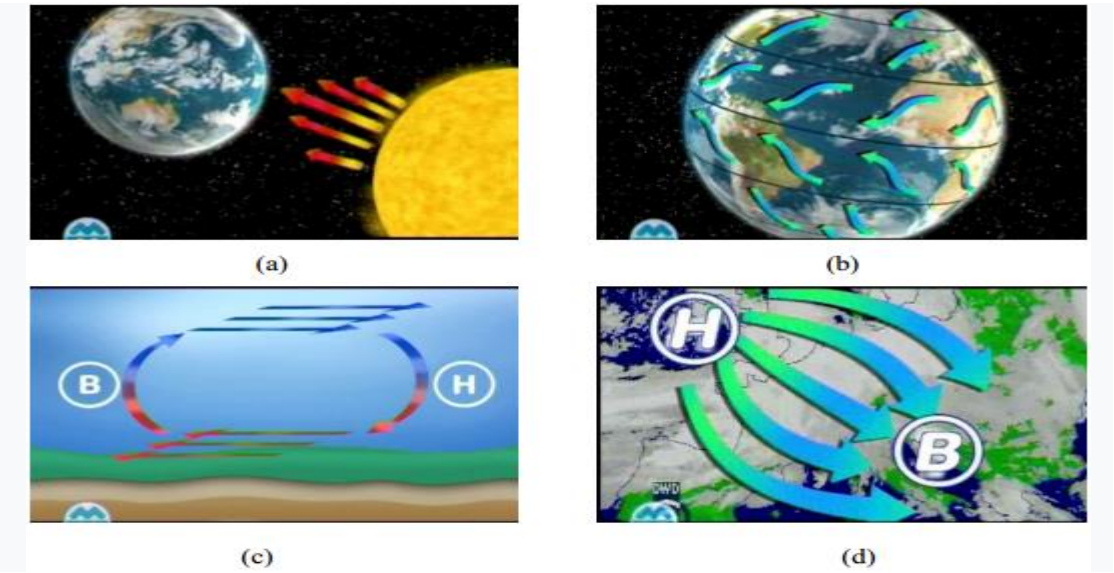

Figure I.3 The birth of the wind

I.3 Types of wind turbine

WTs have the ability to rotate around either a horizontal or a vertical axis, with the former being the more conventional and more common.

I.3.1 The horizontal axis wind turbine

Large three-bladed horizontal-axis WTs (HAWTs) that position the blades upwind of the tower are responsible for the majority of wind power generated worldwide. These turbines feature the main rotor shaft and electrical generator at the top of a tower and require orientation towards the wind. While small turbines use a wind vane for direction, larger turbines typically rely on a wind sensor and yaw system. Most turbines incorporate a gearbox to transform the slow blade rotation into a more rapid motion that can power an electrical generator. However, some turbines use a direct-drive generator that eliminates the need for a gearbox and connects the rotor directly to the generator. Although direct-drive generators that use rare earth materials may be more expensive, they are sometimes preferred over gearbox generators because they eliminate gear-speed increaser-related fatigue torque loading and associated reliability and maintenance costs [Sad 22]. HAWTs are typically oriented into the wind by employing a directional control mechanism or by utilizing the natural dynamic balance phenomenon facilitated by a rudder installed on the turbine facing the wind.

Figure I.4 The horizontal axis WT

Advantages of HAWTs

- Variable blade pitch adjusts the angle of attack to optimize turbine blade performance.
- Changing the angle of attack provides greater control over power generation, enabling maximum efficiency.
- HAWTs feature tall towers, which provide access to higher wind speeds as wind energy increases with height. In some cases, increasing the tower height by just 10 meters can lead to a 20% increase in wind speed.
- HAWT blades rotate horizontally, perpendicular to the wind, resulting in minimal drag and consistent power generation throughout rotation.

Drawbacks of HAWTs

- High construction and transportation costs due to the large size of the turbines.
- Expensive civil construction due to the erection of large towers.
- Production of electronic noise during turbine operation, which can interfere with radar sites.
- Turbulence generated in downwind HAWTs may lead to structural failure.
- HAWTs require an additional yaw control mechanism to turn the blades towards the wind.

I.3.2 The Vertical axis wind turbine

Vertical axis WTs (VAWTs) have their main rotor shaft arranged in a vertical position, providing certain advantages. One advantage is that it does not need to be pointed directly into the wind to be effective, which is beneficial in areas where wind direction is highly variable. It is also advantageous for integration into buildings since it is less steerable. In addition, placing the generator and gearbox near the ground allows for a direct drive from the rotor assembly, making maintenance more accessible. However, this type of turbine generally produces less energy when calculating the average total energy over time [Sad 22]. VAWTs can be divided in two main categories: The first type of VAWT is the Savonius vertical WT, which is named after its inventor, Finnish engineer Sigurd Johannes Savonius, who received a patent in the U.S. in 1925 [Joh 26], Aerodynamically, the device is a drag-type turbine consisting of two or three scoops. When viewed from above [Sur 19], the two-scoop turbine has an "S" shape in cross-section due to its curvature. The scoops experience less drag when moving against the wind than when moving with the wind, which creates a differential drag and causes the Savonius turbine to rotate. Although the

turbine operates smoothly with wind speeds, it generally extracts less wind energy due to the low wind speeds found at low altitudes near the ground. This is because it has a short holder without an extended column as shown in Figure I.5 (a). The resulting torque causes the assembly to rotate, which is generated by the circulation of air between two cylinders and increases the engine's torque. The main advantages of this model are [Cas 19]:

- constructive simplicity.
- cheap initial and maintenance costs.
- low vision impact for urban applications.
- startup with low wind speed independent of the wind direction high torque.

The second type of VAWT is the Darrieus WT, which is represented in Figure 1b-d. This turbine uses blades with an airfoil shape, typically three, that generate lift force to rotate the main shaft. The rotor of Darrieus turbines can have various configurations such as "egg beater", H-shape, or helical shape.

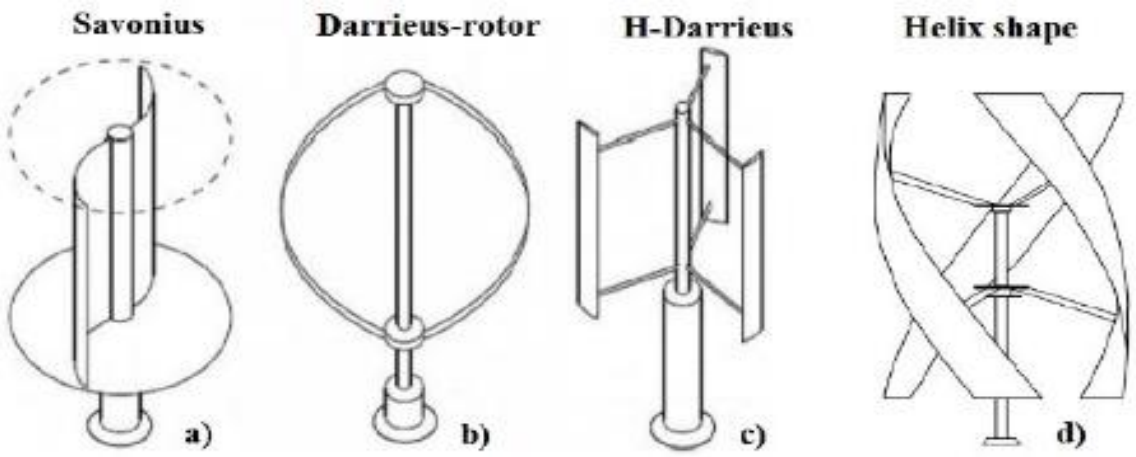

Figure I.5 Different kinds of VAWT: (a) Savonius (b) Darrieus with “egg beater” design rotor (c) H-shape blades; (d) helix shape blades

Advantages of VAWTs:

- A massive tower structure is not necessary for VAWTs as they can be mounted closer to the ground.
- VAWTs also do not require yaw mechanisms.
- VAWTs are located closer to the ground, which makes them easier to maintain.
- VAWTs have lower startup speeds compared to HAWTs and can start at speeds as low as 10 km/h.
- Additionally, VAWTs have a lower noise signature.

Drawbacks of VAWTs:

- VAWTs have lower efficiency than HAWTs due to the additional drag produced by the rotation of blades.
- Despite being located closer to the ground, the equipment for VAWTs now resides at the bottom of the turbine's structure, making it inaccessible.
- Due to their low height, VAWTs cannot capture the wind energy stored at higher altitudes.

I.4 Regulation of the Mechanical Power of a Wind Turbine:

WTs are designed to produce significant amounts of electrical energy by making maximum use of wind energy. However, at high wind speeds, it is necessary to dissipate some of the excess wind energy to avoid damaging the WTs. Therefore, controllers are designed to regulate the mechanical power of WTs, which goes through three phases as shown in Figure I.6 [Luo 14].

- The first stage is divided into two parts: the starting part (before the wind speed reaches ($v_{cut\text{-}in}$), in which the rotational speed is zero and P=0 (the turbine is not working); and a part after starting (the wind speed between $v_{cut\text{-}in}$ and v_{rmax}), where the rotational speed is weak in a non-linear system. This behavior represents a major obstacle to the performance of the control task.
- The second stage occurs when the wind speed is between v_{rmax} and v_{rated}. During this stage, the power generated by the turbine depends on the wind speed and follows a linear system.
- The third stage (the wind speed between v_{rated} and $v_{cut\text{-}off}$) is characterized by a power generated by the turbine is always equal to P_n.

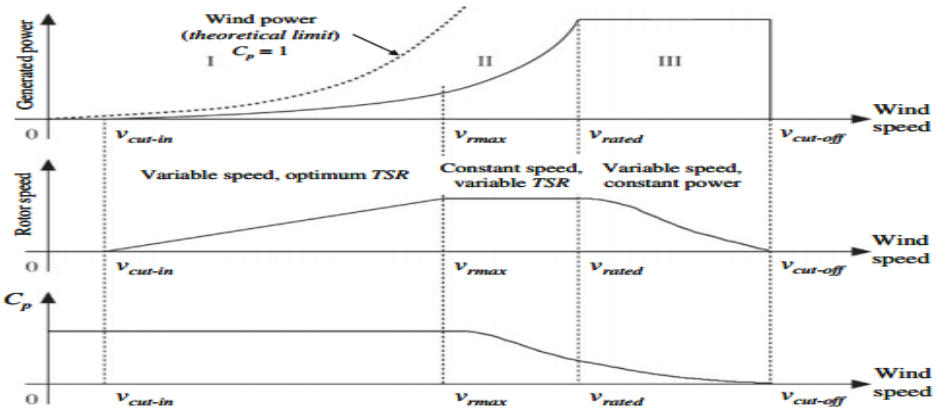

Figure I.6 Diagram of mechanical power, rotor speed and C_p as a function of wind speed

I.5 Wind Energy Assessment in Algeria:

Algeria is located in North Africa, south of the Mediterranean Sea (1200 km), and is known for its diverse terrain that spans over 2 million km². Algeria is divided into several regions based on its geography, including the Sahel, Atlas Tellien, upper plateaus, north of Sahara, and the big Sahara. The geography and weather conditions of Algeria are conducive to abundant renewable energy resources, particularly wind energy. Numerous studies have been conducted to identify wind energy potential and speed in various areas, as depicted in Figure I.7 [Ber 19].

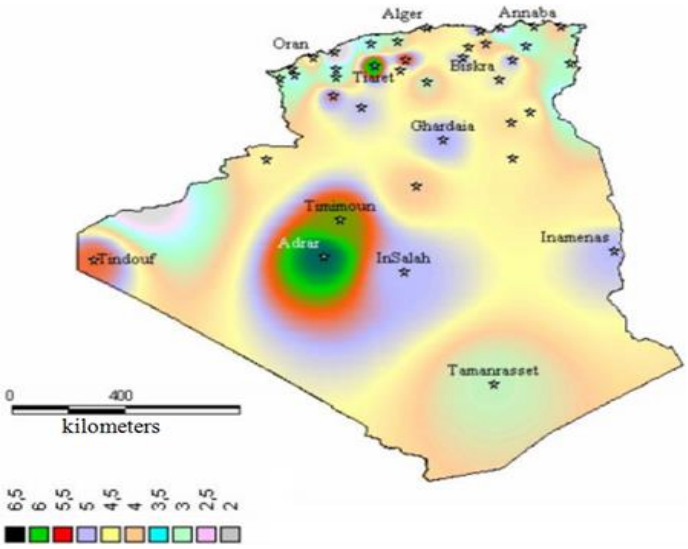

Figure I.7 Wind distribution map for some selected regions in Algeria

I.6 Main Components of a Horizontal Axis Wind Turbine

HAWTs are based on traditional windmill designs that have been in use for centuries. The turbine tower supports a nacelle which is installed perpendicular to the tower and horizontal in relation to the ground, displaying the name of the turbine. Among the most widely used models for harnessing wind energy, HAWTs offer numerous advantages [Saa 14]. The key components of a horizontal wind turbine are illustrated below:

- The main rotor shaft
- The electrical generator
- The gearbox to increase the rotation speed of the blades
- Turbine blades, with stiffness to avoid contacting the post

A wind vane is utilized to orient the turbines, while a wind sensor is integrated for a HAWT. The various components of HAWT are illustrated in Figure I.8.

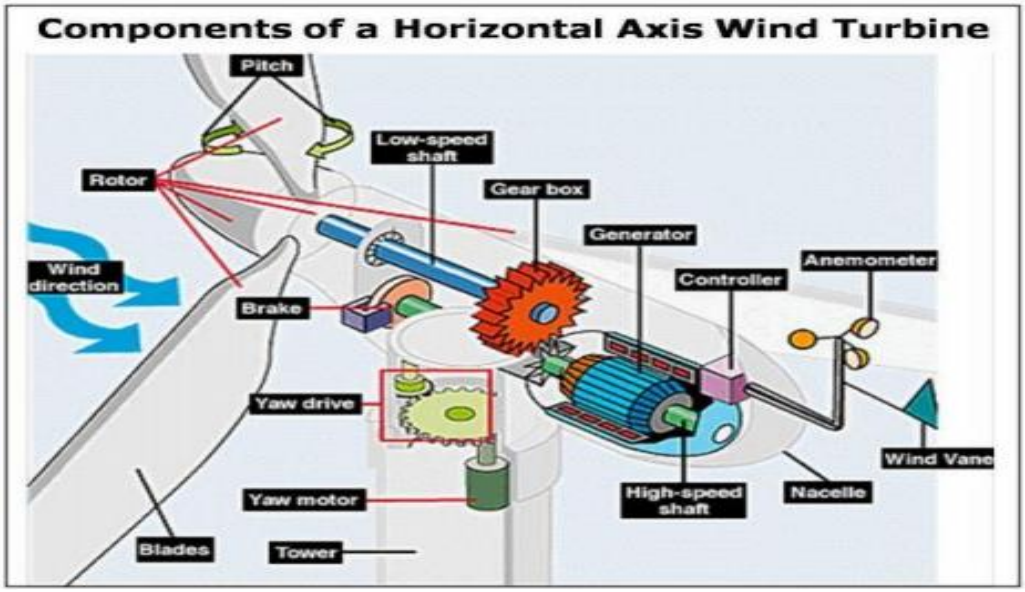

Figure I.8 Components of Horizontal Axis Wind Turbine

I.7 State of the Art on Electromechanical Conversion:

In previous years, the most prevalent type of WT utilized for generating electrical energy at a constant speed was equipped with Squirrel Cage Induction Generator (SCIG), which achieves maximum efficiency only at a certain speed. Regardless of any variations in wind speed, the rotor speed of WT remains constant and is determined by the gear ratio, frequency of the supply network, and generator design. Fixed speed WTs are connected directly to the grid without the need for inverters or compensating batteries connected in parallel, resulting in low cost, reliability, and ease of installation of electrical components.

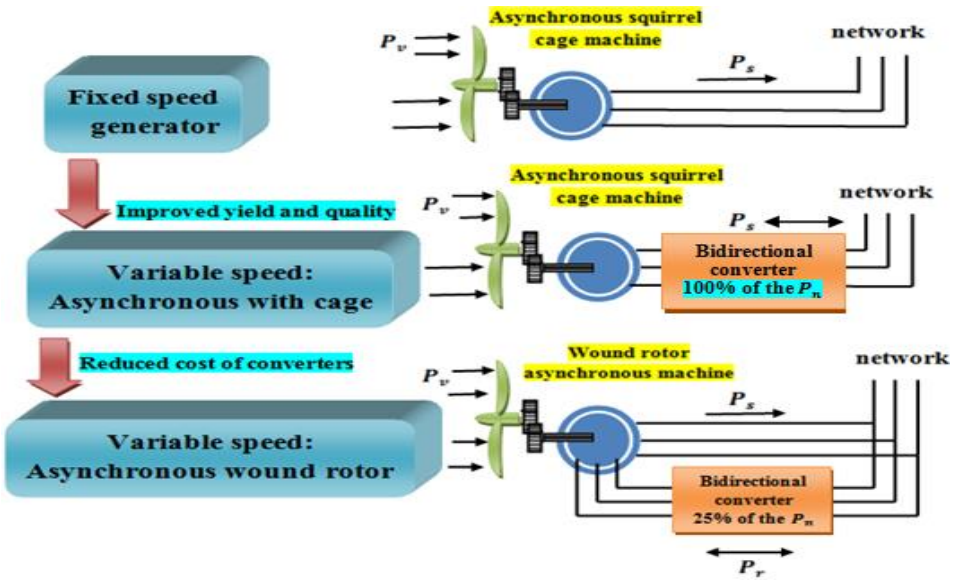

Figure I.9 Evolution of the electrical configuration

I.7.1 Fixed Speed Wind Turbines:

The structure of WTs systems that use fixed-speed generation, known as WTGS, has been extensively documented in [Hei 14], [Ame 03]. Fixed-speed WTGS use SCIGs that are directly connected to the power grid. These types of turbines typically operate at a speed very close to the synchronous speed of the generator, as the stiff torque speed characteristic of these machines requires a "fixed speed." However, this can result in slightly lower aerodynamic efficiency during low or high wind speeds. To magnetize the machine, induction generators need to consume reactive power, so power factor correction capacitors are installed at each WT to maintain a power factor close to unity. To limit flicker on the grid during startup, these systems use a soft-starter to reduce inrush current. Due to their cost-effectiveness and reliability, these solutions are attractive. A typical configuration of WT that uses fixed speed technology is shown in Figure I.10 [Sum 09].

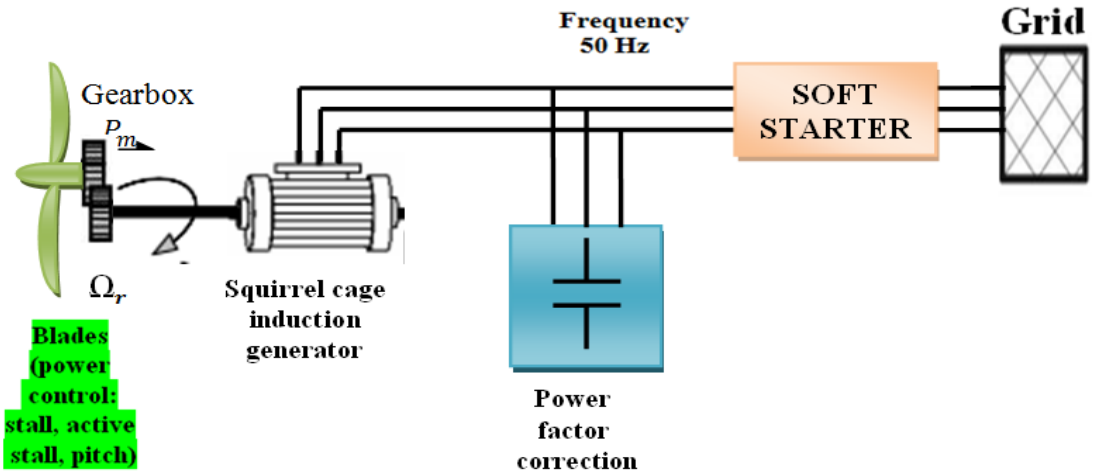

Figure I.10 Schematic setup of a fixed speed WTGS with SCIG

I.7.2 Variable Speed Wind Turbines:

WTs based on asynchronous machines can handle variable wind speeds, but the advantages, and configurations of each type differ from one another. Among the most common types are SCIG and DFIG.

I.7.2.1 Variable Speed WT based on Squirrel Cage Induction Generator:

The stator winding is connected to the power grid via a back-to-back converter, consisting of a Stator Side Converter, a DC Link, and a Grid Side Converter. The stator side converter's control system manages the electromagnetic torque and supplies the reactive power needed to keep the machine magnetized. The supply side converter

regulates the real and reactive power supplied from the system to the utility and regulates the DC link. The variable speed WT equipped with SCIG is illustrated in Figure I.11.

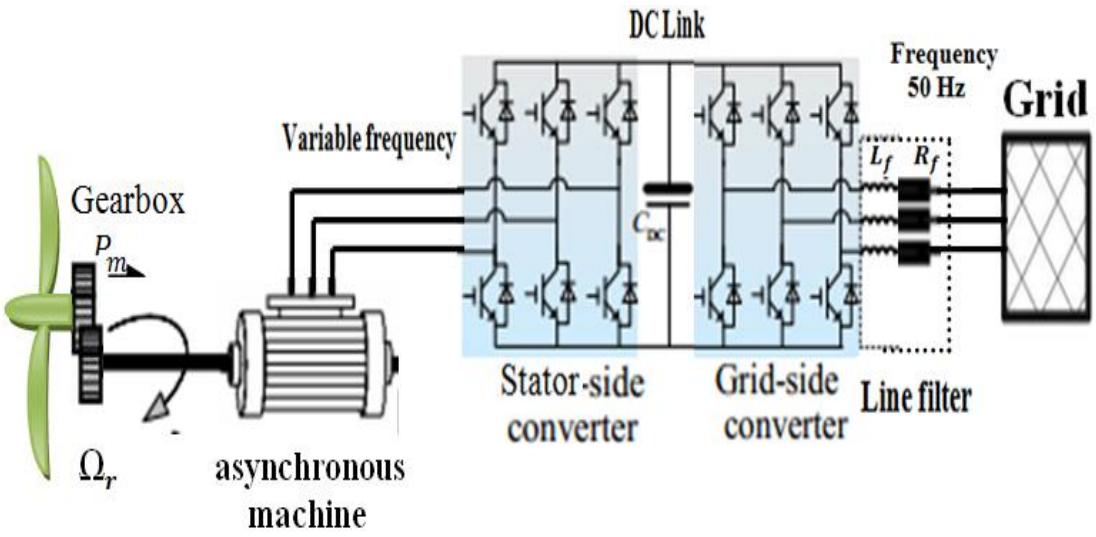

Figure I.11 Variable Speed Squirrel Cage Induction Generator

There are some advantages of SCIG, which can be summarized as follows [Mar 03]:

- The squirrel cage induction machine (SCIM) is widely used due to its ruggedness, brushless design, reliability, and cost-effectiveness.
- A rectifier is capable of producing programmable excitation for the generator.
- Fast transient response can be achieved.
- When spare capacity is available, the inverter can be utilized as a VAR/harmonic compensator.

Also, SCIG is not without some drawbacks, which are listed as follows [Mar 03]:

- Field-oriented control (FOC) is a complex system control technique that relies on accurate knowledge of the generator parameters, which can vary with temperature and frequency, for optimal performance.
- The stator side converter must be oversized by 30-50% of the rated power in order to meet the machine's magnetizing requirements.

I.7.2.2 Variable Speed WT based on DFIM:

For WTs that use DFIM, the stator is directly connected to the grid, while the rotor winding is connected to the grid through a back-to-back converter (RSC-DC link-GSC), as illustrated in Figure I.12.

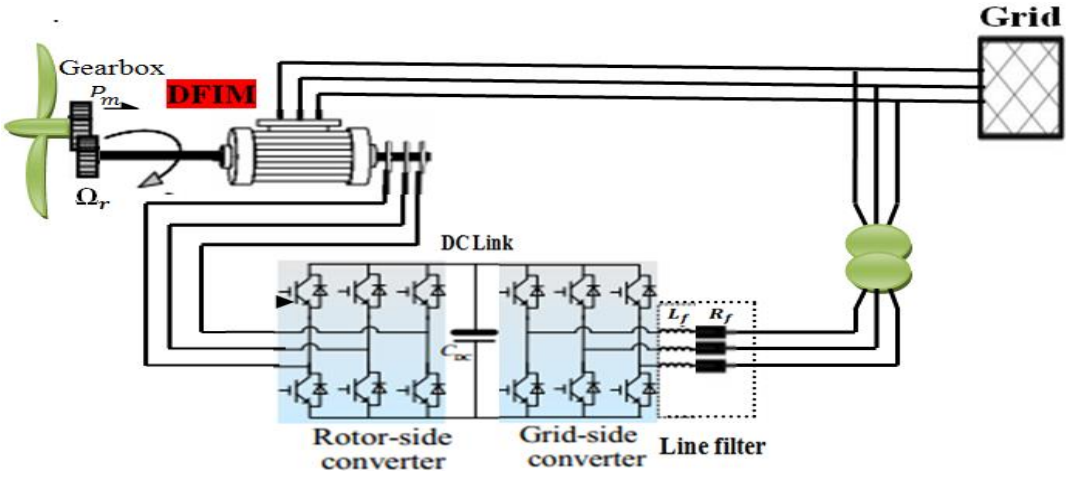

Figure I.12 Variable Speed WT based on DFIM

I.8 Description of the operation of the DFIM:

I.8.1 Structure of the DFIM

The DFIM, which has been known since 1899 [Bek 09], is essentially a standard wound-rotor induction machine equipped with slip rings. This machine comprises two three-phase windings of the stator and rotor that require independent power supply, and both windings can be supplied with bidirectional energy. The external structure of the doubly fed three-phase induction machine includes the stator and its three-phase windings, which are similar to those of a squirrel cage asynchronous machine and a synchronous machine. These windings are wound around magnetic plates that are stacked on top of each other, and they pass through slits in the plates, as shown in Figure I.13.

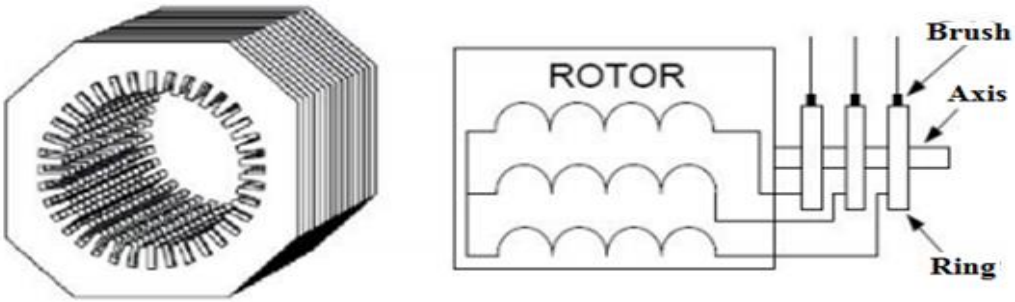

Figure I.13 Structure of the stator and rotor contacts of the DFIM

On the other hand, the rotor comprises stacked magnetic plates of circular shape with slits through which three-phase windings pass, and these are connected to sliding rings that are contacted by brushes installed in the stator to transmit voltage to the rotor. The stator circuit is connected directly to the grid, while the rotor circuit is controlled by a back-to-back converter via slip rings, as illustrated in Figure I.14 [Abo 18].

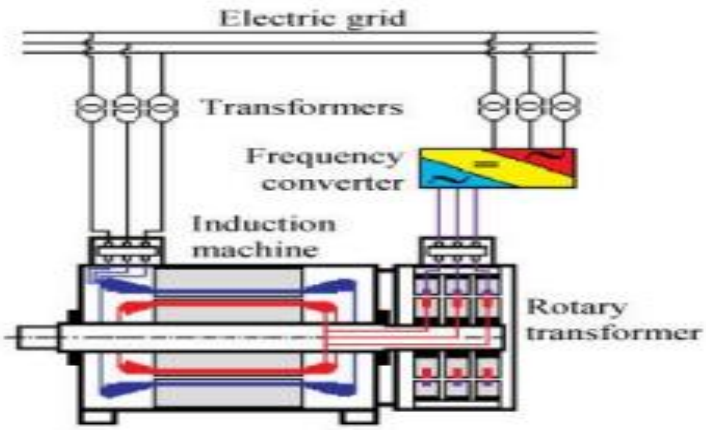

Figure I.14 DFIM connection to the grid

I.8.2 DFIM operating modes:

The DFIM can operate under different conditions depending on the power and speed. As a result, it can function both as a motor and a generator. When the DFIM operates as a motor at sub-synchronous speed, as shown in Figure I.15-a, the power P_r is provided by the rotor. If the speed increases so that the motor operates at super-synchronous speed, as illustrated in Figure I.15-b, the power P_r is absorbed by the rotor.

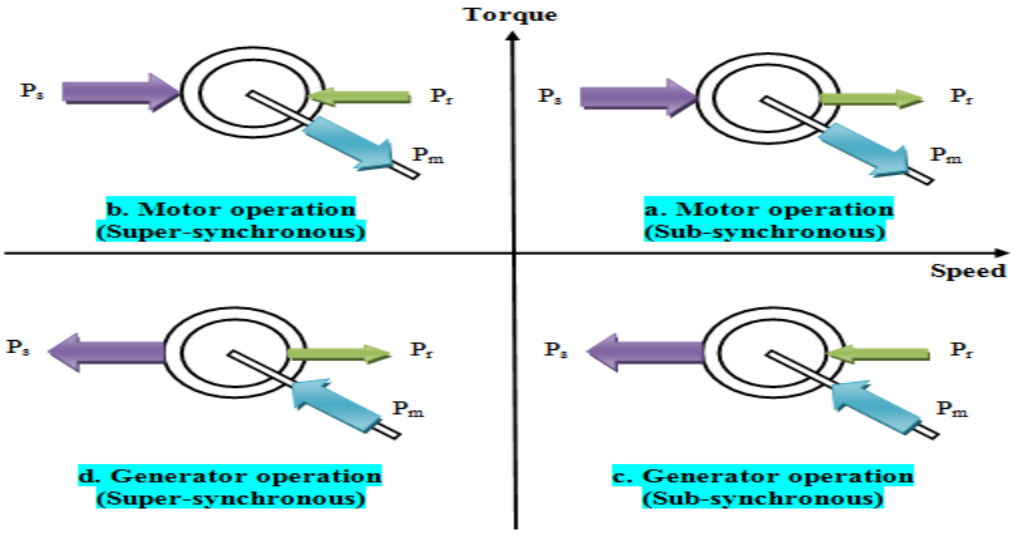

Figure I.15 Operational modes characteristic of the DFIM

While the DFIM operates as a generator at sub-synchronous speed, as depicted in Figure I.15-c, the power P_r is absorbed by the rotor. If the speed increases so that the generator operates at super-synchronous speed, as shown in Figure I.15-d, the power P_r changes direction, and the rotor can provide a possible recovery power [Abo 18].

I.8.3 Configurations of DFIM association with power converter:

DFIM has many configuration possibilities, and its power converter configuration capabilities vary according to the intended use of this machine. DFIM has received significant attention, especially in the field of wind power generation, owing to several advantages, including its low cost resulting from the small size of the back-to-back converter required to feed the rotor, whose capacity is one-third of the nominal power of the generator. The double power supply of the DFIM with the power converters installed provides many configuration situations classified into two main branches: motor operation with a single back-to-back converter and motor operation with two back-to-back converters.

I.8.3.1 Motor operation with a single back-to-back converter:

In this case, the machine's stator is directly connected to the network without transducers with a constant frequency and voltage amplitude. As for the rotor, it is connected to the back-to-back converter. This configuration reduces the power absorbed by this converter to one-third of the nominal power of the machine. Figure I.16 shows the use of a doubly fed induction motor with a single back-to-back converter.

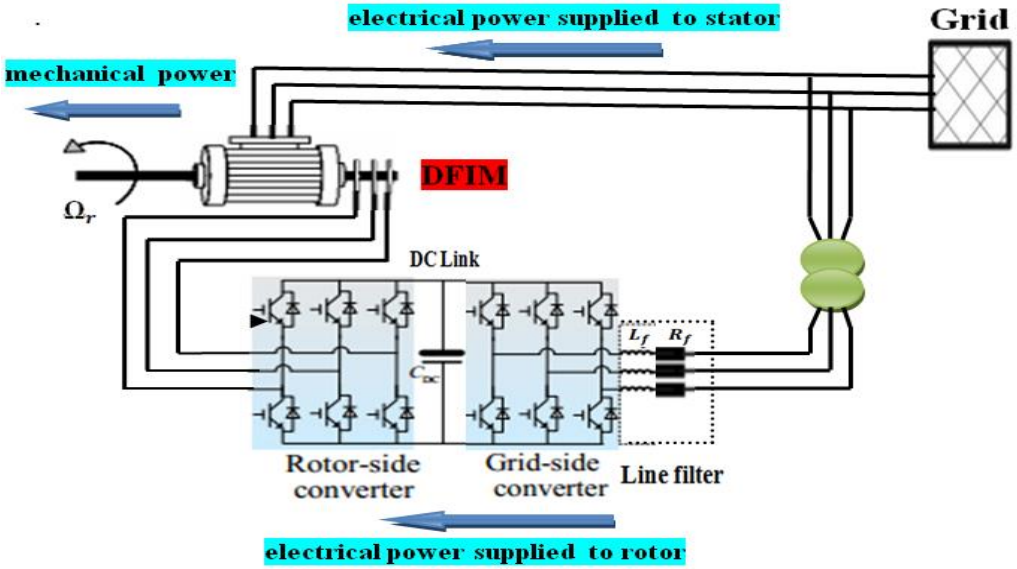

Figure I.16 DFIM as a motor supplied by a single back-to-back converter

I.8.3.2 Motor operation with a two back-to-back converters

Several authors have reported the possibility of operating a DFIM with power converters connected to both the stator and rotor. These configurations can be classified into three main categories:

- Common front end.
- Two independent converters with the same characteristics.
- Two independent converters with the same characteristics are used to feed a machine with a stator-rotor turn ratio that is not equal to 1. In this configuration, the stator of the machine is connected to the back-to-back converter (SSC-DC Link GSC), while the rotor is connected to the back-to-back converter (RSC-DC Link-GSC), as shown in Figure I.17.

It is possible to use different configurations depending on how the converters are connected, but the main objective is to have control over the power flow and the imposed electrical quantities, such as voltage, current, and frequency [Har 19].

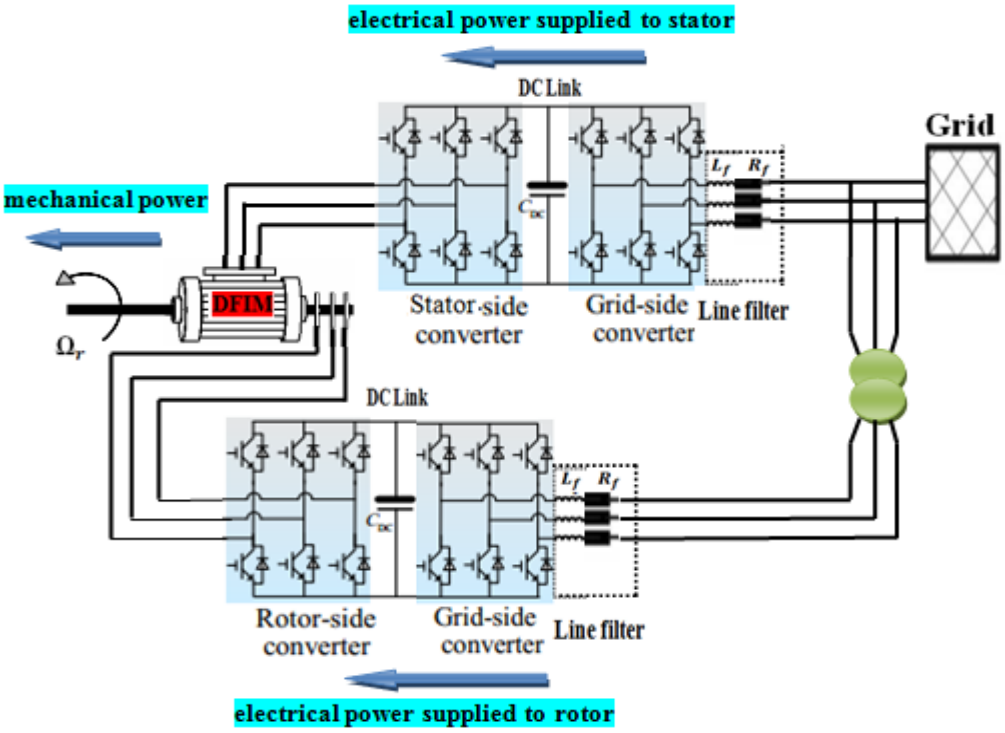

Figure I.17 DFIM as a motor supplied by two back-to-back converter

I.9 Advantages and Disadvantages of the DFIM

I.9.1 Advantages of the DFIM

There are several advantages of the DFIM are listed as:

- The DFIM can be fed and controlled by various possible combinations of stator or rotor [Bek 12].
- The use of a DFIM offers the opportunity to modulate power flow into and out of the rotor winding [Bek 12].
- The possibility of controlling and measuring the stator and rotor currents in a DFIM, unlike in an asynchronous squirrel cage machine, increases the accuracy and flexibility of controlling the electromagnetic torque and the machine's flow.

WTs based on DFIMs have several advantages, are listed as [Har 19], [Gov 14]:

- Firstly, as the rotor circuit is controlled by a power electronics converter, the induction generator can both import and export reactive power. This has significant implications for power system stability and enables the machine to support the grid during severe voltage disturbances (low-voltage ride-through; LVRT) [Har 19].
- A wide range of variable speed operation is possible.
- The stator is never fully loaded, and stress on the windings is also reduced, resulting in less heat generation. This enhances the reliability and ruggedness of the generator.
- WT based on DFIG ensures complete independence between active and reactive power control. It also provides high power output for low wind sites by capturing the maximum available power from the wind.
- This is a robust and well-proven technology.
- The size of the power converters used to control the rotor of DFIG is smaller, which makes it less expensive compared to fully-fed wind turbines that require converters with a capacity of approximately 30% of the nominal power rating.
- WTs based on DFIG have the ability to control reactive power without the need for capacitors.

I.9.2 Disadvantages of the DFIM:

The disadvantages of the DFIM are relatively few compared to other machines (PMSG, SCIG), which are as follows:

- The presence of brushes and slip rings in the DFIM requires more maintenance and monitoring.
- WTs based on DFIM suffer from gearbox issues, which makes them more costly in terms of maintenance and construction.
- The DFIM is very sensitive to grid disturbances such as voltage dips.

I.10 Conclusion

In this chapter, we presented a comprehensive study on wind energy, as this energy is clean and very available in nature. This energy was shed on WT based on DFIG. This machine is more common and used to generate wind energy due to its flexibility and adaptation to the changing wind speed when combined with transducers to control the generator rotor feeding, we also presented in this chapter the fields of using the double fed induction machine, when connected to power transformers. The first configuration of the machine is used as a wind power generator when its rotor is connected to the power transformer to control active and reactive power. The stator of machine is directly connected to the grid, which is the goal of our research. The second configuration applied to the machine is used. As a motor, by connecting the rotor to the rotor side converter, while the stator is connected to the grid side converter. The use of the first configuration has several advantages that are very attractive, including that the inverter connected to the rotor has a size of 25% to 30% of the rated power of the generator, which makes it more economical, and 100% of the rated power is obtained in the stator. The second configuration also features precise and flexible control of electromagnetic torque, flux, and motor speed operation in a wide range due to frequency control of the stator and rotor, with constant power. The next chapter focuses on the modeling and control of WT conversion system based on DFIM.

Chapter II

Wind Turbine Conversion System Modeling and Control based on DFIM

II.1 Introduction:

In this chapter, the modeling and control of WT and DFIM are studied based on a wind turbine conversion system. Initially, a WT model is created, including a multiplier and a mechanical shaft, without a control strategy. Subsequently, the MPPT strategy is implemented to achieve the maximum power output at all power points. Additionally, the model of DFIM, which incorporates electrical and mechanical terms is presented. The stator flux orientation strategy is used to simplify the induction machine model presented in this thesis and facilitate calculations. This strategy also enables easy control of active and reactive power while keeping them separate. To validate the model, a classical PI controller was employed for direct and indirect power control using MATLAB/Simulink. The model was tested under constant wind speed conditions with gradually changing active and reactive power, and randomly variable wind speed with active power extracted from the WT subject to MPPT strategy and reactive power set to zero.

II.2 General model of a wind turbine conversion chain based on DFIM

In this chapter section, we model the wind energy conversion system using DFIM. The stator of the DFIM is directly connected to the grid, while the rotor is linked to the grid through a back-to-back electronic converter (RSC-DC Link-GSC) controlled by PWM.

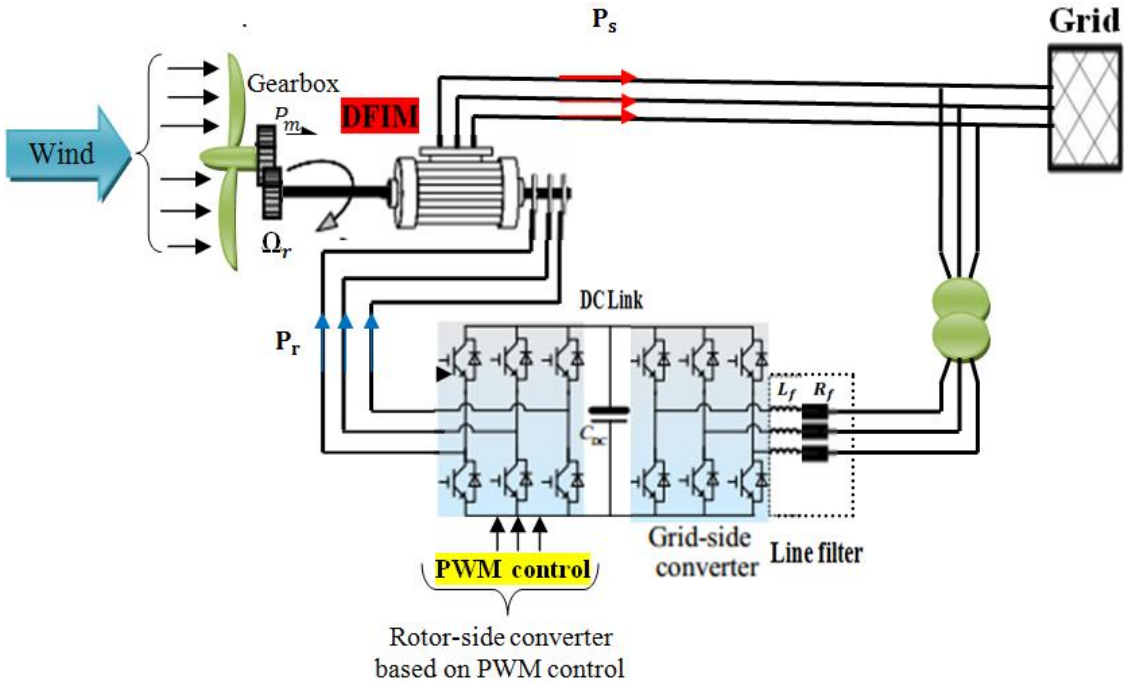

Figure II.1 Global wind power conversion chain based on DFIM

II.2.1 Model of Wind Turbine:

Wind Turbine power production is influenced by the interaction between the wind and the area swept by the wind currents represented by the blades carried on the rotor of the WT. The mean power output is determined by the average wind speed, and thus, only steady-state aerodynamics have been considered important for this project, with turbulence being ignored. The initial aerodynamic analyses of WTs were conducted by Betz and Glauert in the late 1920s and early 1930s. The power available in the wind is calculated by the relation below [Sing 11-1]:

The wind power that swept through the WT input is given by [Bek 13]:

$$P_v = \frac{1}{2}\rho S_w v^3 \tag{II.1}$$

where: ρ is the air density (ρ =1.22kg.m^{-2}); S_w is the circular surface drawn by the blades of WT swept by the wind (m^2); v is wind speed.

The mechanical power required to rotate the WT is generated by the wind power applied to the WT blades, which can be expressed as follows:

$$P_m = C_p P_v = \frac{1}{2} C_p . \rho . S_w . v^3 \tag{II.2}$$

where: C_p represents the power factor, that expresses the efficiency of the energy conversion of WT. The blade length of the WT determines the radius of the circle (R), which in turn determines the circular surface area covered by the rotating blades according to the following relation:

$$S_w = \pi R^2 \tag{II.3}$$

The power coefficient (C_p) varies as a function of λ and β according to:

$$C_p(\beta, \lambda) = (0.5 - 0.0167.(\beta - 2)).\sin\left(\frac{\pi.(\lambda + 0.1)}{(18.5 - 0.3.(\beta - 2))}\right) - 0.00184.(\lambda - 3).(\beta - 2) \tag{II.4}$$

where: λ is the tip speed ratio; β is the blade pitch angle. The equation of the turbine blade tip speed (λ) as a function of the angular speed (Ω_t) and wind speed is shown as:

$$\lambda = \frac{R \Omega_t}{v} \tag{II.5}$$

II.2.1.1 Model of the Multiplier:

The WT is typically connected to the generator shaft via a gearbox, which is designed to achieve a desired range of speeds for the generator shaft by selecting an appropriate gear ratio. Neglecting any transmission losses, the torque and shaft speed of the WT on the generator side of the gearbox can be expressed as [Bek 13]:

$$T_g = \frac{T_{tur}}{G} \tag{II.6}$$

where: G is the gearbox; T_g is the generator shaft torque; T_{tur} is the turbine torque. The gearbox is positioned between the turbine and generator in order to adapt the turbine's speed with that of the generator.

$$\Omega_{tur} = \frac{\Omega_{mec}}{G} \tag{II.7}$$

where: Ω_{mec} is the generator shaft speed, Ω_{tur} is the turbine speed.

II.2.1.2 Model of the Mechanical Shaft:

The mechanical expressions for the shaft of a WT with DFIG are given by [Bed 14]:

$$J_T = J_{gen} + \frac{J_{tur}}{G^2} \tag{II.8}$$

$$f_T = f_{gen} + \frac{f_{tur}}{G^2} \tag{II.9}$$

$$T_{gen} - T_{em} = J_T \frac{d\Omega_{mec}}{dt} + f_T \Omega_{mec} \tag{II.10}$$

where: J_T, f_T are the total inertia and viscous friction coefficient of the WT; J_{gen}, f_{gen} are the inertia and viscous friction coefficient of the generator; J_{tur}, f_{tur} are the inertia and viscous friction coefficient of the turbine.

According to a mechanical system being defined by the sum of all its mechanical characteristics, a mechanical model has been presented as shown in Figure II.2 [Bed 14].

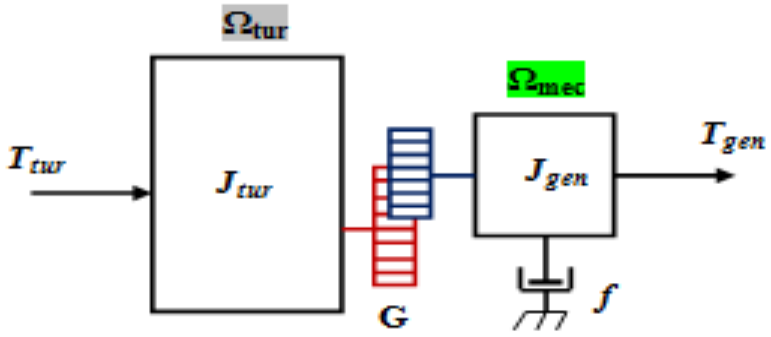

Figure II.2 Mechanical model simplified of wind turbine

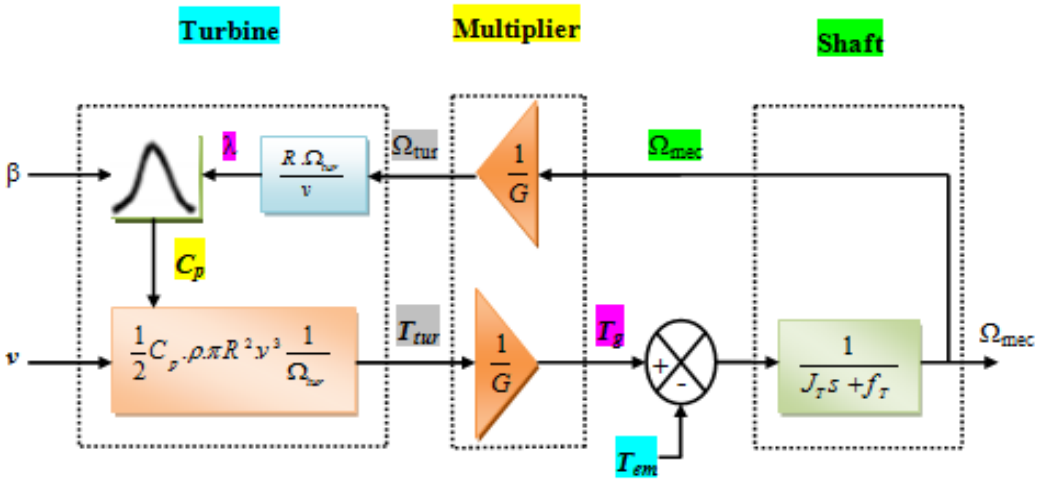

Figure II.3 Block scheme of the wind turbine model

II.2.2 Wind Turbine Control Strategy

II.2.2.1 Power Characteristic - Speed of Large Power Wind Turbines

The power-speed curve for WTs can be divided into four different regions, as illustrated in Figure II.4.

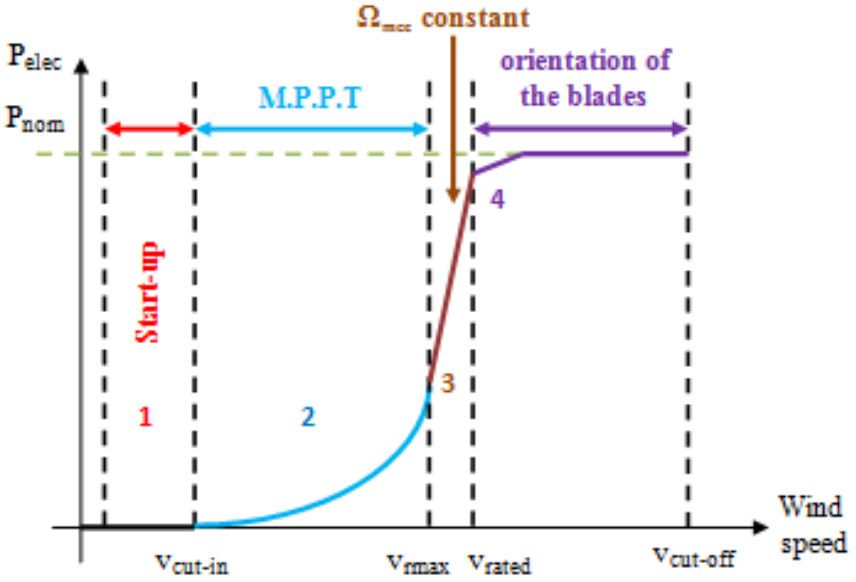

Figure II.4 Typical Power-Speed characteristic of a wind turbine of great power

The power-speed curve of WTs can be divided into four regions, each of which is explained as [Luo 14], [Soh 16]:

- The first region is called the start-up region. In this region, the power output is zero when the wind speed is less than a minimum threshold known as the cut-in speed.
- The second region, which is located between the cut-in speed ($v_{cut\text{-}in}$) and the maximum speed (v_{rmax}), is characterized by a rapid increase in the energy produced. This is achieved by utilizing the maximum power point tracking (MPPT) technique while fixing the blade angle at ($\beta=2^{\circ}$). This technique is employed until the maximum speed (v_{rmax}) is reached.
- The third region is located between the maximum speed (v_{rmax}) and the rated speed (v_{rated}). WTs in this region operate at a constant speed (Ω_{mec} constant), causing the rated power of the generator to increase until it reaches 90% of the nominal power.
- The fourth region is located between the rated speed (v_{rated}) and the cut-off speed ($v_{cut\text{-}off}$). In this region, a constant rated output is produced at the nominal power level, while the generated power is reduced using a blade orientation system.

II.2.3 Model of DFIM

Many installed WTs today are equipped with the DFIMs. However, most of these machines are connected directly to the network to avoid the use of converters. The major advantage of this configuration is that the power rating of the inverters is only around 25-30% of the nominal generator power [Amr 16]. The model of the DFIM is based on that of the asynchronous squirrel cage machine, with the main difference lying in the rotor design.

The rotor of the DFIM is designed with three windings for three phases, which are fed with alternating voltage. The most significant characteristic of this type of wound-rotor machine is that it must be fed from both the stator and rotor sides [Tap 03]. The three-phase windings for both the stator and rotor of the DFIM are illustrated in Figure II.5.

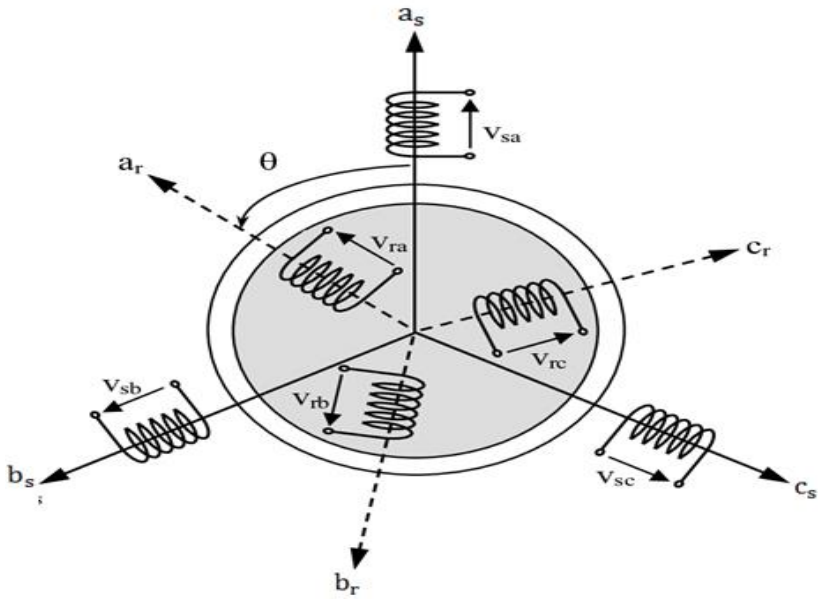

Figure II.5 Representation of the three-phase winding of the DFIM

where:

a_s, b_s, c_s: represent the three-phase axes of the stator.

a_r, b_r, c_r: represent the three-phase axes of the rotor.

In this section, we will first provide a brief overview of the basic three-phase ABC model of the DFIM. Then, to simplify the explanation, we will discuss the two-axes stationary reference frame, also known as the d-q model. Finally, we will explore the synchronously rotating reference frame, which is conventionally used for controlling the DFIM wind turbine system [Hash 18].

II.2.3.1 ABC Reference Frame

The DFIM being discussed has two poles (n_p=1) and three-phase windings that are symmetrically positioned on both the stator and rotor. The resistances, magnetizing inductances, and leakage inductances are uniform across all three phases. The windings are spaced 120 electrical degrees apart from each other on both the stator and rotor. Furthermore, each rotor phase leads its corresponding stator phase by a phase angle denoted as θr. The rotor revolves at an angular speed of w_r in the counter-clockwise direction. For the sake of simplifying the development of the ABC model, a set of assumptions has been taken into account, which are elaborated below [Hash 18]:

- **Sinusoidal Electromagnetic Force Distribution:** The electromagnetic force around the stator winding is assumed to follow a sinusoidal distribution. This is done in order to mitigate the presence of harmonic components.
- **Constant Air Gap:** It is assumed that the air gap between the stator and rotor remains constant. This assumption helps in maintaining a consistent level of mutual inductance among the various phases of both the stator and rotor windings. The mutual inductance between the stator and rotor is influenced by the angular position θ_r.
- **Neglecting Cross-Saturation and Skin Effects:** The cross-saturation effect and skin effect are disregarded in this simplified model. The cross-saturation effect involves alterations in resistances and leakage inductances due to an increase in frequency. The skin effect signifies the interaction between two perpendicular axes.
- **Neglecting Core Iron Losses:** Any losses in the core iron are not taken into account in this simplified model.

II.2.3.2 DFIM Equations

The electrical and mechanical equations are formulated using the triple reference ABC, which is shown in Figure II.5.

- **Electrical Equations**

The three-phase voltage equations of the stator and the rotor are given as:

$$\begin{bmatrix} V_{as} \\ V_{bs} \\ V_{cs} \end{bmatrix} = \begin{bmatrix} R_s & 0 & 0 \\ 0 & R_s & 0 \\ 0 & 0 & R_s \end{bmatrix} . \begin{bmatrix} i_{as} \\ i_{bs} \\ i_{cs} \end{bmatrix} + \frac{d}{dt} \begin{bmatrix} \phi_{as} \\ \phi_{bs} \\ \phi_{cs} \end{bmatrix} \quad \text{(II.11)}$$

$$\begin{bmatrix} V_{ar} \\ V_{br} \\ V_{cr} \end{bmatrix} = \begin{bmatrix} R_r & 0 & 0 \\ 0 & R_r & 0 \\ 0 & 0 & R_r \end{bmatrix} . \begin{bmatrix} i_{ar} \\ i_{br} \\ i_{cr} \end{bmatrix} + \frac{d}{dt} \begin{bmatrix} \phi_{ar} \\ \phi_{br} \\ \phi_{cr} \end{bmatrix} \quad \text{(II.12)}$$

where:

$[V_{as}\ V_{bs}\ V_{cs}]^T$, $[V_{ar}\ V_{br}\ V_{cr}]^T$: stator and rotor voltage vectors.

$[i_{as}\ i_{bs}\ i_{cs}]^T$, $[i_{ar}\ i_{br}\ i_{cr}]^T$: stator and rotor current vectors.

$[\phi_{as}\ \phi_{bs}\ \phi_{cs}]^T$, $[\phi_{ar}\ \phi_{br}\ \phi_{cr}]^T$: stator and rotor flux vectors.

R_s, R_r: represent the resistance of the stator and the rotor, respectively.

- **Magnetic Equations**

The expressions for the three-phase flux of the stator and the rotor as functions of current are provided below:

$$\begin{bmatrix} \phi_{as} \\ \phi_{bs} \\ \phi_{cs} \end{bmatrix} = \begin{bmatrix} L_s & M_s & M_s \\ M_s & L_s & M_s \\ M_s & M_s & L_s \end{bmatrix} . \begin{bmatrix} i_{as} \\ i_{bs} \\ i_{cs} \end{bmatrix} + \left[M_{sr}\right] . \begin{bmatrix} i_{ar} \\ i_{br} \\ i_{cr} \end{bmatrix} \quad \text{(II.13)}$$

$$\begin{bmatrix} \phi_{ar} \\ \phi_{br} \\ \phi_{cr} \end{bmatrix} = \begin{bmatrix} L_r & M_r & M_r \\ M_r & L_r & M_r \\ M_r & M_r & L_r \end{bmatrix} . \begin{bmatrix} i_{ar} \\ i_{br} \\ i_{cr} \end{bmatrix} + \left[M_{sr}\right] . \begin{bmatrix} i_{as} \\ i_{bs} \\ i_{cs} \end{bmatrix} \quad \text{(II.14)}$$

where:

L_s, L_r: stator and rotor inductances, respectively.

M_s: mutual magnetic induction between stator phases.

M_r: mutual magnetic induction between rotor phases.

The mutual magnetic induction matrix $[M_{sr}]$ is a function of the rotor position relative to the stator and rotor phases, which is described by the angle θ between their axes. Therefore, the matrix also varies with time and is related to the angular velocity (w) and time t as follows: $\theta = w.t$.

$$[M_{sr}] = M_0.\begin{bmatrix} \cos\theta & \cos(\theta-\frac{4\pi}{3}) & \cos(\theta-\frac{2\pi}{3}) \\ \cos(\theta-\frac{2\pi}{3}) & \cos\theta & \cos(\theta-\frac{4\pi}{3}) \\ \cos(\theta-\frac{4\pi}{3}) & \cos(\theta-\frac{2\pi}{3}) & \cos\theta \end{bmatrix} \quad \text{(II.15)}$$

where:

M_0: maximum mutual magnetic induction between the stator phase and the corresponding phase of the rotor.

II.2.3.3 Application of the Park Transformation of DFIM

Park's transformation is a widely used technique in the analysis of electric machines [Sol 03]. This transformation converts the three AC quantities (V_a V_b V_c) into two DC quantities (V_d V_q) in order to simplify calculations, control, and analysis [Shu 21]. This results in simplified model equations that yield the same outcomes.

The transformation matrix for Park's transformation is given by:

$$[P] = \sqrt{\frac{2}{3}}.\begin{bmatrix} \cos(\theta) & \cos(\theta-\frac{2\pi}{3}) & \cos(\theta-\frac{4\pi}{3}) \\ -\sin(\theta) & -\sin(\theta-\frac{2\pi}{3}) & -\sin(\theta-\frac{4\pi}{3}) \\ \frac{1}{\sqrt{2}} & \frac{1}{\sqrt{2}} & \frac{1}{\sqrt{2}} \end{bmatrix} \quad \text{(II.16)}$$

The voltage equation for this transformation is given by:

$$[V_{dq0}] = [P].[V_{abc}] \quad \text{(II.17)}$$

The transformation matrix for inverse Park's transformation is given by:

$$[P]^{-1} = \sqrt{\frac{2}{3}}.\begin{bmatrix} \cos(\theta) & -\sin(\theta) & \frac{1}{\sqrt{2}} \\ \cos(\theta-\frac{2\pi}{3}) & -\sin(\theta-\frac{2\pi}{3}) & \frac{1}{\sqrt{2}} \\ \cos(\theta-\frac{4\pi}{3}) & -\sin(\theta-\frac{4\pi}{3}) & \frac{1}{\sqrt{2}} \end{bmatrix} \quad \text{(II.18)}$$

The voltage equation by inverse transformation is given by:

$$[V_{abc}] = [P]^{-1}[V_{dq0}] \tag{II.19}$$

The current equations for this transformation is given by:

$$[I_{dq0}] = [P].[I_{abc}] \tag{II.20}$$

The current equations using inverse transformation is given by:

$$[I_{abc}] = [P]^{-1}[I_{dq0}] \tag{II.21}$$

The flux equation for this transformation is given by:

$$[\phi_{dq0}] = [P].[\phi_{abc}] \tag{II.22}$$

The flux equation using inverse transformation is given by:

$$[\phi_{abc}] = [P]^{-1}[\phi_{dq0}] \tag{II.23}$$

where:

$$[V_{dq0}] = [V_d\ V_q\ V_0]^T$$
$$[I_{dq0}] = [I_d\ I_q\ I_0]^T$$
$$[\phi_{dq0}] = [\phi_d\ \phi_q\ \phi_0]^T$$

The DFIM model that uses the d q-axis is shown in Figure II.6.

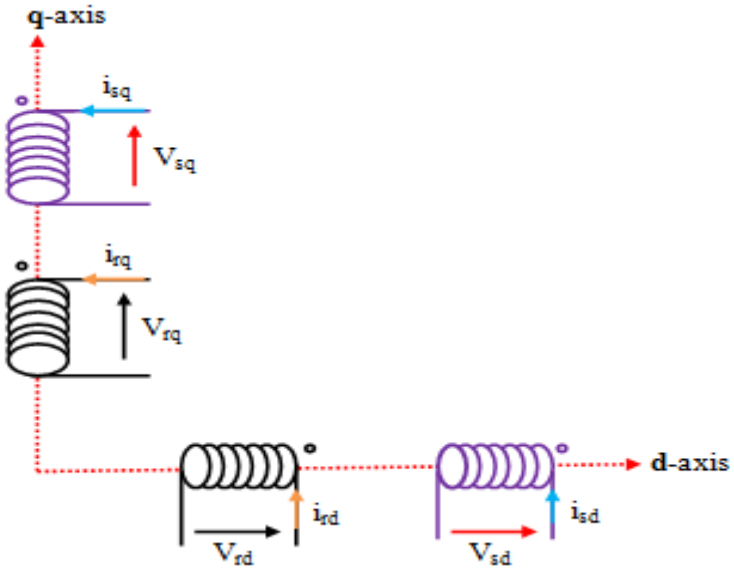

Figure II.6 DFIM model using park transform (d q frame)

After transforming from (a, b, c) reference to (d, q) reference. The stator and rotor voltages are given as below [Ari 22]:

$$\begin{cases} V_{sdq} = R_s.i_{sdq} + \dfrac{d}{dt}\phi_{sdq} \mp \omega_s.\phi_{sqd} \\ V_{rdq} = R_r.i_{rdq} + \dfrac{d}{dt}\phi_{rdq} \mp (\omega_s - \omega).\phi_{rqd} \end{cases} \quad \text{(II.24)}$$

The stator and rotor flux along the d-q axis are given by:

$$\begin{cases} \phi_{sdq} = L_s.i_{sdq} + M.i_{rdq} \\ \phi_{rdq} = L_r.i_{rdq} + M.i_{sdq} \end{cases} \quad \text{(II.25)}$$

The stator active and reactive powers are given by:

$$\begin{cases} P_s = V_{sd}.i_{sd} + V_{sq}.i_{sq} \\ Q_s = V_{sq}.i_{sd} - V_{sd}.i_{sq} \end{cases} \quad \text{(II.26)}$$

The rotor active and reactive powers are given by:

$$\begin{cases} P_r = V_{rd}.i_{rd} + V_{rq}.i_{rq} \\ Q_r = V_{rq}.i_{rd} - V_{rd}.i_{rq} \end{cases} \quad \text{(II.27)}$$

The electromagnetic torque of DFIG is given by:

$$T_{em} = P\frac{M}{L_s}(\phi_{sd}i_{rq} - \phi_{sq}i_{rd}) \quad \text{(II.28)}$$

The angular velocity of the rotor currents can be expressed as a function of the stator angular velocity imposed by the grid, the number of pole pairs, and the rotor speed as:

$$w_r = w_s - p.\Omega \quad \text{(II.29)}$$

where:

w_s: represents the angular velocity of the stator currents, The unit is given in rad.s^{-1}.

w_r: represents the angular velocity of the rotor currents, The unit is given in rad.s^{-1}.

The angles θ_s and θ_r is obtained by the following integration relations:

$$\begin{cases} \theta_s = \int_0^t w_s dt \\ \theta_r = \int_0^t w_r dt \end{cases} \tag{II.30}$$

II.3 Wind Turbine Control Using MPPT

To achieve the highest possible utilization of wind energy for WTs, it is necessary to orient the turbine blades to track the maximum power points at varying wind speeds. The significant variation in rotor speed of the DFIG facilitates the attainment of the maximum attainable power (which is sought in zone 2) from the wind [Ari 22]. Figure II.7 depicts the coefficient of power (C_p) as a function of λ, with each curve defined by a change in value of β. From this figure, it is evident that an optimal value of λ (λ_{opt} = 9.2) and blade pitch angle (β = 2°) exist, corresponding to the maximum value of C_p ($C_{p\text{-}max}$ = 0.5). This results in maximum power absorption at a certain wind speed, and the peak power for each wind speed corresponds to $C_{p\text{-}max}$. To ensure the maximum power generation, the WT must have a control characteristic capable of tracking the maximum line [Bek 13].

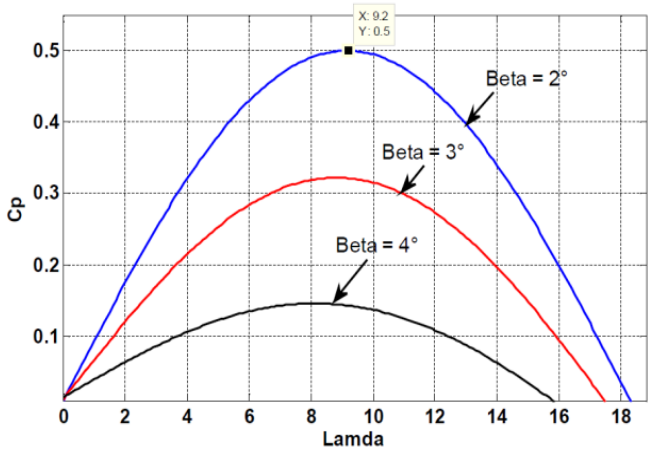

Figure II.7 Power coefficient C_p as a function of λ

There is great difficulty in measuring wind speed when applying MPPT control algorithm, but we can give an estimate of its value, by the following equation [Ben 20-1]:

$$V_{est} = \frac{\Omega_{tur} R_t}{\lambda_{opt}} \tag{II.31}$$

where: λ_{opt} is called the optimal tip speed ratio.

In order to achieve MPPT control algorithm, the reference aerodynamic power should be set as follows:

$$P_{aer}^{*} = \frac{\pi.\rho}{2} C_{p-\max}.R_t^2.V_{est}^3 \tag{II.32}$$

where: P^{*}_{aer} is called the reference aerodynamic power of the wind turbine; $C_{p\text{-}max}$ is the maximum value of the C_p. Based on the reference aerodynamic power equation, the reference electromagnetic torque equation is given as follows:

$$T_{em}^{*} = \frac{P_{ear}^{*}}{\Omega_{tur}} = \frac{\pi.\rho}{2} C_{p\text{-}\max}.\frac{R_t^5 \Omega_{tur}^{\ 2}}{\lambda_{opt}^{\ 3}} \tag{II.33}$$

where: Ω_{tur} is the angular speed of WT; T^{*}_{em} is the reference torque of WT.

The WT model with MPPT using reference electromagnetic torque is shown in Figure II.8.

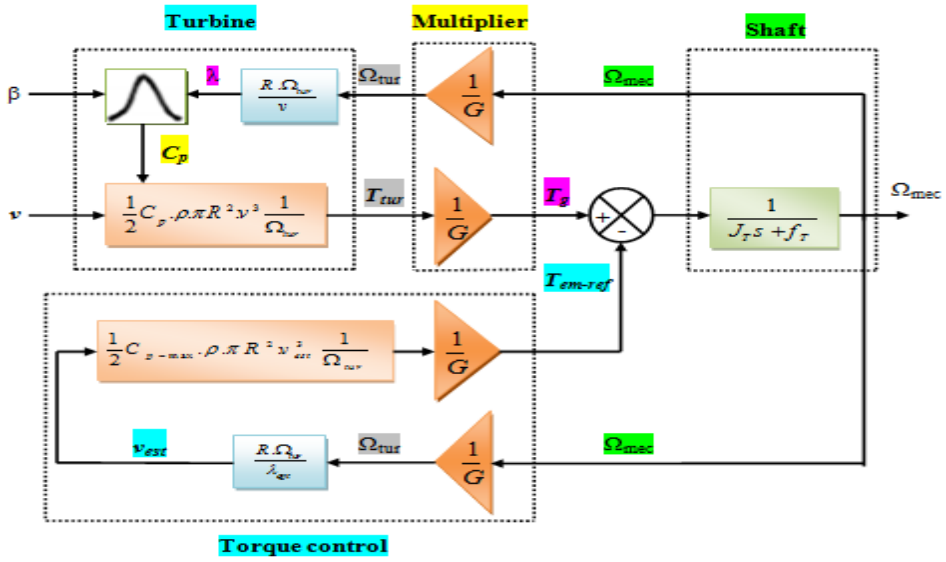

Figure II.8 Wind turbine model with MPPT strategy

II.4 DFIG for Independent Stator Active and Reactive Power Control

In order to achieve vector control of DFIG, it is recommended to choose a reference related to the rotating field. Once the DFIG is connected to an electrical grid, it becomes necessary to find a strategy that achieves independent control of stator active and reactive powers. This can be achieved by using stator flux orientation along the d-axis of the (d, q) reference frame. However, the quadratic component (q-axis) of the stator flux should be set to zero, as shown in Figure II.9 [Ben 20].

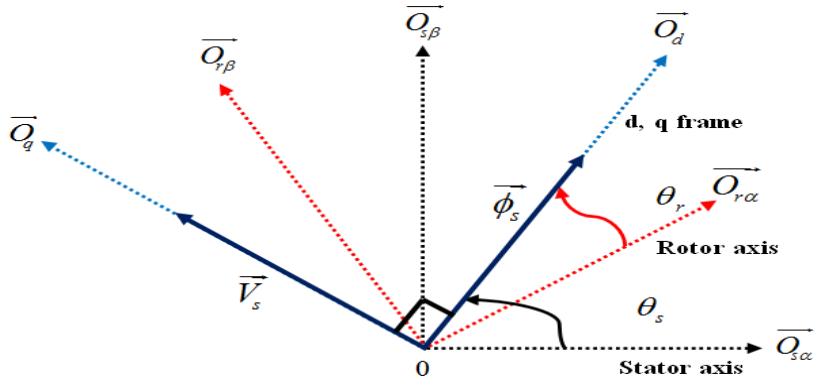

Figure II.9 Stator flux orientation diagram of (d q) reference frame

By applying stator flux orientation technology along the d-axis and neglecting the stator resistance value, which is typically very small, the expressions of stator flux and voltage can be written as:

$$\phi_{sd} = \phi_s = L_s i_{sd} + M i_{rd} \tag{II.34}$$

$$\phi_{sq} = 0 = L_s i_{sq} + M i_{rq} \tag{II.35}$$

$$v_{sd} = 0 \tag{II.36}$$

$$v_{sq} = v_s \approx w_s \phi_s \tag{II.37}$$

The stator active and reactive powers can be written in the simplified form as follows:

$$P_s = -V_s \frac{M}{L_s} i_{rq} \tag{II.38}$$

$$Q_s = \frac{V_s^2}{\omega_s L_s} - V_s \frac{M}{L_s} i_{rd} \tag{II.39}$$

From (II.38) and (II.39), we can observe that the stator active power (P_s) is directly proportional to the quadratic rotor current (i_{rq}). On the other hand, the stator reactive power (Q_s) is proportional to the direct rotor current (i_{rd}), with an additional term of (V_s^2/ L_s.w_s), which is related to the stator voltage (V_s).

By substituting (II.25) into (II.24), we can obtain the rotor voltages as:

$$\begin{cases} V_{rd} = R_r.i_{rd} + \sigma L_r \dfrac{di_{rd}}{dt} - gw_s \sigma L_r i_{rq} \\ V_{rq} = R_r.i_{rq} + \sigma L_r \dfrac{di_{rq}}{dt} + g\dfrac{M.V_s}{L_s} + gw_s \sigma L_r i_{rd} \end{cases} \quad \text{(II.40)}$$

where:

$$\sigma = 1 - \frac{M^2}{L_s.L_r}$$

By utilizing the previously mentioned equations, we can construct a block diagram of the DFIM using the relations that connect the rotor voltages of the (d, q) axes to the rotor currents of the (d, q) axes. Then, we can find the relationships that link the rotor currents to strategy the stator active and reactive powers. This diagram represents a simplified form of the doubly fed induction machine, which employs the stator flux orientation and neglects some terms. The block scheme of the simplified mathematical model of the DFIM is shown in Figure II.10.

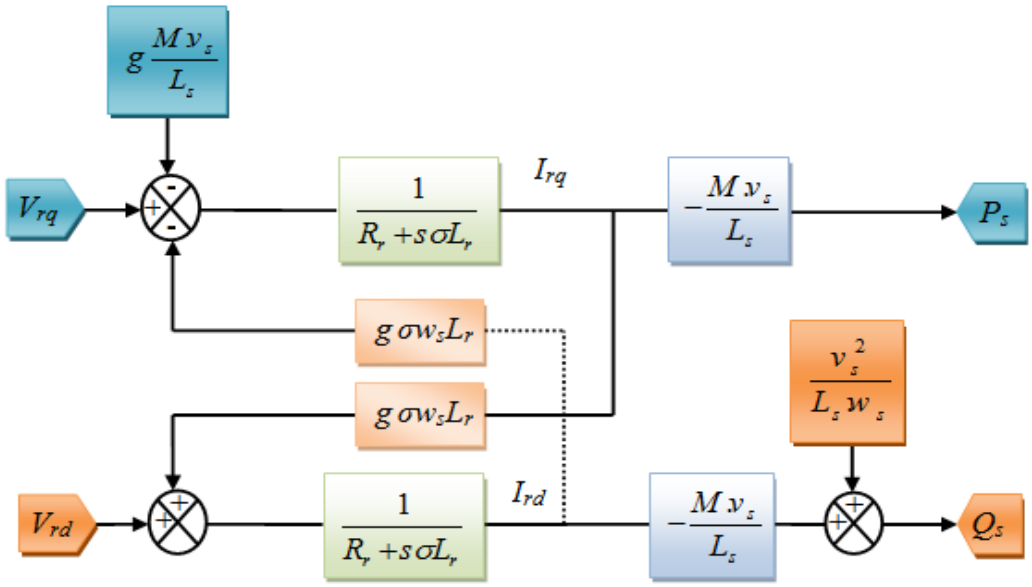

Figure II.10 The block scheme of simplified model of DFIM

II.4.1 DPC using PI controller of DFIG

This method involves regulating the stator active and reactive stator powers of DFIG independently by using a PI controller on each axis while neglecting the coupling terms between the two axes. This method is called direct power control (DPC) because the PI controller acts directly on the voltages. The model of DPC using PI controller is shown in Figure II.11 [Boude 18].

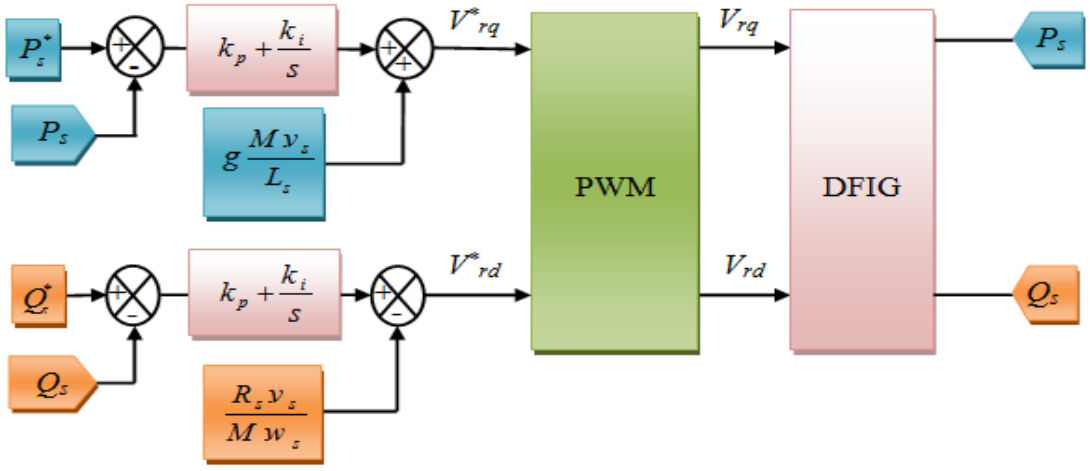

Figure II.11 DPC using PI controller of DFIG

Dimensioning of the PI Regulator

To track the reference values of stator active and reactive powers, it is necessary to calculate the dimensions of the power regulator using the rotor parameters of the DFIG and select the response time of the control system based on its speed. The closed loop of the stator active and reactive powers regulator is depicted in Figure II.12.

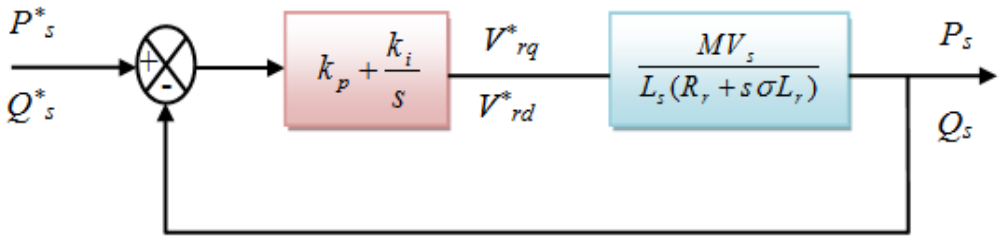

Figure II.12 The closed-loop scheme of PI corrector for P_s and Q_s regulation

It can be seen from Figure II.12 that the stator active power regulator corresponding to the q-axis is symmetrical with the stator reactive power regulator corresponding to the d-axis, so they are drawn in the same scheme.

The transfer function (TF) of the PI regulator is given by:

$$PI(s) = k_p + \frac{k_i}{s} \tag{II.41}$$

Through the TF of the PI regulator and the machine system function, we can write The open loop transfer function (OLTF) as:

$$OLTF(s) = (k_p + \frac{k_i}{s})(\frac{MV_s}{L_s(R_r + s\sigma L_r)}) \tag{II.42}$$

By extracting the common factors, we find:

$$OLTF(s) = \frac{k_i}{s}(\frac{k_p}{k_i}s + 1)(\frac{(MV_s / L_s R_r)}{(s\sigma T_r + 1)}) \tag{II.43}$$

where $T_r=R_r/L_r$

By applying the pole compensation method, between PI corrector and machine system, we find:

$$\frac{k_p}{k_i} = \sigma T_r \tag{II.44}$$

When the previous condition is applied, the OLTF becomes as:

$$OLTF(s) = \frac{k_i MV_s}{L_s R_r s} \tag{II.45}$$

Through OLTF, the closed loop transform function (CLTF) can be expressed as:

$$CLTF(s) = \frac{OLTF(s)}{1 + OLTF(s)} \tag{II.46}$$

Therefore, after application and shorthand, we find:

$$CLTF(s) = \frac{1}{1 + s\frac{L_s R_r}{k_i MV_s}} \tag{II.47}$$

To ensure that the expression for a first-order linear system is correct, it must be written in the following form:

$$G(s) = \frac{1}{1+\tau s} \tag{II.48}$$

By matching between (II.47) and (II.48), we find:

$$\tau = \frac{L_s R_r}{k_i M V_s} \tag{II.49}$$

From (II.44) and (II.49), K_p and K_i can be deduced as:

$$\begin{cases} K_i = \dfrac{L_s R_r}{\tau M V_s} \\ K_p = K_i \sigma T_r = \dfrac{\sigma L_s L_r}{\tau M V_s} \end{cases} \tag{II.50}$$

To achieve a very fast control system, a value of $\tau = 0.001$ sec was chosen. The system electrical time constant for this machine can be calculated as $\tau_e = \sigma T_r$.

II.4.2 IDPC using PI controller of DFIG

II.4.2.1 IDPC without Power Loops using PI controller of DFIG

In this case, the stator active and reactive power were controlled indirectly by regulating the rotor currents using a PI controller for each axis. This was done by taking into consideration the coupling terms [Boude 18], and extracting the rotor reference current of the d-axis from the stator active reference power, and extracting the rotor reference current of the q-axis from the stator reactive reference power, as shown in Figure II.13.

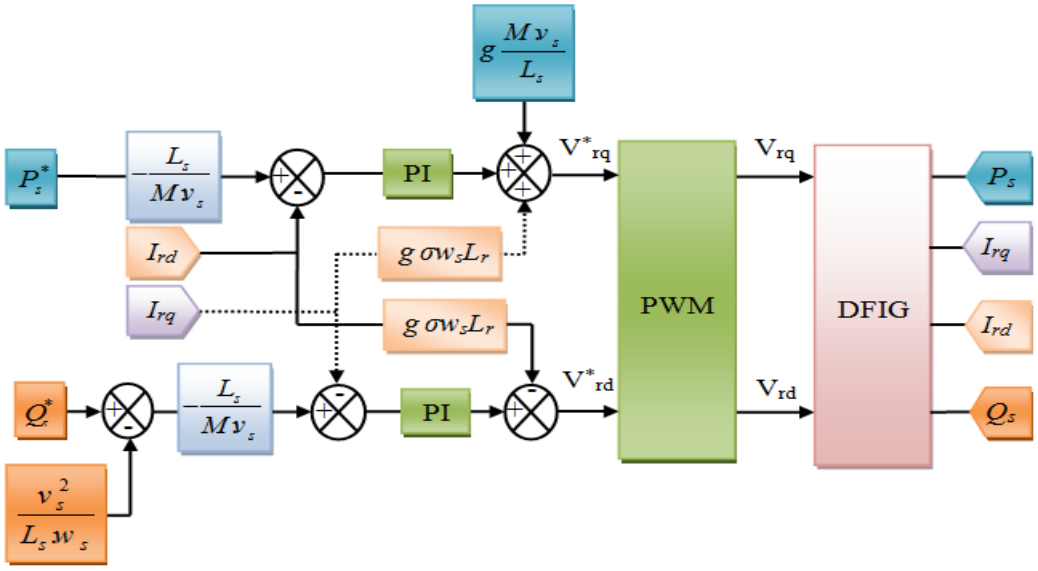

Figure II.13 IDPC without power loops using PI controller of DFIG

Dimensioning of the PI Regulator

From (II.40), the decoupling terms will be canceled as follows:

$$\begin{cases} -gw_s \sigma L_r i_{rq} = 0 \\ g\dfrac{M}{L_s} V_s + gw_s \sigma L_r i_{rd} = 0 \end{cases} \Rightarrow \begin{cases} V_{rd} = R_r . i_{rd} + \sigma L_r \dfrac{di_{rd}}{dt} \\ V_{rq} = R_r . i_{rq} + \sigma L_r \dfrac{di_{rq}}{dt} \end{cases} \quad \text{(II.51)}$$

Using the Laplace transform, we get:

$$\begin{cases} \dfrac{I_{rd}}{V_{rd}} = \dfrac{1}{R_r + \sigma L_r s} \\ \dfrac{I_{rq}}{V_{rq}} = \dfrac{1}{R_r + \sigma L_r s} \end{cases} \quad \text{(II.52)}$$

The closed-loop of the direct rotor current regulator and the quadratic rotor current regulator are shown in Figure II.14.

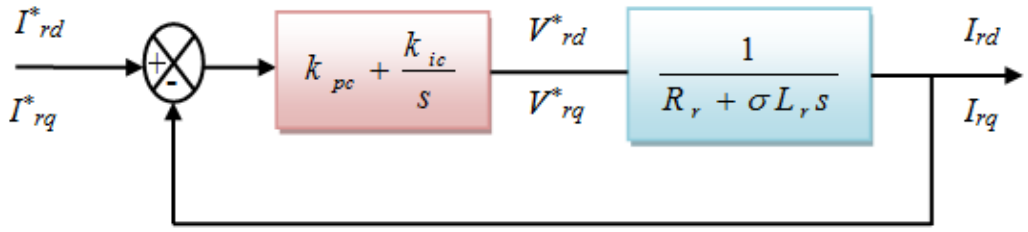

Figure II.14 The closed-loop scheme of PI corrector for P_s and Q_s regulation

In (II.52), it is noted that the machine system is symmetrical at both the d and q axes. As a result, the gains of the PI regulator are also symmetrical at these two axes.

The transform function of the PI corrector to regulate the rotor current is given as:

$$PI(s) = k_{pc} + \frac{k_{ic}}{s} \quad \text{(II.53)}$$

The OLTF in Figure II.14 is given by:

$$OLTF(s) = \frac{k_{ic}}{s}\left(\frac{k_{pc}}{k_{ic}} s + 1\right)\left(\frac{(1/R_r)}{(s\sigma T_r + 1)}\right) \quad \text{(II.54)}$$

where $T_r = R_r / L_r$

By applying the pole compensation method, between PI corrector and machine system, we find:

$$\frac{k_{pc}}{k_{ic}} = \sigma T_r \tag{II.55}$$

Therefore, OLTF becomes as:

$$OLTF(s) = \frac{k_{ic}}{R_r s} \tag{II.56}$$

The CLTF relation in Figure II.14 is given by:

$$CLTF(s) = \frac{\frac{k_{ic}}{R_r s}}{1 + \frac{k_{ic}}{R_r s}} = \frac{1}{1 + \frac{R_r}{k_{ic}} s} \tag{II.57}$$

By matching between (II.48) and (II.57), we find:

$$\tau = \frac{R_r}{k_{ic}} \tag{II.58}$$

Finally, the gains (K_{pc}, K_{ic}) of the PI corrector is given by:

$$\begin{cases} K_{ic} = \dfrac{R_r}{\tau} \\ K_{pc} = K_i \sigma T_r = \dfrac{\sigma L_r}{\tau} \end{cases} \tag{II.59}$$

II.4.2.2 IDPC with Power Loops using PI controller of DFIG

Unlike DPC, which only regulates the currents in the rotor, this method takes into consideration the coupling between the rotor currents and powers, and uses two PI controllers for each axis to regulate the currents and powers as shown in Figure II.15 [Boude 19].

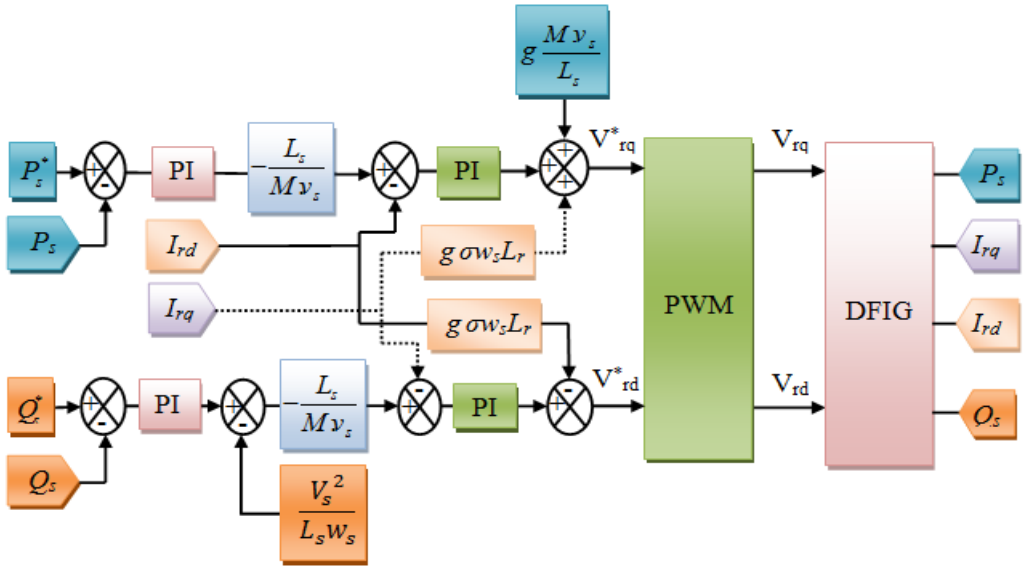

Figure II.15 IDPC with power loops using PI controller of DFIG

Dimensioning of the PI Regulator

We have previously calculated the dimensions of the PI corrector that regulates the rotor currents (I_{rd}, I_{rq}) and converts them into reference rotor voltages (V^*_{rd}, V^*_{rq}). Now, we will calculate the dimensions of the PI corrector that regulates the stator powers (P_s, Q_s) and converts them into reference rotor currents (I^*_{rd}, I^*_{rq}), as shown in Figure II.16.

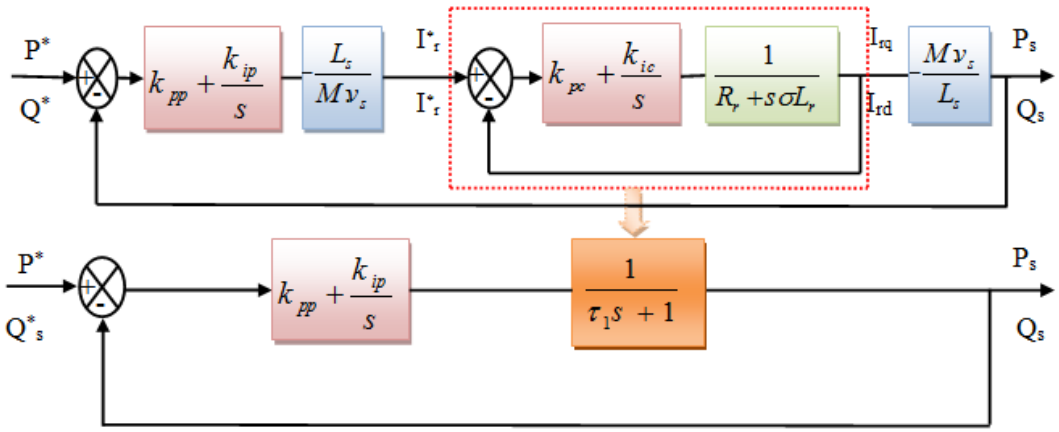

Figure II.16 The closed-loop scheme of PI corrector for P_s and Q_s regulation

Referring to (II.52), we note that the machine system is symmetric about the d and q-axes, resulting in symmetric gains of the PI regulator along these two axes.

The transform function of the PI corrector to regulate the stator power (P_s, Q_s) is given as:

$$PI(s) = k_{pp} + \frac{k_{ip}}{s} \tag{II.60}$$

The OLTF in Figure II.16 is given by:

$$OLTF(s) = \frac{k_{ip}}{s}\left(\frac{k_{pp}}{k_{ip}}s + 1\right)\left(\frac{1}{(\tau_1 s + 1)}\right) \tag{II.61}$$

By applying the pole compensation method, we find:

$$\frac{k_{pp}}{k_{ip}} = \tau_1 \tag{II.62}$$

Therefore, OLTF becomes as follows:

$$OLTF(s) = \frac{k_{ip}}{s} \tag{II.63}$$

The CLTF relation in Figure II.16 is given by:

$$CLTF(s) = \frac{\frac{k_{ip}}{s}}{1 + \frac{k_{ip}}{s}} = \frac{1}{1 + \frac{1}{k_{ip}}s} \tag{II.64}$$

By matching between (II.48) and (II.64), we find:

$$\tau_2 = \frac{1}{k_{ip}} \tag{II.65}$$

Finally, the gains (K_{pp}, K_{ip}) of the PI corrector is given by:

$$\begin{cases} K_{ip} = \dfrac{1}{\tau_2} \\ K_{pp} = K_{ip}.\tau_1 = \dfrac{\tau_1}{\tau_2} \end{cases} \tag{II.66}$$

II.5 Simulation results

In this simulation, the rotor of DFIG is controlled using an inverter fed by a DC voltage source, which is regulated using PI controller. The simulation results of the studied system are validated and presented using MATLAB/Simulink.

II.5.1 Test with fixed wind speed

To investigate the performance of the rotor control mechanisms applied to the DFIG, the generator is operated at a fixed nominal speed of 150.8 rad/s. The reference active and reactive power echelons are applied to each type of PI controller strategy, and these echelons are listed in Table II.1 along with their corresponding time variations.

Table II.1 Reference active and reactive power echelons

Time (s)	P_s^*	Q_s^*
0 to 1.5	0	0
1.5 to 2.25	-3300	0
2.25 to 3	-3300	3000
3 to 3.5	-5800	3000
3.5 to 4	-5800	-2500
4 to 5	-750	-2500

- **Simulation Results of IDPC with Power Loops at fixed speed WT**

The stator active and reactive powers and their corresponding references using IDPC with power loops are shown in Figs. II.17 (a) and II.17 (b), respectively. The stator and rotor currents using IDPC with power loops are shown in Figs. II.18 (a) and II.18 (b).

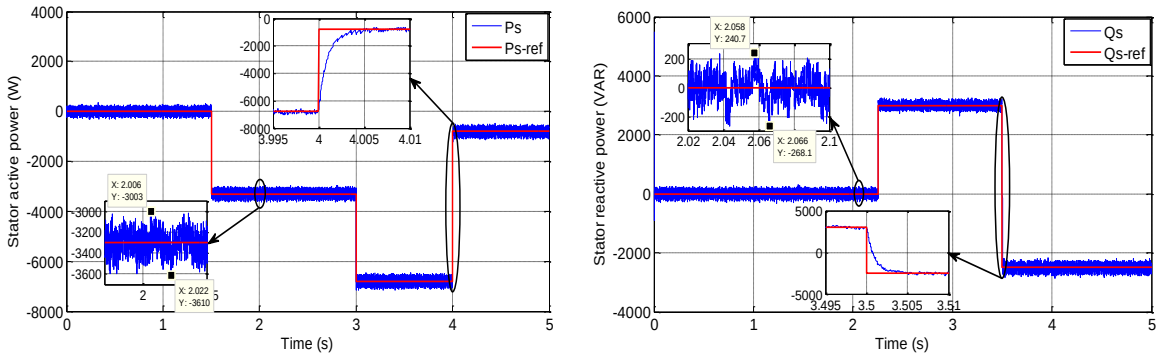

(a) (b)

Figure II.17 (a) Stator active and (b) reactive powers using IDPC with power loops

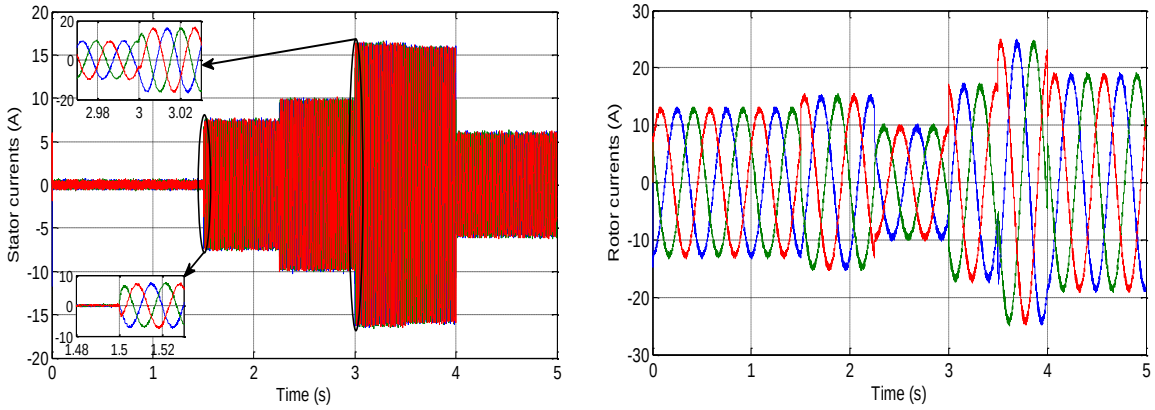

(a) (b)

Figure II.18 (a) Stator and (b) rotor currents using IDPC with power loops

We note from Figure II.17 that IDPC using power loops provides a slow response to track active and reactive power echelons without overshoot and undershoot, with a somewhat low ripple. However, when the power echelons differ, we notice a good separation between the d-axis (which corresponds to active power) and q-axis (which corresponds to reactive power) with slight fluctuations. We also note from Fig. II.18 that the three-phase stator and rotor currents have a sinusoidal nature, with a significant decrease in harmonics.

- **Simulation Results of IDPC without power loops at fixed speed WT**

The stator active and reactive powers and its reference using IDPC without power loops are shown in Figs. II.19 (a) and II.19 (b), respectively. The stator and rotor currents using IDPC with power loops are shown in Figs. II.20 (a) and II.20 (b), respectively.

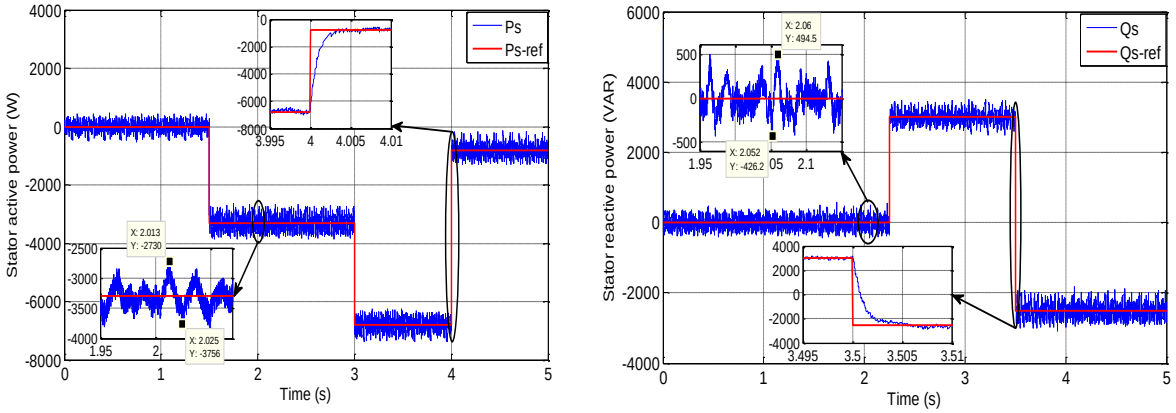

(a) (b)

Figure II.19 (a) Stator active and (b) reactive powers using IDPC without power loops

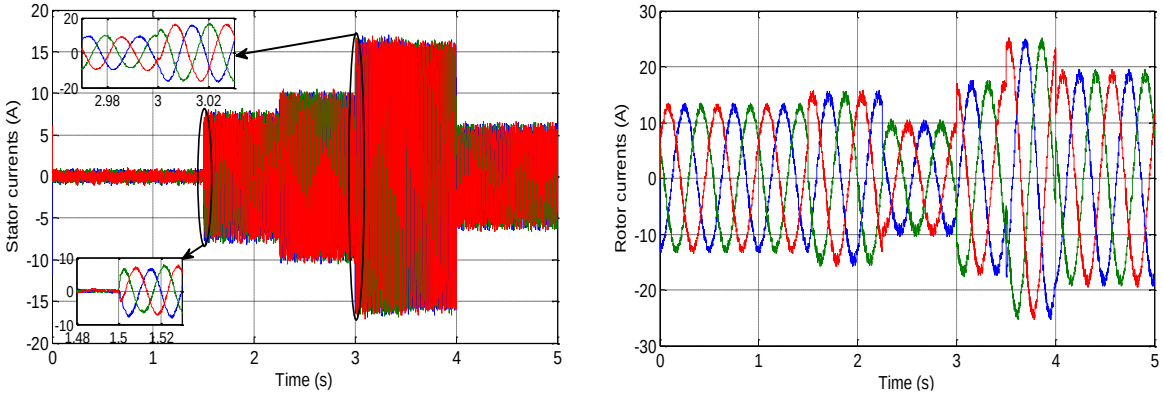

(a) (b)

Figure II.20 (a) Stator and (b) rotor currents using IDPC without power loops

We note from Figure II.19 that the IDPC without the power loops provides a faster response in order to track the active and reactive power echelons with no-overshoot and no-undershoot and some extent high ripple, nevertheless, when the power echelons different, we notice a good separation between the d-axis, corresponding to the stator active power, and q-axis, corresponding to the stator reactive power, with some slight fluctuations. We note from Fig. II.20 that the three-phase stator and rotor currents are sinusoidal in nature, with rather high harmonics.

II.5.2 Test with variable wind speed

The wind speed of a randomly variable nature was applied and the reference stator active power was derived using MPPT strategy to find out the robustness of vector control applied to rotor of DFIG. The wind speed curve that allows to rotate the WT blades, is displayed in Fig. II.21, where its value changes very randomly from1.79 to 11.75 $m.s^{-1}$, during 3.5 s. The rotor speed curve derived from a WT driven by wind speed is displayed in Fig. II.22, where its value changes very randomly from 0 to 154.1 $rad.s^{-1}$. The DFIG adapts well to very randomly changing wind speeds, which makes it more widely used nowadays.

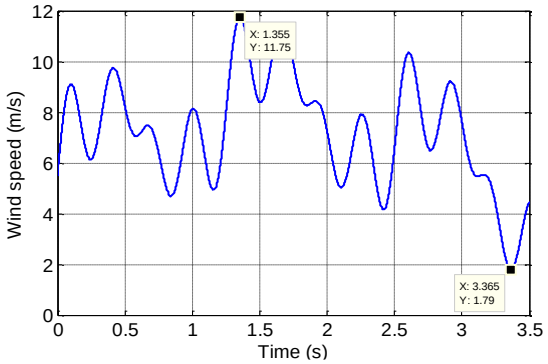

Figure II.21 Wind speed

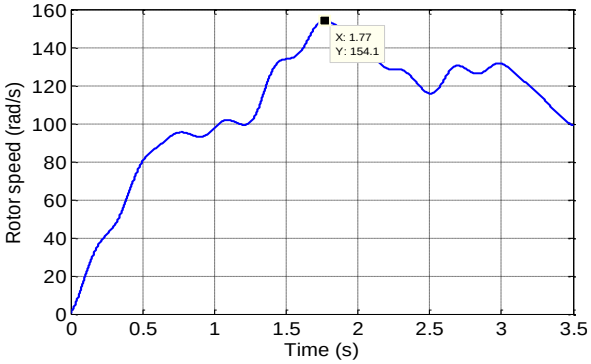

Figure II.22 Rotor speed

- **Simulation Results of IDPC with Power Loops at variable speed WT**

IDPC with power loops is a control strategy that utilizes both current loops and power loops. These loops are designed with a PI controller. The stator active power (blue line) and its reference profile (red line) of DFIG driven by variable speed WT integrated with the IDPC with power loops using PI-PWM and its zoom versus time in the transitional regime at start-up and between moments 2.23s and 2.28s are shown in Fig. II.23 (a). The reference of stator power ($P_{s\text{-}ref}$) is calculated by multiplying the mechanical speed (W_m) of the rotor by the reference of electromagnetic torque ($T_{em\text{-}ref}$), which is determined using MPPT. This calculation ensures that the system can generate maximum power at all power points. Fig. II.23 (b) presents the stator reactive power (blue line) and its reference profile (red line) of a DFIG that is driven by a variable speed WT. The control strategy used in this system is IDPC with power loops, which is implemented using PI-PWM. Additionally, the figure includes a zoomed-in view of the transitional regime during start-up and between the time intervals of 2.15s and 2.25s. The reference value of stator reactive power, is always maintained at zero ($Q_{s\text{-}ref}$=0) to ensure a unit power factor (PF = 1). The three-phase stator currents are displayed with their zoom using IDPC with power loops, and PI controller, as illustrated in Fig. II.24 (a). The frequency of the stator current is always constant (f_s=50 Hz) to synchronize it with the electrical grid. The three-phase rotor currents and their zoom can be observed in Fig. II.24 (b), which shows the results obtained using indirect control with power loops using PI-PWM. The frequency of the rotor currents is directly related to the rotor speed (ω_m).

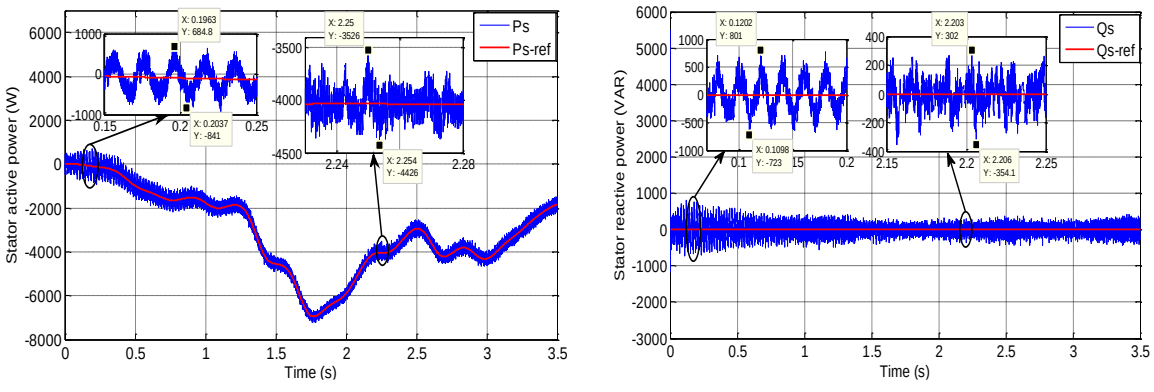

(a) (b)

Figure II.23 (a) Stator active and (b) reactive powers using IDPC with power loops

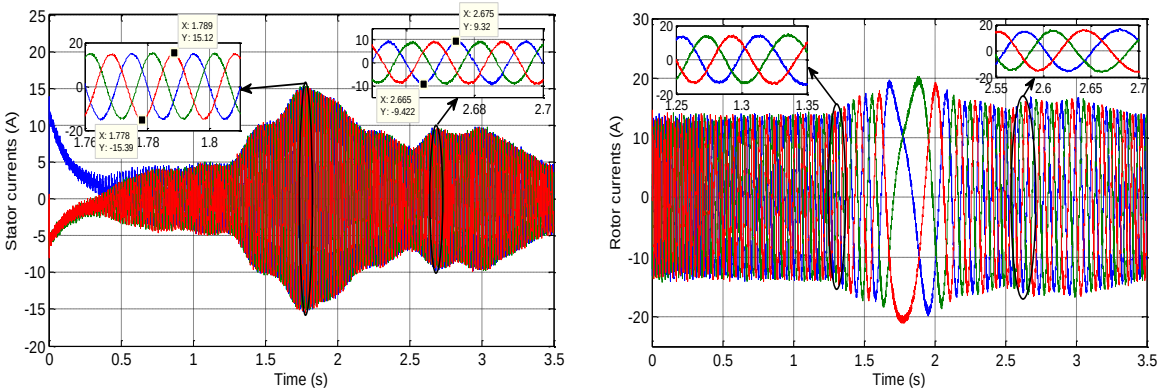

(a) (b)

Figure II.24 (a) Stator and (b) rotor currents using IDPC with power loops

We note from Figure II.23 that the stator active and reactive powers, when using IDPC with power loops provide greater stability during the transitional regime at start-up and lower ripple. Additionally, we notice from Fig. II.24 that the three-phase stator and rotor currents exhibit sinusoidal characteristics with relatively minor disturbances. Furthermore, we observe that the amplitude of the stator and rotor currents varies with changes in wind speed.

- **Simulation results of IDPC without power loops at variable speed WT**

IDPC without power loops is based on current loops using only a PI controller. The currents reference signal (I^*_{rq}, I^*_{rd}) are obtained from the powers reference signal (P^*_s, Q^*_s). Fig. II.25 (a) shows the stator active power and its reference of a DFIG driven by a variable speed WT integrated with IDPC without power loops using PI-PWM, and its zoom versus time in the transitional regime at start-up and between moments 2.2s and 2.26s. Similarly, Fig. II.25 (b) shows the stator reactive power and its reference of the DFIG driven by a variable speed WT integrated with IDPC control without power loops using PI-PWM, and its zoom versus time in the transitional regime at start-up and between moments 2s and 2.25s. Fig. II.26 (a) shows the three-phase stator currents and their zoom versus time using IDPC without power loops using PI-PWM. Similarly, Fig. II.26 (b) shows the three-phase rotor currents and their zoom versus time using IDPC without power loops using PI-PWM. It is noteworthy that from Fig. II.25, the use of IDPC without power loops results in greater stability in the transitional regime at start-up with high ripples of stator active and reactive powers compared to IDPC with power loops. From Fig. II.26, we note that the three-phase stator and rotor currents have a sinusoidal nature, with relatively lower disturbance.

Additionally, we note that the amplitude of the stator and rotor currents varies with changes in wind speed.

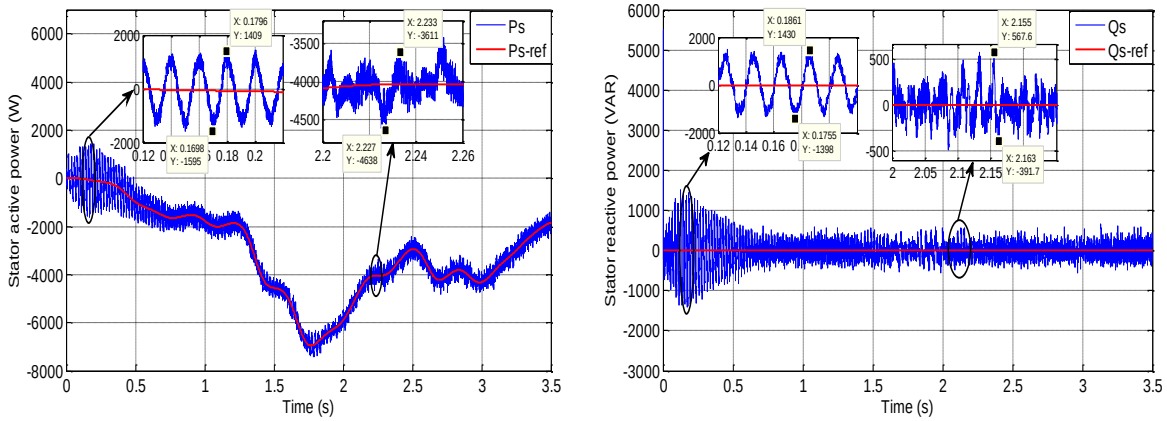

(a) (b)

Figure II.25 (a) Stator active and (b) reactive powers using IDPC without power loops

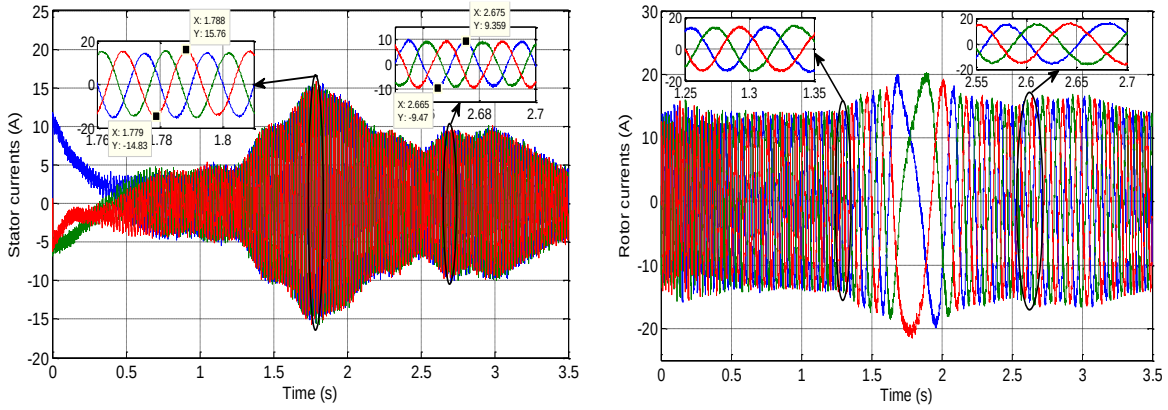

(a) (b)

Figure II.26 (a) Stator and (b) rotor currents using IDPC without power loops

The results of the performance comparison between IDPC without power loops and IDPC with power loops, in the case of fixed and variable wind speeds, have been summarized in Table II.2.

Table II.2 Performance comparison between IDPC without and with power loops

Technique / Performance	IDPC without power loops	IDPC with power loops
Response time of stator active power (s)	0.0035	0.005
Ripples of P_s (W)	1027	900
Ripples of Q_s (VAR)	959.3	656.1
Transitional system ripple at start-up of P_s (W)	3004	1525.8
Transitional system ripple at start-up of Q_s (VAR)	2828	1524

We can see from Table II.2 that indirect power control without power loops provides a faster response time; however, it results in more ripples in the steady-state and transitional system at start-up compared to indirect power control with power loops.

II.6 Conclusion

In this chapter, we have conducted a theoretical study on the modeling and control of a wind energy conversion system based on DFIM used as a generator. Initially, the WT was controlled using MPPT strategy to obtain the maximum power that this turbine can produce. However, to convert the mechanical power into electrical power, the WT was coupled with a DFIG, which tracks the stator active power reference obtained from the MPPT strategy. The reference stator reactive power is set to zero. To track the reference signals, the rotor of DFIG is controlled using three different methods with a classical PI controller. The first method is DPC with PI controller without using current loops. While easy to implement, this method is not robust or effective. The second method is IDPC with power loops, which uses four PI controllers, including two PI controllers of power loops and two PI controllers of rotor currents loops. The third method is IDPC without power loops, which uses only two PI controllers for rotor current loops. This method is simpler to implement than the second method, and therefore, we will continue our research using this method and replace the classical controllers with advanced control techniques.

Chapter III
Advanced Control of DFIG using Backstepping Control

III.1 Introduction

The backstepping control (BSC) has received significant attention since its invention and has been widely applied to solve control problems in electrical systems, mechanical engineering, aerospace engineering, and other fields. Over several years of research and studies, this method has been developed comprehensively and systematically to a large extent. For example, it has been successfully applied to nonlinear damping and systems with uncertain parameters [Zhan 20]. BSC theory is a technique used in nonlinear systems, developed by Petar V. Kokotovic and others since about 1990. It is used to design stabilizing control elements for a special class of nonlinear dynamic systems, including systems with uncertain parameters. These systems are built from subsystems that radiate out from an irreducible subsystem that can be stabilized using some other method. Due to this iterative architecture, the designer can start the design process at the known-stable system and "back out" new controllers that incrementally install each external subsystem. The process ends when the final external control is reached, hence known as the BSC [Abb 12-13]. To stabilize a nonlinear dynamical system, the Lyapunov function approach can be used. This approach is applied to the backstepping technique at each step of the dynamical system in an iterative manner to stabilize the system's origin in strict feedback. As a result, the error and its derivative settle down to zero [Abd 18]. The objective of this chapter is to provide a theoretical study of the backstepping controller and its mathematical model, using the Lyapunov function to fulfill the stability condition by backstepping relation. The chapter applies the BSC to control the rotor of DFIG, to control the stator active and reactive powers, achieving stability in nonlinear systems and uncertainties. Additionally, the chapter examines the robustness of the control system when the parameter variation of DFIG occurs. The numerical simulation results applied in this chapter are presented using the Matlab/Simulink program.

III.2 Concept of Backstepping Control

The backstepping approach is a recursive control design technique used in nonlinear feedback control systems. This approach uses a virtual control to decompose a complex nonlinear design problem into several simpler design steps, resulting in stability in highly nonlinear dynamic systems. The basic idea of backstepping design is to recursively select appropriate functions of state variables as pseudo control inputs for lower dimension subsystems of the overall system. At each backstepping stage, a new pseudo control design is generated, expressed in terms of the pseudo control designs from preceding design stages. When the design procedure terminates, a feedback design for the true control input is achieved by an efficient original design objective. This objective is formed by summing up the Lyapunov functions associated with each individual design stage, which is used to drive the virtual control [Men 18] [Lag 11].

III.2.1 Lyapunov Function

Lyapunov functions are scalar functions used to demonstrate the stability of an equilibrium of an ordinary differential equation in the theory of ordinary differential equations. These functions are named after the Russian mathematician Aleksandr Mikhailovich Lyapunov, and they play a crucial role in stability theory and control theory. In many classes of ordinary differential equations, the existence of Lyapunov functions is both a necessary and sufficient condition for stability. Although there is no general technique for constructing Lyapunov functions for ordinary differential equations, the construction of Lyapunov functions is known for many specific cases. Informally, a Lyapunov function is a function that takes positive values everywhere except at the equilibrium and decreases or is non-increasing along every trajectory of the ordinary differential equation. The primary benefit of Lyapunov function-based stability analysis of ordinary differential equations is that it does not require the actual solution, whether analytical or numerical, of the ordinary differential equation [Abb 12-13].

III.2.1.1 Methods of Lyapunov's theory

Basic Lyapunov theory encompasses two techniques developed by Lyapunov: the indirect method and the direct method. The indirect method, also known as the linearization method, asserts that the stability characteristics of a nonlinear system near an equilibrium point are fundamentally comparable to those of its linearized approximation. The method serves as the theoretical justification for using linear control for physical systems, which are always

inherently nonlinear. The direct method is a powerful tool for nonlinear system analysis, and therefore the so-called Lyapunov analysis often actually refers to the direct method. The direct method is a generalization of the energy concepts associated with a mechanical system: the motion of a mechanical system is stable if its total mechanical energy decreases all the time. In using the direct method to analyze the stability of a nonlinear system, the idea is to construct a scalar energy-like function (a Lyapunov function) for the system, and to see whether it decreases. The power of this method comes from its generality: it is applicable to all kinds of control systems, be they time-varying or time-invariant, finite dimensional or infinite dimensional. Conversely, the limitation of the method lies in the fact that it is often difficult to find a Lyapunov function for a given system. Although Lyapunov's direct method is originally a method of stability analysis, it can be used for other problems in nonlinear control. One important application is the design of nonlinear controllers. The idea is to somehow formulate a scalar positive function of the system states, and then choose a control law to make this function decrease. A nonlinear control system thus designed will be guaranteed to be stable. such a design approach has been used to solve many complex design problems, e.g., in robotics and adaptive control. The direct method can also be used to estimate the performance of a control system and study its robustness [Slo 91].

III.2.1.2 Principles of stability according to Lyapunov

Stability theory holds a crucial role within engineering systems. For any given control system, ensuring stability is essential, as an unstable control system holds no utility. The Lyapunov stability provides a broad and valuable method for assessing the stability of nonlinear systems [Puk 11].

We consider the first-order controlled system is as follows:

$$\dot{x} = f(x) \tag{III.1}$$

The system is assumed to start operating at the initial value $x(0)$, assuming that x_e is the equilibrium point of the system, which achieve the function is equal to zero $f(x_e) = 0$, at this point. Since we have a spherical field (B_R) with radius (R) and identifier in the state space $\|x\| < R$, and a spherical surface (S_R) identifier with $\|x\| = R$, also this space contains another spherical field (B_R) where $r < R$, as shown in the figure (4.1), which shows the principle of stability through the curves that the systems follow, starting from their initial value towards the equilibrium point. For three types of systems such as marginally stable

systems, asymptotically stable, and unstable systems, we can say that the equilibrium point is stable if one of the following conditions is satisfied.

$$\forall\, R > 0,\ \exists\, r > 0,\ if\ \|x(0) - x_e\| < r \Rightarrow \|x(t) - x_e\| < R, for\ all\ \ t \geq 0 \qquad \text{(III.2)}$$

Based on Figure (4.1), it can be inferred that for any value of $R > 0$, there exists a value $r > 0$ such that if the difference between the initial value of the system $x(0)$ and the equilibrium point x_e is less than r, then the difference between the two values will also be less than R for all $t \geq 0$. However, if the distance difference between the initial value and the equilibrium point is greater than or equal to r, then the equilibrium point is not stable.
If the preceding condition is satisfied, i.e., the equilibrium point is stable and the distance between the initial value and the equilibrium point is less than r, then the system is said to be asymptotically stable. In this case, $x(t)$ will converge to the equilibrium point x_e as time approaches infinity.

$$\|x(0) - x_e\| < r \ \Rightarrow\ x(t) \to x_e\ as\ t \to \infty \qquad \text{(III.3)}$$

Global asymptotic stability is achieved when the system is asymptotically stable for all possible initial conditions or primitive values of state variables (solutions of the system), not just for a subset of them. In other words, if the system is globally asymptotically stable, then any initial condition will converge to the same unique equilibrium point as time approaches infinity. This is a desirable property for designing nonlinear control systems because it ensures that the system will converge to the desired equilibrium point regardless of the initial conditions or inputs applied to the system.

When studying the stability of a given system, it is essential to understand the function $v(x)$ that describes the stability properties of the system. This function is typically a Lyapunov function, which is a scalar function that assigns a positive value to each point in the state space of the system. The function $v(x)$ should satisfy the following conditions:

- $v(x)$ is continuous and differentiable.
- $v(x)$ is positive definite, meaning that $v(0) = 0$ and $v(x) > 0$ for all $x \neq 0$.
- $v(x)$ has a negative definite derivative, meaning that $\partial v(x)/\partial x$ is negative definite for all x in the state space except for the equilibrium points, where it is zero.

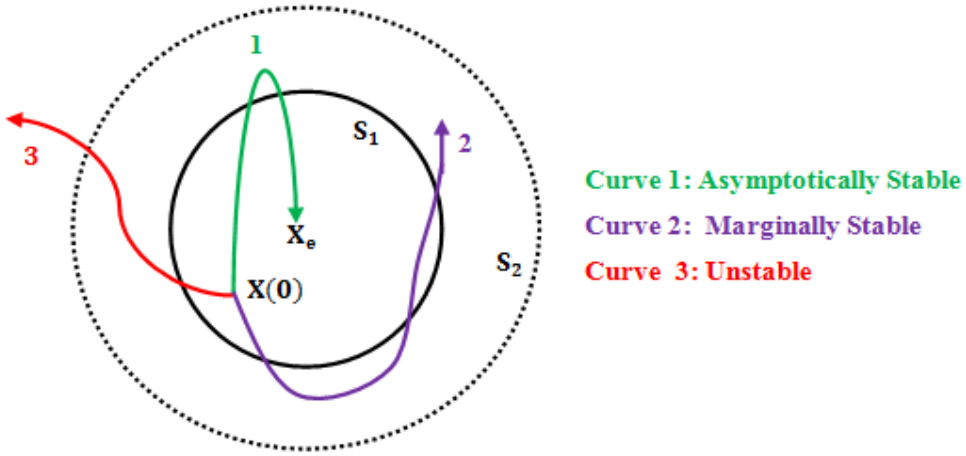

Figure III.1 Principles of stability according to Lyapunov

III.3 Backstepping Control of DFIG

The BSC approach involves multiple steps, with each step dealing with a simpler single-input single-output design problem, providing a reference for the next design step. The stability and performance of the overall system are achieved by a Lyapunov function [Nad 17]. In this section, BSC is proposed to control the active and reactive power of the stator due to its good performance which ensures the stability of the system based on Lyapunov's theory. To control the DFIG rotor using BSC, we have implemented this technique in two methods [Dou 15].

III.3.1 DPC using BSC

From (II.40), the rotor currents derivative is extracted as follows:

$$\begin{cases} \dot{I}_{qr} = \dfrac{1}{\sigma L_r} v_{qr} - \dfrac{1}{\sigma T_r} I_{qr} - g w_s I_{dr} - g \dfrac{L_m v_s}{\sigma L_r L_s} \\ \dot{I}_{dr} = \dfrac{1}{\sigma L_r} v_{dr} - \dfrac{1}{\sigma T_r} I_{dr} + g w_s I_{qr} \end{cases} \tag{III.4}$$

The stator active and reactive powers errors are defined:

$$\begin{cases} e_1 = P_s^{ref} - P_s \\ e_3 = Q_s^{ref} - Q_s \end{cases} \tag{III.5}$$

The derivative of (III.5) is as follows:

$$\begin{cases} \dot{e}_1 = \dot{P}_s^{ref} - \dot{P}_s \\ \dot{e}_3 = \dot{Q}_s^{ref} - \dot{Q}_s \end{cases} \tag{III.6}$$

By deriving (II.38) and (II.39) and substituting them into (III.6), we obtain:

$$\begin{cases} \dot{e}_1 = \dot{P}_s^{ref} + v_s \dfrac{L_M}{L_s} \dot{I}_{rq} \\ \dot{e}_3 = \dot{Q}_s^{ref} + v_s \dfrac{L_M}{L_s} \dot{I}_{rd} \end{cases} \tag{III.7}$$

By substituting (III.4) into (III.7), we get:

$$\begin{cases} \dot{e}_1 = \dot{P}_s^{ref} + v_s \dfrac{L_M}{L_s} \left(\dfrac{1}{\sigma L_r} v_{qr} - \dfrac{1}{\sigma T_r} I_{qr} - g w_s I_{dr} - g \dfrac{L_m v_s}{\sigma L_r L_s} \right) \\ \dot{e}_3 = \dot{Q}_s^{ref} + v_s \dfrac{L_M}{L_s} \left(\dfrac{1}{\sigma L_r} v_{dr} - \dfrac{1}{\sigma T_r} I_{dr} + g w_s I_{qr} \right) \end{cases} \tag{III.8}$$

We can choose the Lyapunov function V_1 associated with the active and reactive power errors, as follows:

$$V_1 = \frac{1}{2} e_1^2 + \frac{1}{2} e_3^2 \tag{III.9}$$

The derivative of (III.9) is as follows:

$$\dot{V}_1 = e_1 \dot{e}_1 + e_3 \dot{e}_3 \tag{III.10}$$

Using (III.8) and (III.10), we find:

$$\begin{aligned} \dot{V}_1 = e_1 \left(\dot{P}_s^{ref} + v_s \frac{L_M}{L_s} \left(\frac{1}{\sigma L_r} v_{qr} - \frac{1}{\sigma T_r} I_{qr} - g w_s I_{dr} - g \frac{L_m v_s}{\sigma L_r L_s} \right) \right) + e_3 \left(\dot{Q}_s^{ref} + \right. \\ \left. v_s \frac{L_M}{L_s} \left(\frac{1}{\sigma L_r} v_{dr} - \frac{1}{\sigma T_r} I_{dr} + g w_s I_{qr} \right) \right) \end{aligned} \tag{III.11}$$

Equation (III.11) can be rewritten as follows:

$$\begin{aligned} \dot{V}_1 = -k_1 e_1^2 - k_3 e_3^2 + e_1 \left(\dot{P}_s^{ref} + v_s \frac{L_m}{L_s} \left(\frac{1}{\sigma L_r} v_{qr} - \frac{1}{\sigma T_r} I_{qr} - g w_s I_{dr} - g \frac{L_m v_s}{\sigma L_r L_s} \right) + k_1 e_1 \right) + \\ e_3 \left(\dot{Q}_s^{ref} + v_s \frac{L_m}{L_s} \left(\frac{1}{\sigma L_r} v_{dr} - \frac{1}{\sigma T_r} I_{dr} + g w_s I_{qr} \right) + k_3 e_3 \right) \end{aligned} \tag{III.12}$$

where k_1, k_3 are positive constants.

To make the BSC system more stable and reduce the tracking error, it is necessary for the derivative of the Lyapunov function to always be negative, which can be expressed as:

$$\dot{V}_1 = -k_1 e_1^2 - k_3 e_3^2 \leq 0 \tag{III.13}$$

By applying the condition of (III.13) to (III.12), we get:

$$\begin{cases} \dot{P}_s^{ref} + v_s \dfrac{L_m}{L_s}\left(\dfrac{1}{\sigma L_r} v_{qr} - \dfrac{1}{\sigma T_r} I_{qr} - g w_s I_{dr} - g \dfrac{L_m v_s}{\sigma L_r L_s}\right) + k_1 e_1 = 0 \\ \dot{Q}_s^{ref} + v_s \dfrac{L_m}{L_s}\left(\dfrac{1}{\sigma L_r} v_{dr} - \dfrac{1}{\sigma T_r} I_{dr} + g w_s I_{qr}\right) + k_3 e_3 = 0 \end{cases} \quad \text{(III.14)}$$

Using (III.14), the reference rotor voltages can be written as follows:

$$\begin{cases} v_{dr}^{ref} = \dfrac{\sigma L_r L_s}{L_m v_s}\left(-\dot{Q}_s^{ref} - k_3 e_3\right) + R_r I_{dr} - g w_s \sigma L_r I_{qr} \\ v_{qr}^{ref} = \dfrac{\sigma L_r L_s}{L_m v_s}\left(-\dot{P}_s^{ref} - k_1 e_1\right) + R_r I_{qr} + g w_s \sigma L_r I_{dr} + g \dfrac{L_m v_s}{L_s} \end{cases} \quad \text{(III.15)}$$

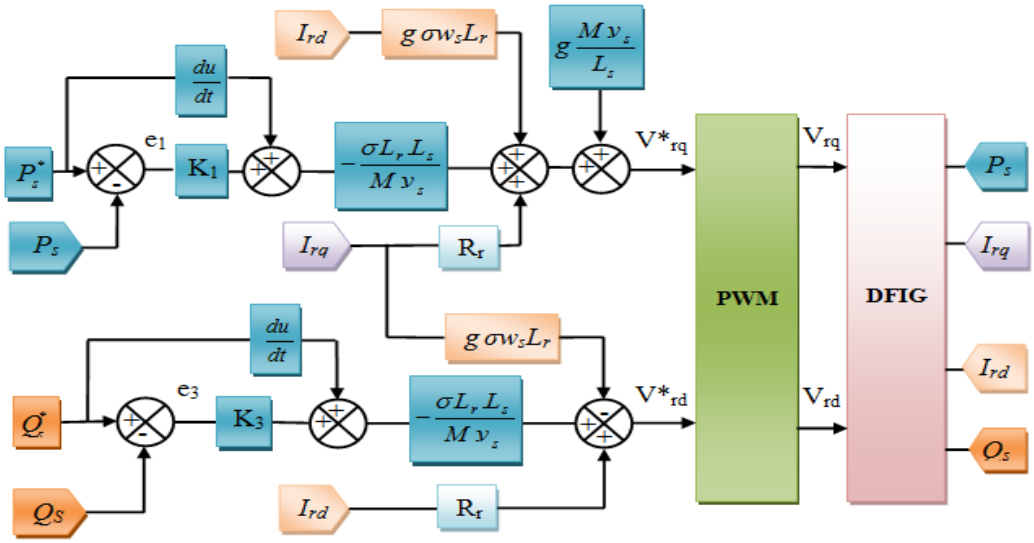

Figure III.2 Direct power control using BSC

III.3.2 IDPC using BSC

The reference active and reactive powers as a function of the reference rotor currents are given as follows:

$$\begin{cases} P_s^{ref} = -\dfrac{L_m v_s}{L_s} I_{qr}^{ref} \\ Q_s^{ref} = \dfrac{v_s^2}{L_s w_s} - \dfrac{L_m v_s}{L_s} I_{dr}^{ref} \end{cases} \quad \text{(III.16)}$$

The rotor currents errors are defined by:

$$\begin{cases} e_2 = I_{qr}^{ref} - I_{qr} \\ e_4 = I_{dr}^{ref} - I_{dr} \end{cases} \quad \text{(III.17)}$$

The derivative of (III.17) is as follows:

$$\begin{cases} \dot{e}_2 = \dot{I}_{qr}^{ref} - \dot{I}_{qr} \\ \dot{e}_4 = \dot{I}_{dr}^{ref} - \dot{I}_{dr} \end{cases} \tag{III.18}$$

By substituting (III.4) into (III.18), we get:

$$\begin{cases} \dot{e}_2 = \dot{I}_{qr}^{ref} - (\frac{1}{\sigma L_r} v_{qr} - \frac{1}{\sigma T_r} I_{qr} - g w_s I_{dr} - g \frac{L_m v_s}{\sigma L_r L_s}) \\ \dot{e}_4 = \dot{I}_{dr}^{ref} - (\frac{1}{\sigma L_r} v_{dr} - \frac{1}{\sigma T_r} I_{dr} + g w_s I_{qr}) \end{cases} \tag{III.19}$$

The Lyapunov function of the reference signal tracking errors is given by:

$$V_2 = \frac{1}{2}(e_2^2 + e_4^2) \tag{III.20}$$

By deriving (III.20), we find:

$$\dot{V}_2 = e_2 \dot{e}_2 + e_4 \dot{e}_4 \tag{III.21}$$

By substituting (III.19) into (III.21), we get:

$$\begin{aligned} \dot{V}_2 = &-k_2 e_2^2 - k_4 e_4^2 + e_2 (\dot{I}_{qr}^{ref} - (\frac{1}{\sigma L_r} v_{qr} - \frac{1}{\sigma T_r} I_{qr} - g w_s I_{dr} - g \frac{L_m v_s}{\sigma L_r L_s}) + k_2 e_2) + \\ & e_4 (\dot{I}_{dr}^{ref} - (\frac{1}{\sigma L_r} v_{dr} - \frac{1}{\sigma T_r} I_{dr} + g w_s I_{qr}) + k_4 e_4) \end{aligned} \tag{III.22}$$

where k_2, k_4 are positive constants.

In order to stabilize the control system, the derivative of the Lyapunov function should always be negative defined, as follows:

$$\dot{V}_2 = -k_2 e_2^2 - k_4 e_4^2 \leq 0 \tag{III.23}$$

By applying the condition of (III.23) to (III.22), we find:

$$\begin{cases} \dot{I}_{qr}^{ref} - (\frac{1}{\sigma L_r} v_{qr} - \frac{1}{\sigma T_r} I_{qr} - g w_s I_{dr} - g \frac{L_m v_s}{\sigma L_r L_s}) + k_2 e_2 = 0 \\ \dot{I}_{dr}^{ref} - (\frac{1}{\sigma L_r} v_{dr} - \frac{1}{\sigma T_r} I_{dr} + g w_s I_{qr}) + k_4 e_4 = 0 \end{cases} \tag{III.24}$$

Using (III.24), which describes the relationship between the reference rotor currents and voltages, the reference rotor voltages are written as:

$$\begin{cases} v_{dr}^{ref} = L_r\sigma(\dot{I}_{dr}^{ref} + k_4 e_4) + R_r I_{dr} - g w_s \sigma L_r I_{qr} \\ v_{qr}^{ref} = L_r\sigma(\dot{I}_{qr}^{ref} + k_2 e_2) + R_r I_{qr} + g w_s \sigma L_r I_{dr} + g\dfrac{L_m v_s}{L_s} \end{cases} \quad \text{(III.25)}$$

where k_2, k_4 are positive constants.

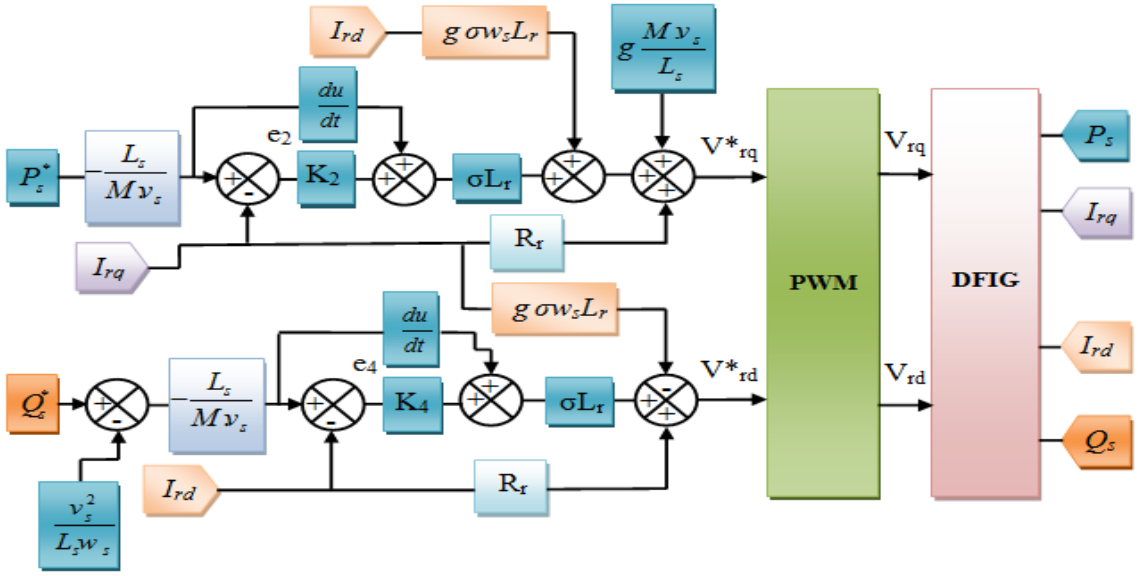

Figure III.3 IDPC using BSC

The utilization of BSC technology in both methods facilitates the attainment of convergence while ensuring overall system stability. The positive constants, namely k_1, k_2, k_3, and k_4, when chosen appropriately, ensure both stability and a rapid dynamic response.

III.4 Simulation Results

In this section of the simulation, the rotor of DFIG is supplied by an inverter connected to a DC voltage source. This inverter is controlled using BSC utilized in two methods: DPC using BSC and IDPC using BSC. The simulated system's results are validated and showcased using MATLAB/Simulink.

III.4.1 Test with fixed wind speed

To investigate the BSC behavior, both direct and indirect control of active and reactive powers using BSC are applied. First, DFIG is rotated at a fixed speed of 150.8 rad/s, which is close to the synchronous speed. The effectiveness of this control strategy is reflected in the control system's response time for tracking the reference signal and minimizing the ripple in active and reactive power. The active and reactive power echelons are listed in Table II.1, which is located in the second chapter.

III.4.1.1 DPC using BSC at fixed speed WT

The stator active and reactive powers, along with their zoomed-in views, are shown in Figs. III.4 (a) and III.4 (b), respectively, using DPC with BSC for DFIG is rotated at a fixed speed. The stator and rotor currents, along with their zoomed-in views, are shown in Figs. III.5 (a) and III.5 (b), respectively, using DPC with BSC for DFIG is rotated at a fixed speed. Upon observing the active and reactive power echelons depicted in Fig. III.4, it is evident that the implementation of DPC using BSC yields a faster response for tracking the reference signal, devoid of overshoot and undershoot. Additionally, it demonstrates excellent tracking precision, as well as a good separation and independence between the stator active power corresponding to the q-axis and the stator reactive power corresponding to the d-axis.

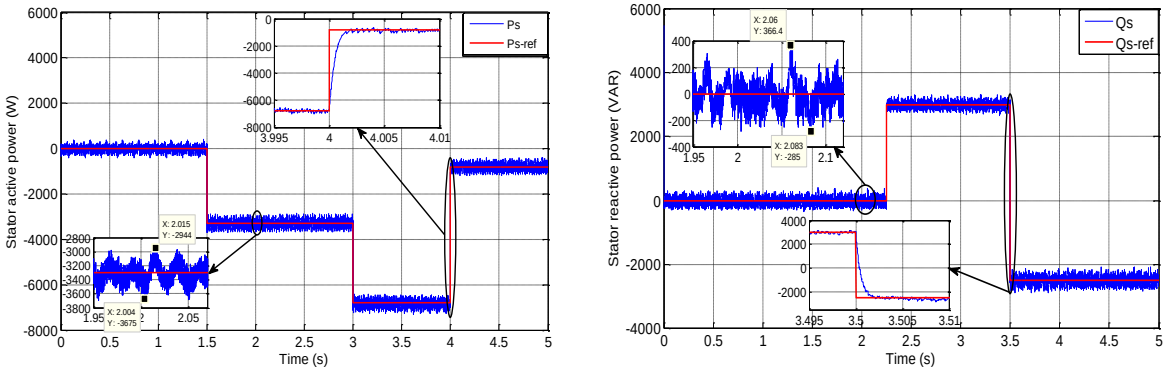

(a) (b)

Figure III.4 (a) Stator active and (b) reactive powers using DPC with BSC

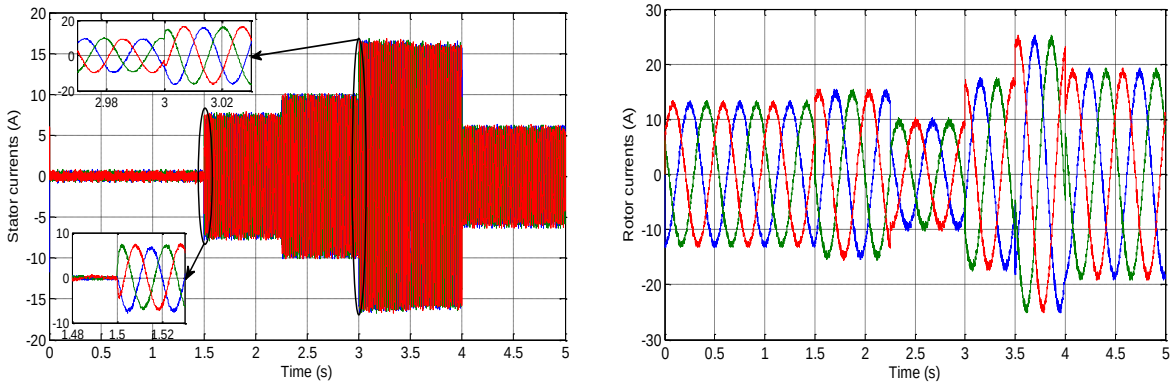

(a) (b)

Figure III.5 (a) Stator and (b) rotor currents using DPC with BSC

III.4.1.2 IDPC with BSC at fixed speed WT

The stator active and reactive powers, along with their zoomed-in views, are shown in Figs. III.6 (a) and III.6 (b), respectively, using IDPC with BSC for DFIG is rotated at a fixed speed. The stator and rotor currents, along with their zoomed-in views, are shown in

Figs. III.7 (a) and III.7 (b), respectively, using IDPC with BSC. When analyzing the active and reactive power echelons shown in Fig. III.6, it becomes apparent that the utilization of IDPC with BSC yields a faster response for reference signal tracking compared to DPC with BSC, Furthermore, it exhibits remarkable tracking accuracy of reference signal and maintains independence between the stator active power associated with the q-axis and the stator reactive power associated with the d-axis.

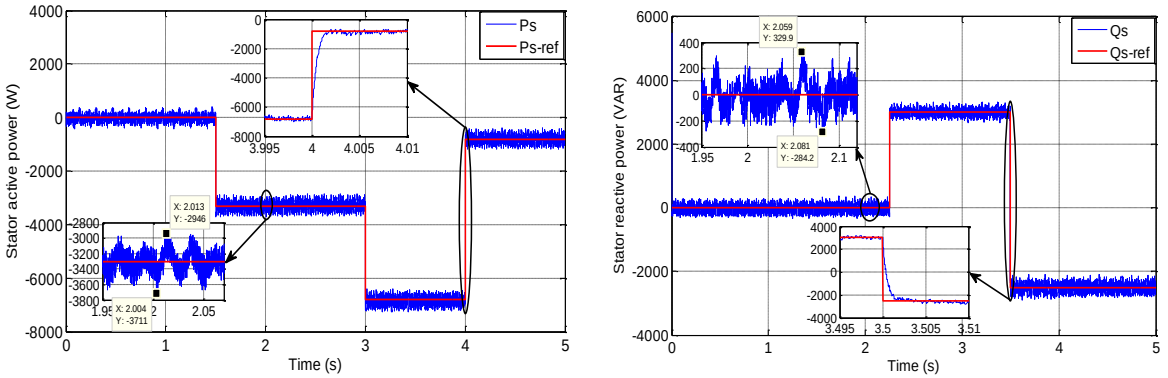

(a) (b)

Figure III.6 (a) Stator active and (b) reactive powers using IDPC with BSC

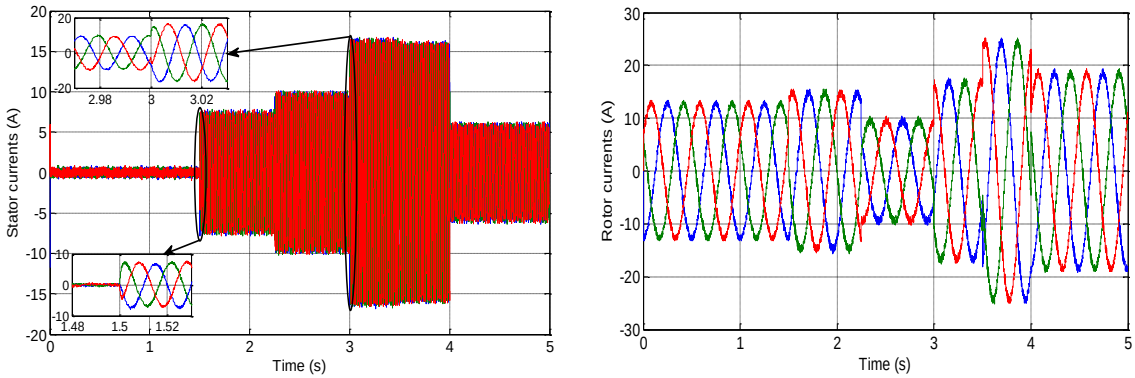

(a) (b)

Figure III.7 (a) Stator and (b) rotor currents using IDPC with BSC

III.4.2 Test with variable wind speed

DFIG is more adaptable and flexible for variable speed WTs, starting at lower wind speeds and extending to higher wind speeds. This part focuses on simulating DFIG driven by randomly variable-speed WTs and using the non-simplified model of DFIG to show the transient system of stator active and reactive powers. The control of the DFIG rotor using BSC is studied in two methods, namely DPC and IDPC.

III.4.2.1 DPC using BSC at variable speed WT:

In this section, the stator active and reactive powers are controlled directly using DPC with BSC for controlling the rotor of DFIG with a variable-speed WT. The reference active power is obtained from the WT using MPPT strategy to maximize the wind energy extraction. Simultaneously, the reactive power is consistently maintained at zero to achieve an optimal power factor close to unity.

The stator active and reactive powers and their zoomed-in views using DPC with BSC are shown in Figs. III.8 (a) and III.8 (b) respectively. The stator and rotor currents and their zoomed-in views using DPC with BSC for controlling the rotor of DFIG with a variable speed WT are shown in Figs. III.9 (a) and III.9 (b) respectively.

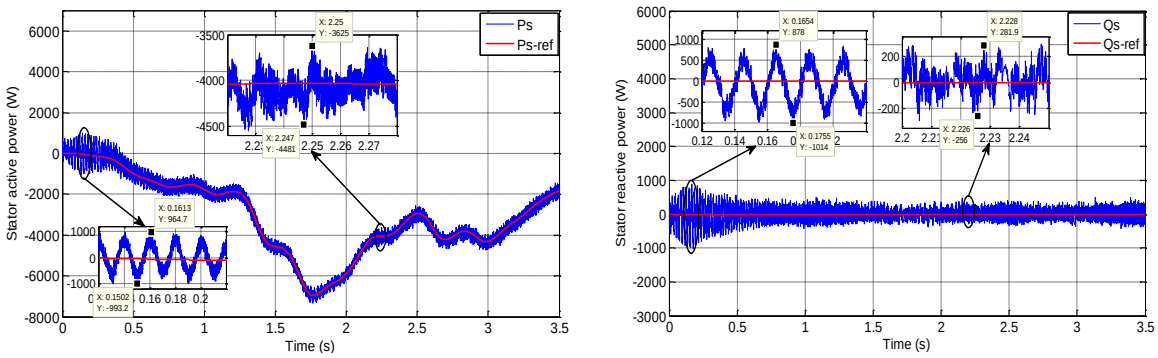

(a) (b)

Figure III.8 (a) Stator active and (b) reactive powers using DPC with BSC

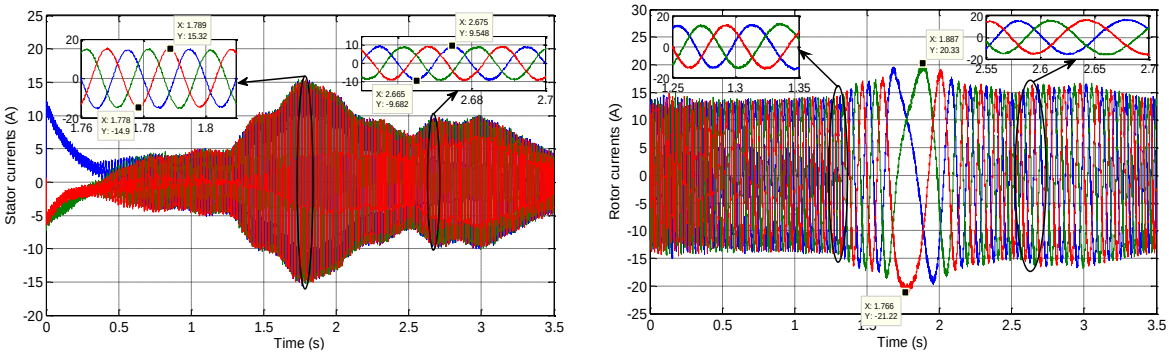

(a) (b)

Figure III.9 (a) Stator and (b) rotor currents using DPC with BSC

III.4.2.2 IDPC using BSC at variable speed WT:

In this section, the stator active and reactive powers and their zoomed-in views using IDPC with BSC for controlling the rotor of DFIG with a variable-speed WT are shown in Figs. III.10 (a) and III.10 (b) respectively. The stator and rotor currents and their zoomed-in views using IDPC with BSC are shown in Figs. III.11(a) and III.11(b) respectively.

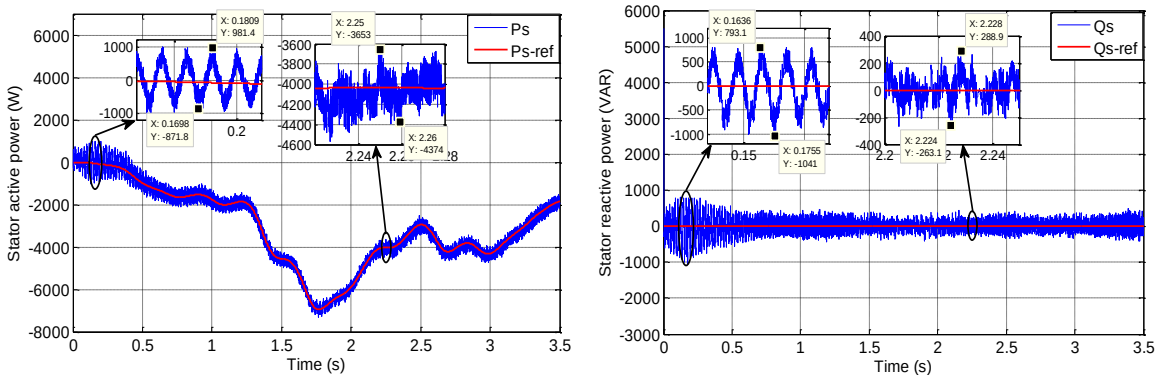

(a) (b)

Figure III.10 (a) Stator active and (b) reactive powers using IDPC with BSC

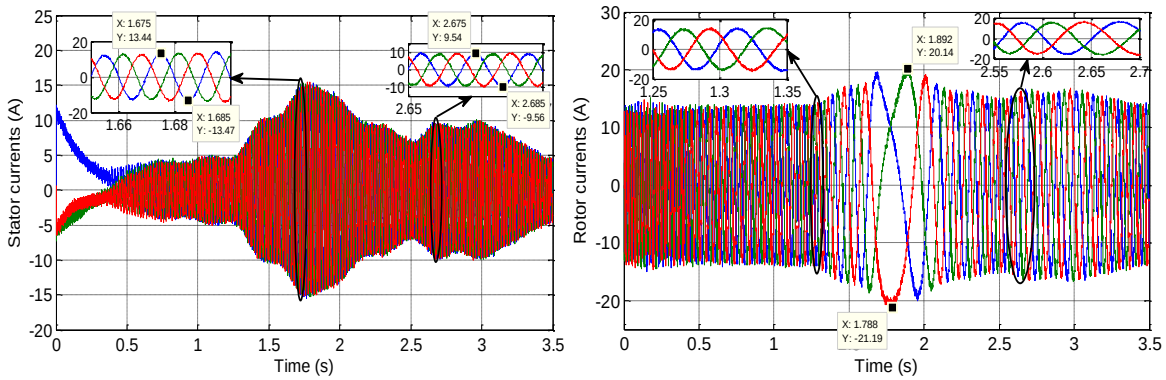

(a) (b)

Figure III.11 (a) Stator and (b) rotor currents using IDPC with BSC

The performance comparison results between DPC and IDPC using BSC at fixed and variable wind speed, are summarized in Table III.1.

Table III.1. Performance comparison between DPC and IDPC using BSC

Technique / Performance	DPC using BSC	IDPC using BSC
Response time of stator active power (s)	0.002	0.0018
Ripples of P_s (W)	856	721
Ripples of Q_s (VAR)	537.9	552
Transitional system ripple at start-up of P_s (W)	1957.9	1853.2
Transitional system ripple at start-up of Q_s (VAR)	1892	1834.1

III.5 Conclusion

In this chapter, we conducted a theoretical study on BSC for controlling the rotor of DFIG, which is an advanced and efficient control technique that relies on incremental adjustments to the output signal of a dynamic system. By doing so, this approach can enhance the performance and stability of the system. In the beginning, we investigated the application of BSC with DPC for controlling the DFIG rotor. This was achieved by first establishing the general model of the rotor voltages expressions using the Lyapunov function and selecting an appropriate gain to ensure stability. The implementation of this control method led to fast and accurate control of the active and reactive power output of the DFIG rotor, resulting in a more stable and reliable wind power generation system. Next, we investigated of BSC with IDPC, which relies only on rotor current loops without power loops, to regulate the control of DFIG rotor. IDPC using BSC provides good separation between stator active and reactive power, and lower ripple in both transitional and permanent systems. This leads to reduced THD of stator currents, and enhances the accuracy and efficiency of controlling the output of active and reactive power. In conclusion, BSC with both DPC and IDPC to regulate the control of DFIG rotor is a promising and dependable technology that ensures system stability and reliability for generating clean wind power. The simulation results were verified using a constant and randomly variable wind speed under MATLAB/Simulink.

Chapter VI

Robust Control of DFIG using Fuzzy Logic Control

IV.1 Introduction

Fuzzy logic is an innovative control technology since the sixties of the last century, nowadays, the interest in the field of this technique on the part of scientists has greatly increased, this strategy is widely used, especially in the field of devices used by humans (microwaves, robots, washing machines, ... and so on). The fuzzy logic controller (FLC) is an impressive technology that can smoothly handle fuzzy and non-linear systems. This invented technology is somewhat similar to the flexibility of human thinking, which consists in making a decision and dealing in an appropriate way [Ari 22]. FLC is characterized by flexibility and robustness against complex and nonlinear systems, as it provides satisfactory approximate solutions, by it overcomes of this complexity without resorting to a complex mathematical model and eliminates spurious signals emitted by the system. FLC works with a technique of integrating knowledge that depends on Mamdani model [Azz 17]. FLC is mainly applied range-to-point or range-to-range control, unlike other classic control techniques, it is controlled from point to point, the results obtained from the FLC are derived from the inputs and outputs, which in turn uses membership functions (MFs) each other's associated, by converting crisp inputs into linguistic variables based on their value. As for, the output of the FLC depends on the degree of its membership in the various membership function (MFs), which can be considered as inputs [Bai 06], this robust technology is based on three basic stages, arranged as follows: firstly, fuzzification stage, secondly, the stage of inference rules that based on linguistic variables using the rule (if … then) and logical operations (and, or...), finally defuzzification stage. In this chapter, FLC with SVPWM are applied to improve the control of DFIG rotor.

IV.2 Historical

Fuzzy logic was suggested by Lotfi Zadeh in 1965 [Ngu 19]. Then he developed this idea in 1973, using the linguistic variables that characterize the conditional rule (if...then) [Liu 17], in 1974, Mamdani studied fuzzy logic based on the researchs of Lotfi Zadeh, he performed his first experiment with fuzzy logic control technology on a steam engine [Aou 18]. This success led to interest in developing this technology to expand its uses in many industrial fields.

IV.3 Concept of fuzzy logic

In our daily life, human uses ambiguous logic and ambiguous ideas continuously and routinely, but he does not pay attention to them, as these ambiguous ideas avoid the sudden transition from one category to another, which makes this contrary to the law of the machine "0" or "1", which is

called clear data or classical and can be processed by all devices, unlike the ambiguous ideas or answers, that can only be implemented by humans because they are ideas that are likely to occur between 0 and 1. In order to enable machines to handle vague language input such as 'Somehow Satisfied', the crisp input and output must be converted to linguistic variables with fuzzy components. For instance, to control an air conditioner system, the input temperature and the output control variables must be converted to the associated linguistic variables such as 'HIGH', 'MEDIUM', 'LOW' and 'FAST', 'MEDIUM' or 'SLOW'. The former is corresponding to the input temperature and the latter is associated with the rotation speed of the operating motor. Besides those conversions, both the input and the output must also be converted from crisp data to fuzzy data [Bai 06].

IV.4 Principle of Fuzzy Logic

The classical set has a clear-cut boundary, implying that a member either belongs to the set or does not. Additionally, this classical set can be represented by a binary function with two elements, 0 or 1. For instance, we define the faculty members in the computer science department as set A. The faculty member either fully belongs to this set ($\mu_A(x) = 1$) if they are a faculty in the computer science department, or has no affiliation with set A ($\mu_A(x) = 0$) if they are not part of that department. This mapping is straightforward, employing a sharp boundary without any ambiguity. In other words, "fully belonging to" can be mapped as a member of set A with a degree of 1, while "not belonging to" can be mapped as a member of set A with a degree of 0. This mapping resembles a binary categorization, akin to black-and-white classification. In contrast to a classical set, a fuzzy set allows for members to possess a gradual boundary. In other words, a fuzzy set enables a member to belong to a set to a certain degree. For instance, continuing with the example of temperature, we can divide it into three categories: LOW (0 ~30°F), MEDIUM (30 ~ 70 °F), and HIGH (70 ~ 120 °F) based on the perspective of the classical set, as illustrated in Figure IV.1[Bai 06].

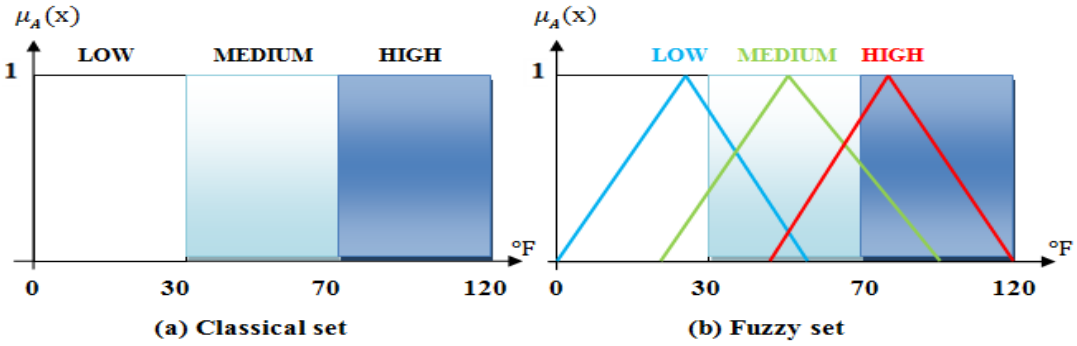

Figure IV.1. Classical and fuzzy sets

In the classical set, each temperature is unambiguously classified into a single subset: either LOW, MEDIUM, or HIGH, with clear boundaries. However, in a fuzzy set, as depicted in Figure IV.1. (b), these boundaries become indistinct or smooth. A temperature can be simultaneously assigned to two or even three subsets. For instance, a temperature of 40 °F may be classified as belonging to low to a certain degree, let's say 0.5, while also being considered part of medium to an extent of approximately 0.7. Another intriguing example is the temperature 50 °F, which can be categorized as belonging to low and high with a degree of around 0.2 and as part of medium with almost 1 degree. The dashed line in Figure 2.3b represents the boundary of the classical set. It is evident that a fuzzy set encompasses elements with varying degrees of membership within the set. This differs from classical or crisp sets, where members can only belong if their membership is complete or full. In a fuzzy set, a member can possess a partial degree of membership, and this partial degree of membership can be mapped to a function or a range of membership values. Let's consider a fuzzy set A, and if an element x is a member of this fuzzy set A, we can represent this mapping as:

$$\mu_A(x) \in [01] \quad (A = (x, \mu_A(x) | \, x \in X) \tag{IV.1}$$

The function $\mu_A(x)$, referred to as the membership function (MF) for the fuzzy set A, is responsible for mapping each element of x to a membership value ranging from 0 to 1. If the membership function $\mu_A(x)$ is limited to either 0 or 1, it is evident that A becomes a classical set, and $\mu_A(x)$ represents the characteristic function of A. The term X commonly denotes the universe of discourse, or simply the universe, which can comprise discrete objects (ordered or unordered) or continuous space [Per 05].

IV.5 Basic Elements of Fuzzy Logic

The basic elements on which the fuzzy logic theory is based are briefly presented as follows:

IV.5.1 Linguistic Variables and Linguistic Terms

In the 1970s, Zadeh introduced and developed the theory of approximate reasoning based on the concepts of linguistic variables and fuzzy logic. A linguistic variable can be informally defined as a variable whose values are words in a natural or artificial language. For instance, "Age" is a linguistic variable with values such as young, old, very young, very old, quite young, more or less young, not very young, and not very old. The values of a linguistic variable are typically derived from primary terms (e.g., young and old) using various linguistic modifiers (e.g., very, more or less) and connectives (e.g., and, or, not). A linguistic term is employed to convey ideas and

information in human communication. A linguistic variable allows for its value to be described both qualitatively through a linguistic term and quantitatively through a corresponding membership function (MF) that expresses the meaning of a fuzzy set. Linguistic terms represent the states of processes and control variables in FLC. Their values are defined using linguistic terms, which can be words or sentences in a natural or artificial language. The FLC is a rule-based system that utilizes principles of fuzzy logic. Among the various techniques developed using fuzzy sets, fuzzy IF-THEN rules emerge as the most prominent and widely employed approach, owing to their extensive and successful applications [Sal 10].

In Zadeh's perspective of fuzzy logic, truth values are expressed linguistically, such as true very true, more or less true, false, possible false, etc. These truth values can be considered as values of the linguistic variable "Truth". The rules of inference in fuzzy logic are approximate rather than exact. As a result, approximate reasoning, also known as fuzzy reasoning, is primarily qualitative rather than quantitative in nature. It falls mostly outside the scope of classical logic's applicability. The main objective of the theory of approximate reasoning is to emulate human linguistic reasoning, particularly in describing the behavior of systems centered around human interactions [Omar 16].

IV.5.2 Membership Functions (MF)

As discussed above, a fuzzy set is completely parameterized by its membership function (MF). Since most fuzzy sets have a universe of discourse X that consists of the real line R, it would be impractical to list all the pairs that define a membership function. Therefore, an MF is expressed using a mathematical formula. An MF can be parameterized according to the desired complexity. These membership functions can also be one-dimensional or multi-dimensional. Here are a few classes of parameterized MFs in one dimension, specifically MFs with a single input [Per 05].

IV.5.2.1 Triangular Membership Function

A triangular MF is specified by three parameters {a, b, c} as follows:

$$triangle(x;a,b,c)=\begin{cases} 0, & x<a. \\ \dfrac{x-a}{b-a}, & a\le x\le b. \\ \dfrac{c-x}{c-b}, & \mathrm{b}\le x\le c. \\ 0, & c<x. \end{cases} \qquad \text{(IV.2)}$$

By using 'min' and 'max,' we have an alternative expression for the preceding equation:

$$triangle(x;a,b,c) = \max\left(\min\left(\frac{x-a}{b-a}, \frac{c-x}{c-b}\right), 0\right) \quad \text{(IV.3)}$$

The parameters {a, b, c} (with a< b< c) determine the x coordinates of the three corners of the underlying triangular MF.

IV.5.2.2 Trapezoidal Membership Function

A trapezoidal MF is specified by four parameters {a, b, c} as follows:

$$trapezoid(x;a,b,c,d) = \begin{cases} 0, & x < a. \\ \frac{x-a}{b-a}, & a \le x \le b. \\ 1, & b \le x \le c. \\ \frac{d-x}{d-c}, & c \le x \le d. \\ 0, & d \le x. \end{cases} \quad \text{(IV.4)}$$

An alternative concise expression using min and max is:

$$trapezoid(x;a,b,c,d) = \max\left(\min\left(\frac{x-a}{b-a}, 1, \frac{d-x}{d-c}\right), 0\right) \quad \text{(IV.5)}$$

The parameter {a, b, c, d} (with a < b < c < d) determine the x coordinates of the four corners of the underlying trapezoidal MF.

IV.5.2.3 Gaussian Membership Function

A Gaussian MF is specified by two parameters {c, σ}:

$$gaussian(x,c,\sigma) = e^{-\frac{1}{2}\left(\frac{x-c}{\sigma}\right)^2} \quad \text{(IV.6)}$$

A Gaussian MF is determined completely by c and σ; c represents the MFs center and σ determines the MFs width.

IV.5.2.4 Generalized Bell Membership Function

A generalized bell MF (or bell MF) is specified by three parameters {a, b, c}:

$$bell(x,a,b,c) = \frac{1}{1+\left|\frac{x-c}{a}\right|^{2b}} \quad \text{(IV.7)}$$

where the parameter b is usually positive. It is also called as the Cauchy MF.

IV.5.2.5 Sigmoidal Membership Function

A sigmoidal MF is defined by:

$$sig(x,a,c) = \frac{1}{1+\exp[-a(x-c)]} \tag{IV.8}$$

where a controls the slope at the crossover point x=c. Sigmoidal functions are widely used as the activation function of artificial neural networks.

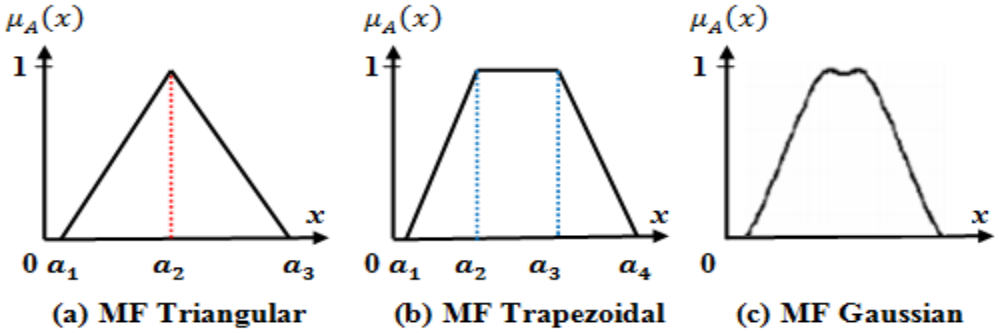

Figure IV.2. Forms for different types of membership functions

IV.5.3 Fuzzy Rules

Human beings make decisions based on rules. Although we may not be aware of it, all the decisions we make are based on computer-like if-then statements. For example, if the weather is fine, we may decide to go out. If the forecast predicts bad weather today but fine weather tomorrow, we decide not to go today and postpone it until tomorrow. Rules connect ideas and establish relationships between events. Fuzzy machines, which aim to imitate human behavior, operate in a similar manner. However, the decision-making process and the means of making those decisions are replaced by fuzzy sets, and the rules are replaced by fuzzy rules. Fuzzy rules also employ a series of if-then statements. For instance, if X, then A; if Y, then B, where A and B represent sets of X and Y. The number of rules is determined by the number of linguistic variables and the number of variables themselves. Fuzzy logic utilizes everyday spoken language to establish a rule base. It commonly employs IF/THEN rules or similar constructs like fuzzy associative matrices. Rules are typically expressed in the form: IF a variable IS a particular set, THEN take a specific action. Fuzzy logic incorporates the AND, OR, and NOT operators from Boolean logic. In fuzzy logic, these operators are often defined as the minimum, maximum, and complement, respectively. They are referred to as the Zadeh operators because they were initially introduced as such in Zadeh's original papers.

IV.6 Fuzzy Sets

IV.6.1 Basic Properties of Fuzzy Sets

Suppose B is a fuzzy set of elements, denoted generically by u, defined on the universe of discourse U, and represented by a membership function μ_B(u), then [Ama 20]:

- **Support of a fuzzy set:**

The support of a fuzzy set B, S(B), is the crisp set of all elements u∈ U such that μ_B(u)> 0, and is written formally as in (IV.9).

$$S(B) = \{u \in U \mid \mu_B(u) > 0\} \tag{IV.9}$$

- **Core of a fuzzy set:**

The core of a fuzzy set B, C(B), is the crisp set of all elements u ∈ U such that μ_B(u)= 1,and is written formally as in (IV.10).

$$C(B) = \{u \in U \mid \mu_B(u) = 0\} \tag{IV.10}$$

- **Height of a fuzzy set:**

The height of a fuzzy set B, H(B), is the largest membership degree corresponding to any element in the set, and is written formally as in (IV.11).

$$H(B) = \sup_{u \in U} \mu_B(u) \tag{IV.11}$$

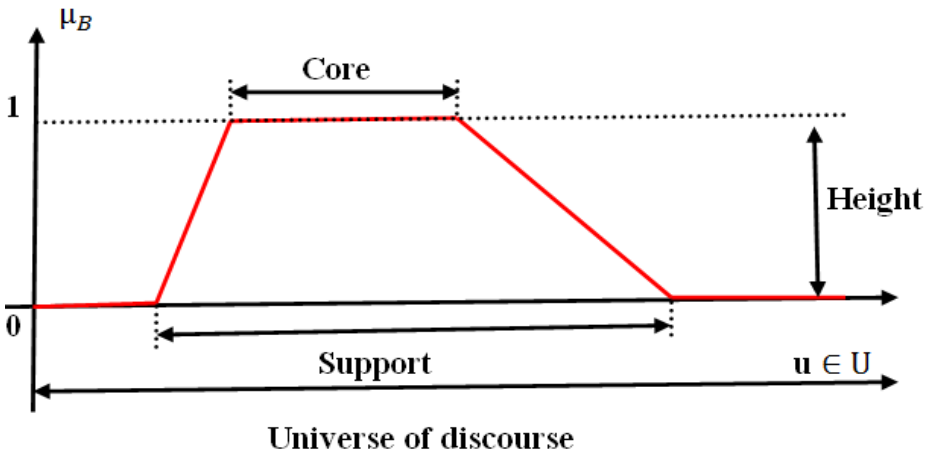

Figure IV.3. Support, Core and height of the fuzzy Sets

IV.6.2 Fuzzy Set Operation

Fuzzy set operation refers to an operation performed on fuzzy sets. These operations serve as generalizations of crisp set operations. Multiple generalizations are possible, but the most commonly utilized ones are known as standard fuzzy set operations. These operations include fuzzy unions, fuzzy intersections, and fuzzy complements [Nit 18].

- **Fuzzy Union (∪):** The union of two fuzzy sets(μ_A(x), μ_B(x)) is the maximum (MAX) of each element from two sets.

$$\mu_{A\cup B}(x) = \mu_A(x) \cup \mu_B(x) = \max(\mu_A(x), \mu_B(x)) \tag{IV.12}$$

- **Fuzzy Intersection (∩):** The intersection of two fuzzy (μ_A(x), μ_B(x)) sets is just the minimum (MIN) of each element from the two sets.

$$\mu_{A\cap B}(x) = \mu_A(x) \cap \mu_B(x) = \min(\mu_A(x), \mu_B(x)) \tag{IV.13}$$

- **Fuzzy Complement (A^c):** The complement of a fuzzy variable with degree of membership (DOM) x is (1-x).

$$\mu_{\bar{A}}(x) = 1 - \mu_A(x) \tag{IV.14}$$

- **Some other Additional Operations:**

Equality: A = B, if μ_A(x) = μ_B(x), ∀x ∈ X

Not equal: A ≠B, if μ_A(x) ≠ μ_B(x) for at least one x ∈ X

Containment: A⊆ B if and only if μ_A(x) ≤ μ_B(x), ∀x∈ X

Product: A.B is defined as $\mu_{A.B}$(x) = μ_A(x)· μ_B(x)

IV.7 General Structure of Fuzzy Logic Controller

We focus in our research on the fuzzy mamdani's inference system and how to use it. A Mamdani model of the fuzzy logic controller contains four basic stages, which are listed as [Per 05].

- Fuzzification stage;
- Knowledge base stage;
- Inference engine stage (fuzzy reasoning, decision-making logic);
- Defuzzification stage.

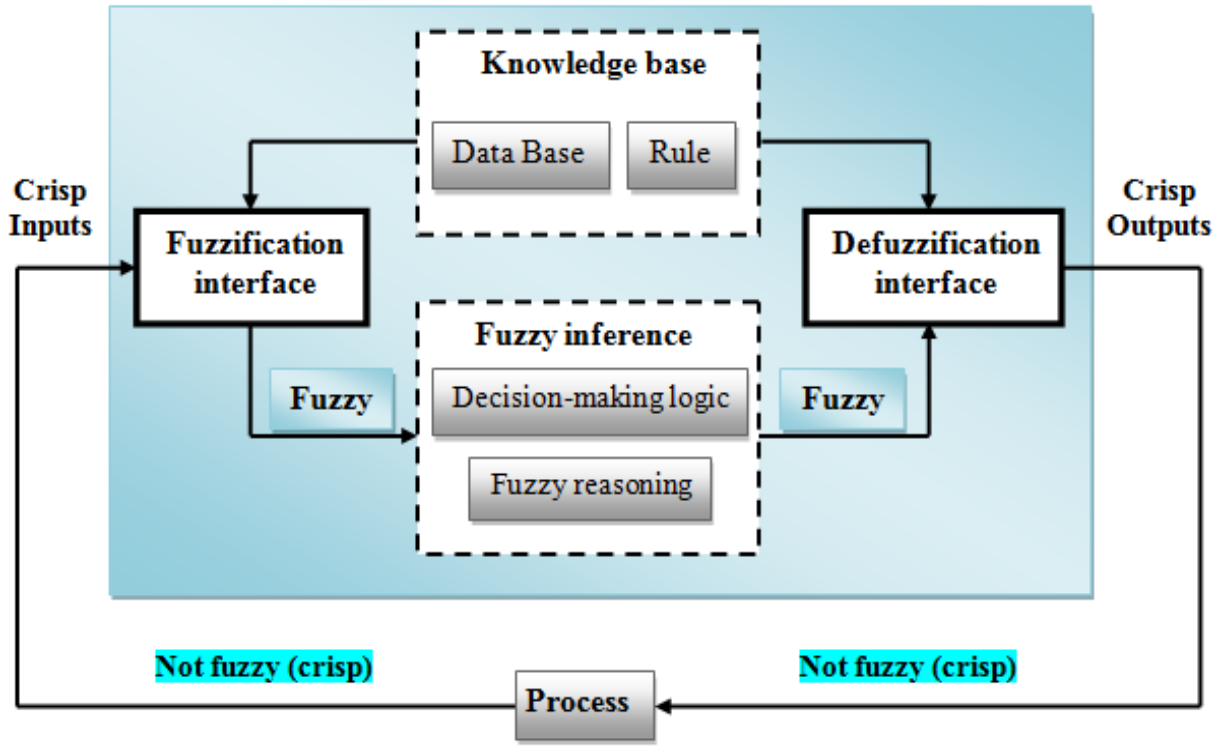

Figure IV.4. General structure of FLC stages

IV.7.1 Fuzzification stage

The first important step that contributes to the design of the fuzzy logic controller is to define the state variables. These variables are passed through the fuzzification block to fuzzify the input. The fuzzy logic control only works with fuzzy inputs, so the numeric inputs of the crisp linguistic variables must be converted into fuzzy linguistic variables. This transformation is called the process of fuzzification. The generally used crisp linguistic variables consist of case error, or change of state error (derivative of state error), or the area of a state error (integral of state error). The fuzzification process is performed using membership functions, which are the graphical representation of the degree of belonging of an element to the fuzzy set. The value of the degree of belonging quantum ranges between 0 and 1. We can use different membership functions for input and output depending on the precision requirement.

IV.7.2 Knowledge base stage:

The knowledge base consists of the database and the linguistic control rule base. The database provides the information used to define the linguistic control rules and the fuzzy data manipulation in the fuzzy logic controller. The rule base, which contains expert rules, specifies the control goal actions through a set of linguistic rules. In other words, the rule base contains rules that would be provided by an expert. The FLC examines the input signals and, using the expert rules, determines

the appropriate output signals (control actions). Fuzzy logic utilizes everyday spoken language to define the rule base. Fuzzy logic typically employs IF/THEN rules or equivalent constructs such as fuzzy associative matrices. Rules are usually expressed in the form: IF a variable is set, THEN take action. The AND, OR, and NOT operators from Boolean logic also exist in fuzzy logic, typically defined as the minimum, maximum, and complement operators. When defined in this manner, they are referred to as the Zadeh operators, named after Zadeh's original papers where they were first defined. The main methods for developing the rule base include:

- Utilizing the experience and knowledge of an expert for the application and control goals.
- Modeling the control action of the operator.
- Modeling the process.
- Employing a self-organized fuzzy controller.
- Correcting significant errors in the process output through suitable adjustments of the control output.
- Ensuring smooth control action near the reference value.
- Preventing the process output from exceeding user-specified values.

IV.7.3 The inference engine stage:

The inference engine, also known as the reasoning mechanism, is the core of the fuzzy logic controller. It possesses the capability to simulate human decision-making based on fuzzy concepts and infer fuzzy control actions using fuzzy implications and fuzzy logic rules of inference. In other words, once all the monitored input variables are transformed into their respective linguistic variables through the fuzzification process, the inference engine evaluates the set of if-then rules provided in the rule base. As a result, a linguistic value for the linguistic variable is obtained. The fuzzy linguistic result then needs to be transformed into a crisp output value for the FLC, which is why a defuzzification process is employed.

IV.7.3.1 Inference Rules

The rules of inference can be described in several methods which are as follows:

- **Linguistically:**

We write the rules explicitly, as in the following example:

1. **IF** (error of rotor current is Negative-Big) **OR** (error change of rotor current is Negative-Big) **Then** (change of reference rotor voltage is Negative-Very Big)

2. **IF** (error of rotor current is Negative-Big) **OR** (error change of rotor current is Negative-Medium) **Then** (change of reference rotor voltage is Negative-Very Big)

3. **IF** (error of rotor current is Negative-Big) **OR** (error change of rotor current is Negative-Small) **Then** (change of reference rotor voltage is Negative-Very Big)

4. **IF** (error of rotor current is Negative-Big) **OR** (error change of rotor current is Zero) **Then** (change of reference rotor voltage is Negative-Big)

……..

49. **IF** (error of rotor current is Positive-Big) **OR** (error change of rotor current is Positive-Big) **Then** (change of reference rotor voltage is Positive-Very Big)

- **Symbolically**

It is in fact a linguistic description where the designation of fuzzy sets is replaced by abbreviations.

1. **IF** (e_{Irdq} is **NB**) **OR** (Δe_{Irdq} is **NB**) **Then** (ΔV^{*}_{rdq} is **NVB**)
2. **IF** (e_{Irdq} is **NB**) **OR** (Δe_{Irdq} is **NM**) **Then** (ΔV^{*}_{rdq} is **NVB**)
3. **IF** (e_{Irdq} is **NB**) **OR** (Δe_{Irdq} is **NS**) **Then** (ΔV^{*}_{rdq} is **NVB**)
4. **IF** (e_{Irdq} is **NB**) **OR** (Δe_{Irdq} is **ZE**) **Then** (ΔV^{*}_{rdq} is **NB**)

……..

49. **IF** (e_{Irdq} is **PB**) **OR** (Δe_{Irdq} is **PB**) **Then** (ΔV^{*}_{rdq} is **PVB**)

- **By inference matrix:**

It gathers all the inference rules in the form of a table. In the case of a two dimensional array, the entries of the array represent the fuzzy sets of the input variables (rotor current error: e_{Irdq} and rotor current error change: Δe_{Irdq}). The intersection of a column and a row gives the fuzzy set of the output variable (reference rotor voltage change: ΔV^{*}_{rdq}) defined by the rule.

Table IV. 1. Fuzzy logic system inference matrix

ΔV^{*}_{rdq}		e_{Irdq}						
		NB	NM	NS	ZE	PS	PM	PB
Δe_{Irdq}	NB	NVB	NVB	NVB	NB	NM	NS	ZE
	NM	NVB	NVB	NB	NM	NS	ZE	PS
	NS	NVB	NB	NM	NS	ZE	PS	PM
	ZE	NB	NM	NS	ZE	PS	PM	PB
	PS	NM	NS	ZE	PS	PM	PB	PVB
	PM	NS	ZE	PS	PM	PB	PVB	PVB
	PB	ZE	PS	PM	PB	PVB	PVB	PVB

IV.7.3.2 Inference Mechanism

There are several methods used to enable the inference mechanism and they are listed as:

- **The MAX-MIN inference method**

The max-min (or Mamdani) inference appears when choosing the Minimum as logical AND, the Maximum as logical OR, Truncate as the reshaping method and Maximum as the aggregation method [Izq 15].

- **The Max-Product inference method**

The max-prod inference uses the Product function as its reshaping method, so the original consequents of each of the rules are scaled down, rather than truncated. This leads to a different aggregated fuzzy set with a different Centre of gravity [Izq 15].

- **The Sum-Product inference method**

In this method, the operator "AND" is represented by the function "Prod", the operator "OR" is represented by the function "Sum" and the conclusion "Then" is represented by the "Prod" function.

IV.7.4 Defuzzification stage

The final stage of the fuzzy logic process is defuzzification, during which the aggregated fuzzy set produces a single scalar value as output. As the name suggests, defuzzification is the inverse operation of fuzzification. While in the initial step, the crisp values of input variables are transformed into degrees of membership with respect to fuzzy sets, the final step extracts a precise value from the range of the fuzzy set for the output variable. Numerous defuzzification methods have been proposed in the literature [Wan 15].

- **Centroid Method**

The Centroid Method, also known as the center of area or center of gravity, is widely used and considered the most physically intuitive among all defuzzification methods (Sugeno, 1985; Lee, 1990). In this thesis, the Centroid Method is the only method adopted. It is determined using the following algebraic expression

$$z_{COA} = \frac{\int_z \mu_A(z).z\,dz}{\int_z \mu_A(z)} \qquad \text{(IV.15)}$$

where z is the output variable, and $\mu_A(z)$ is the membership function of the aggregated fuzzy set A with respect to z.

- **Center of Sums Method**

The Center of Sums method is considered the fastest defuzzification method. It involves calculating the algebraic sum of the individual output fuzzy sets. However, one drawback of this method is that intersecting areas are added twice, which can lead to potential inaccuracies. The algebraic equation for obtaining the defuzzified value using the Center of Sums method is given by the following equation:

$$U_f = \frac{\sum_{j=1}^{p} A(\alpha_j).f_j}{\sum_{j=1}^{p} A(\alpha_j)} \quad \text{(IV.16)}$$

In the Center of Sums method, the weights used are the areas of the respective membership functions. On the other hand, in a weighted average method, the weights are the individual membership values themselves.

- **Mean-Max Method (Middle of Maxima MOM Method)**

From the distribution of the membership function of the combined control action, the range of the output variable is determined. This range corresponds to the point where the membership function reaches its maximum value. The mid-value of this range is considered as the crisp output of the controller [Pra 07]. In this defuzzification technique, the average output value is obtained by using the following method:

$$z = \frac{z_1 + z_2}{2} \quad \text{(IV.17)}$$

where, z_1 is the first value and z_2 is the last value, the output overall membership function $\mu_A(z)$ is maximum.

IV.8 Advantages

Fuzzy logic has many advantages and can be used in many areas due to its efficiency and benefits mentioned as follows:

- The structure of fuzzy systems is straightforward and easy to understand, and they do not require a mathematical model [Mas 20].
- FLC is very easy to comprehend because the concept behind the control is straightforward [Kri 15].

- Fuzzy systems are well-suited for uncertain or approximate reasoning, particularly in cases where deriving a mathematical model is challenging [Mas 20].
- FLC can be confidently employed, particularly when dealing with inaccurate input data [Mas 20].
- FLC can effectively operate even in the presence of noisy inputs [Kri 15].
- Fuzzy systems can be designed with ease, as they do not require complex mathematical analysis [Kri 15].
- FLC enables decision-making based on estimated values in situations with incomplete or uncertain information [Mas 20].
- FLC can handle multiple inputs and generate multiple outputs, as it operates solely based on rules. Creating the rule base for fuzzy control is easier compared to optimizing the parameters for PID control [Kri 15].
- FLC performs exceptionally well in highly non-linear systems, adapting to the specific situation. On the other hand, designing conventional controllers to adjust to non-linear characteristics can be extremely challenging [Kri 15].

IV.9 Drawbacks

While FLC offers numerous advantages, it also has some relevant disadvantages, which can be summarized as follows:

- One of the notable disadvantages of FLC is the extensive manual tuning required in industrial applications. This manual tuning process can be time-consuming, especially when applied to similar factories or in the experimental field [Alb 00].
- Another disadvantage of FLC is that the process of calculating parameters is not based on a mathematical rule. This can make the parameter calculation tedious, time-consuming, and potentially inaccurate.
- Many actual implementations of FLC are only equivalent to interpolation schemes in lookup tables [Alb 00].
- Fuzzy systems do not possess the same capacity for machine learning and pattern recognition as neural networks.
- The validation and verification of a fuzzy knowledge-based system often require extensive testing with hardware.
- If the model is unknown, it can be challenging to achieve stability in the controller system.
- In some cases, the rules in a fuzzy logic system may be mismatched or non-coherent.

IV.10 Application of Fuzzy Logic to DFIG

In this chapter, the FLC is applied to control the inverter connected to the rotor of DFIG. The block scheme of IDPC using FLC to control the DFIG rotor is shown in Figure IV.5.

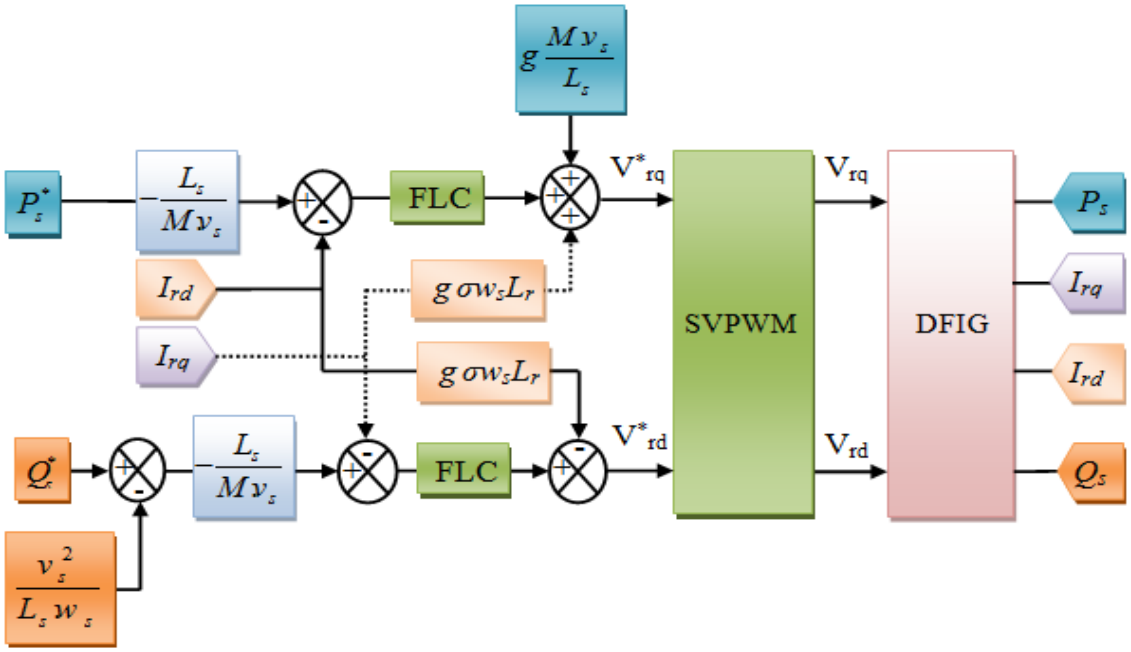

Figure IV.5. IDPC using FLC to control the DFIG rotor

The general model of FLC used to control the DFIG rotor in this chapter is shown in Figure IV.6. This model proposes inputs (e_{Irdq}, Δe_{Irdq}) and output (ΔV^{*}_{rdq}) of FLC, 1/z is represented the time delay [Haz 17].

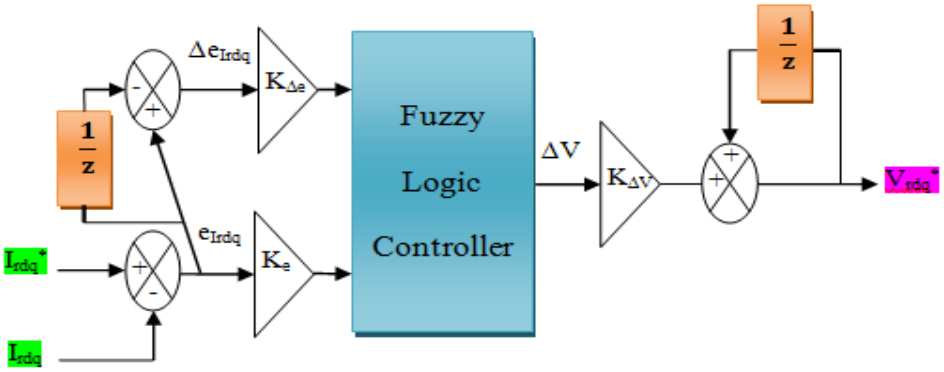

Figure IV.6. General model of FLC

Each element of the fuzzy set has a degree of membership (degree of belong) that distinguishes it in the membership function, where a degree of belong of the elements for each membership function ranges is between 0 and 1, as for the range of membership functions for each of the error,

error change and voltage change ranges are between -1 and 1, as illustrated in Figures IV.7, 8, and 9.

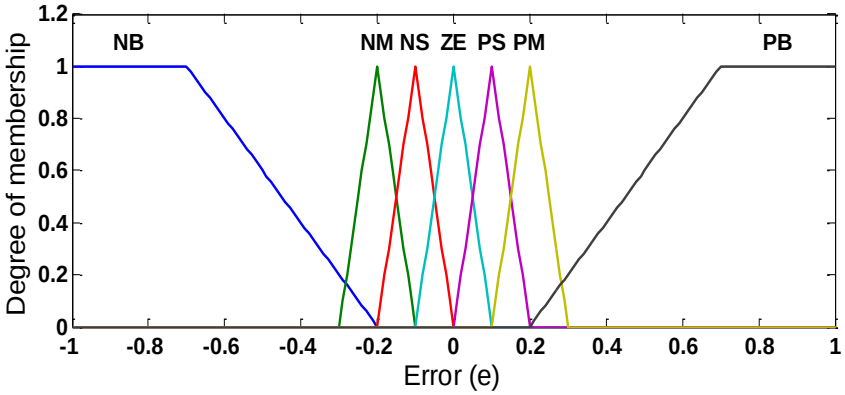

Figure IV.7. MFs of e_{Irdq}

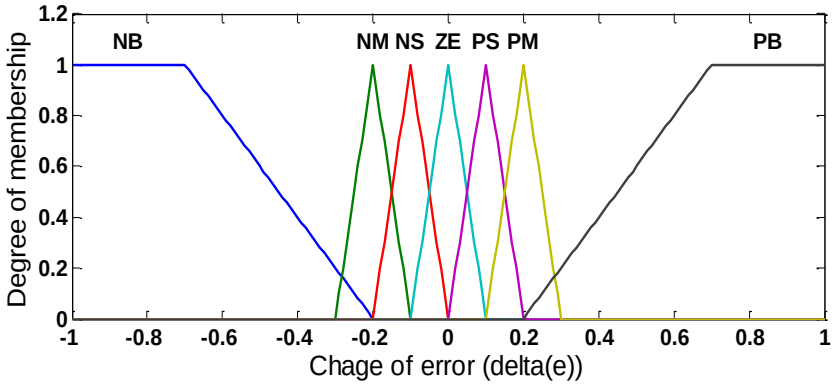

Figure IV.8. MFs of Δe_{Irdq}

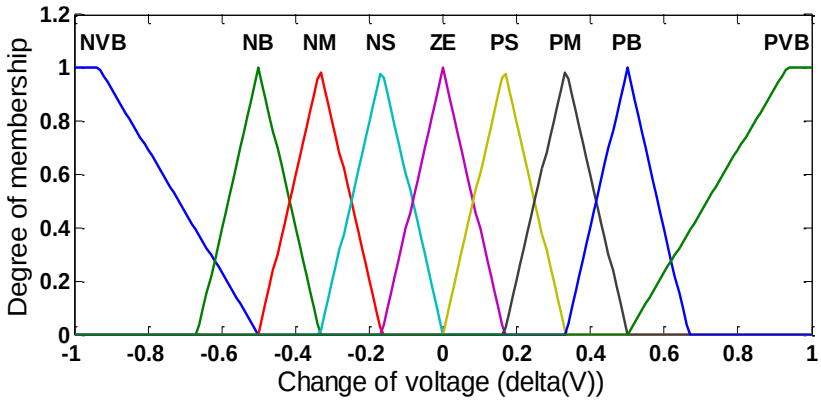

Figure IV.9. MFs of ΔV^{*}_{rdq}

The names of MFs shown in Figures IV.7, 8, and 9 are illustrated as:

PVB: represents **P**ositive-**V**ery **B**ig.

PB: represents **P**ositive-**B**ig.

PM: represents **P**ositive-**M**edium.

PS: represents **P**ositive-**S**mall.

ZE: represents **Z**ero.

NS: represents **N**egative-**S**mall.

NM: represents **N**egative-**M**edium.

NB: represents **N**egative-**B**ig.

NVB: represents **N**egative-**V**ery **B**ig.

The inference rules mentioned earlier are summarized in the inference matrix of this system, which are previously included in Table IV. 1.

By applying the inference matrix and the conditional rule (if...then), we can get the rule surface as shown in Figure IV.10.

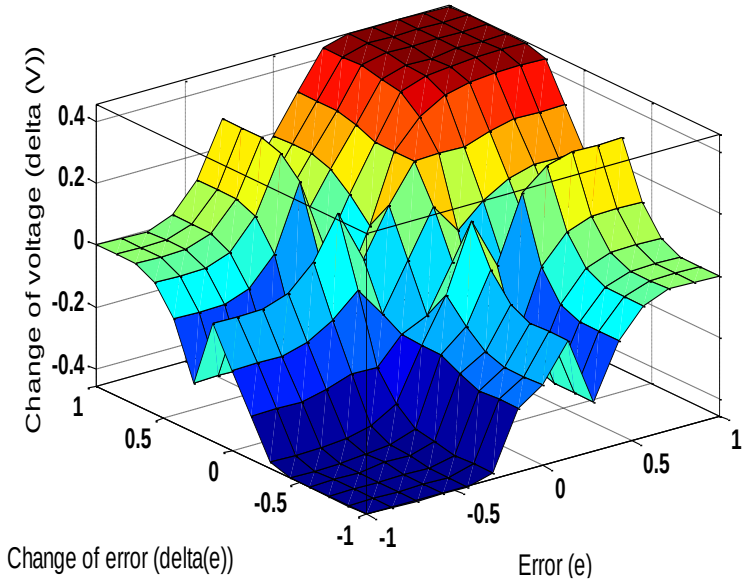

Figure IV.10. Rule surface using Mamdani model

IV.11 Fuzzy Backstepping Control applied to DFIG

BSC is a stable and highly effective control method that has led to great success in the field of control. However, conventional BSC suffers from complexity at every step due to the increasing order of nonlinear systems. Therefore, to achieve adaptive control with the system order, its gain values need to be varied repeatedly. To eliminate the complexity arising from the system order and external disturbances and increase the stability of nonlinear systems, the constant gain is replaced by a FLC in the virtual control law of the Lyapunov function. This hybrid technique of BSC and FLC is known as fuzzy backstepping control (FBSC) [Lui 17].

To track the reference signal and ensure system stability, we multiply the inputs (e_{Irdq}, Δe_{Irdq}) and output (ΔV^{*}_{rdq}) with appropriate gains (k_e, $k_{\Delta e}$) and (k_p, k_i), respectively. The block scheme of FLC using PI controller is shown in Figure IV.11.

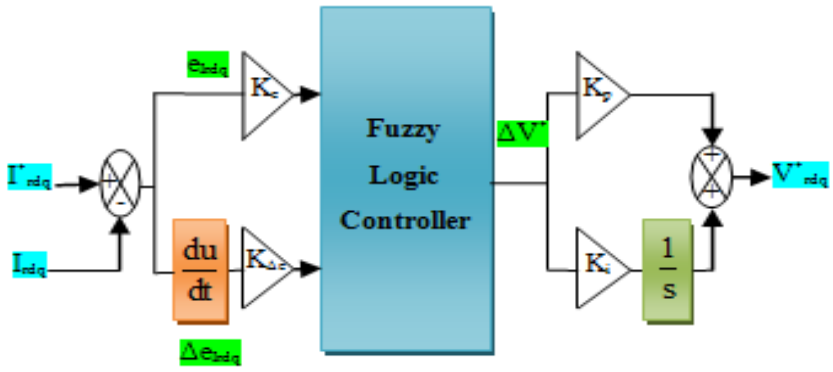

Figure IV.11. Overall model of FLC using PI controller

From (III.15), the reference rotor currents are as follows:

$$\begin{cases} I_{rd}^{ref} = -\dfrac{L_s}{MV_s}.P_s^{ref} \\ I_{rq}^{ref} = -\dfrac{L_s}{MV_s}.(Q_s^{ref} - \dfrac{V_s^2}{L_s w_s}) \end{cases} \quad \text{(IV.18)}$$

Using (III.24), and replacing positive gains (k_1, k_2) with FLC, the reference rotor voltages for FBSC can be written as follows:

$$\begin{cases} v_{rd}^{ref} = L_r\sigma(\dot{I}_{rd}^{ref} + (FLC)_2.e_4) + R_r I_{rd} - gw_s\sigma L_r I_{rq} \\ v_{rq}^{ref} = L_r\sigma(\dot{I}_{rq}^{ref} + (FLC)_1.e_2) + R_r I_{rq} + gw_s\sigma L_r I_{rd} + g\dfrac{L_m v_s}{L_s} \end{cases} \quad \text{(IV.19)}$$

IDPC using FBSC for controlling DFIG rotor is shown in Figure IV.12.

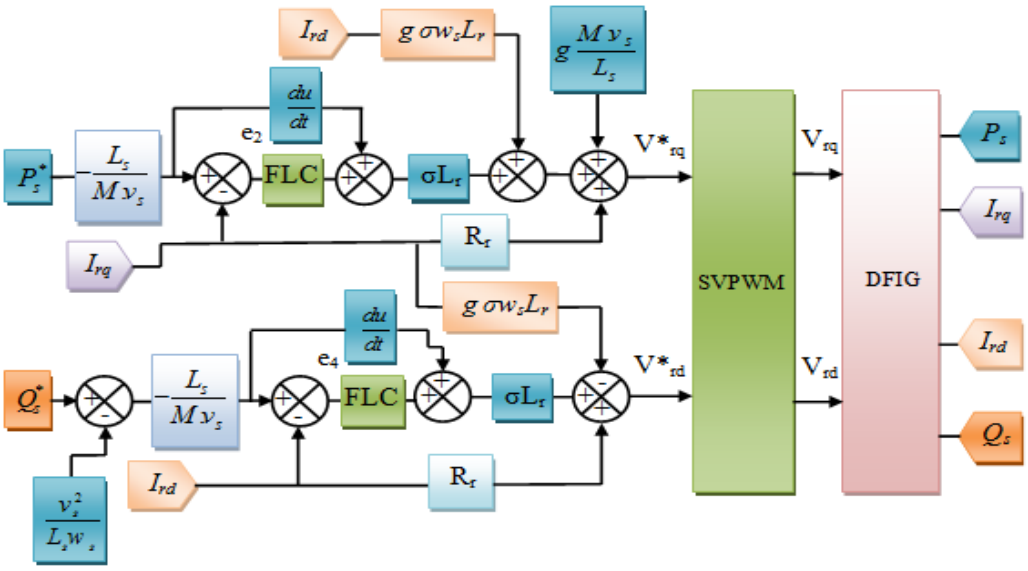

Figure IV.12. IDPC using FBSC for controlling DFIG rotor

IV.11 Simulation Results

Fig. IV.13(a) shows the wind speed applied to the turbine, the value of which varies randomly from 5.9 to 9.26 m/s, over 10 s. Fig. IV.13(b) shows the rotor speed generated by the wind turbine being applied to the DFIG, the value of which varies from 0 to 148.83 rad/s.

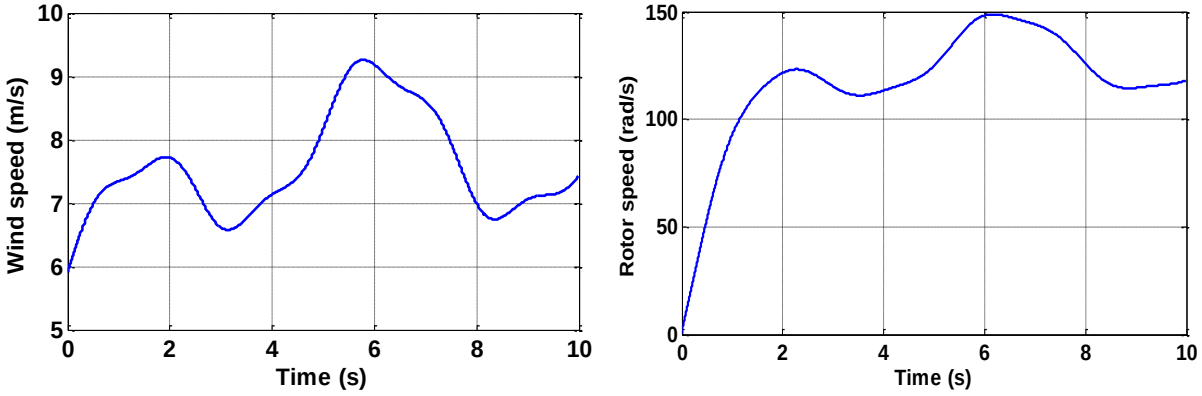

(a) (b)

Figure IV.13. (a) Wind speed and (b) Rotor speed

Figs. IV.14(a) and IV.14(b) show the stator active power and its reference profile, the value of which varies from 0 to −6.2599 kW, integrated with FLC using PWM and SVPWM, respectively. The reference of stator power (P_s^*) is generated by the mechanical speed of the rotor (ω_m) multiplied by the reference of electromagnetic torque (T^*_{em}) resulting from MPPT, to obtain maximum power at all power points. Figs. IV.15(a) and IV.15(b) illustrate the stator reactive power (blue line) and its reference profile integrated with FLC using PWM and SVPWM, respectively. The reference value of stator reactive power is always maintained at zero (Q_{sref} = 0), to ensure a unit power factor (PF = 1).

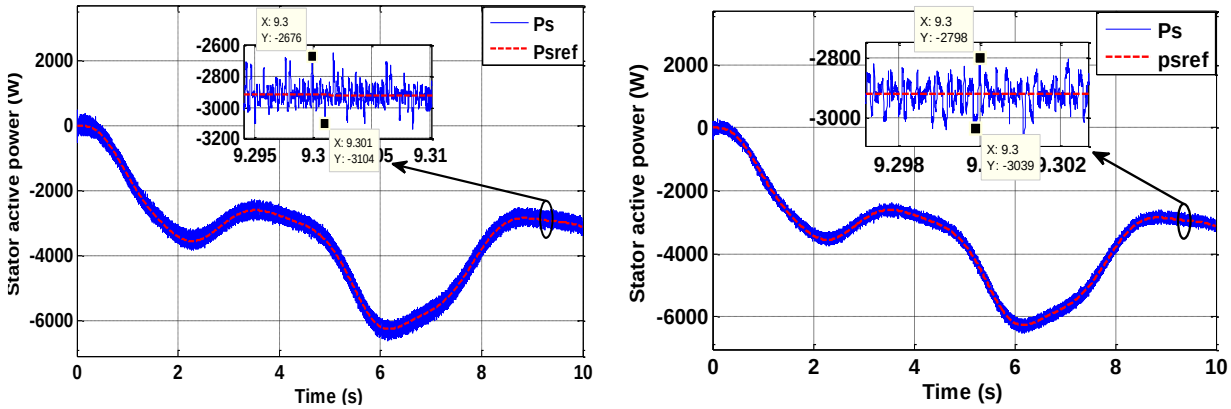

(a) (b)

Figure IV.14. Stator active power using (a) PWM and (b) SVPWM

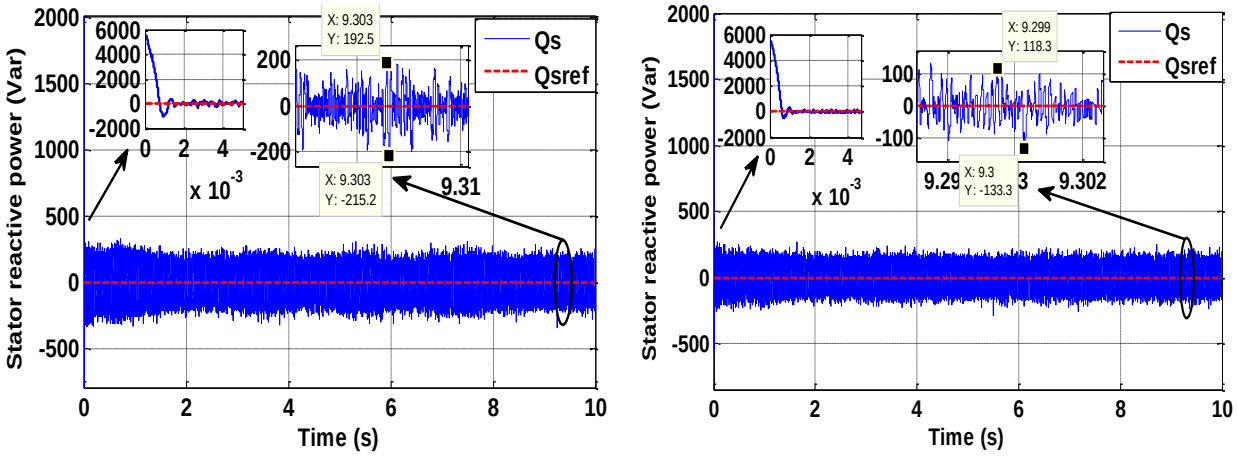

(a) (b)

Figure IV.15. Stator reactive power using (a) PWM and (b) SVPWM

The simulation results revealed that SVPWM gives reduced ripples of active power (-3039 W $\leq \Delta P_s \leq -2798$ W) and reactive power (-133.3 Var $\leq \Delta Q_s \leq 118.3$ Var), compared to PWM which gives higher ripples of active power (-3104 W $\leq \Delta P_s \leq -2676$ W) and reactive power (-215.2 Var $\leq \Delta Q_s \leq 192.5$ Var).

Figs. IV.16(a) and IV.16(b) illustrate the three-phase stator currents using PWM and SVPWM, respectively. The frequency of the stator current is always constant ($f_s = 50$ Hz) to synchronize it with the electrical grid. Figs. IV.17(a) and IV.17(b) show a zoom of the three-phase stator currents ranging between 4.6 s and 4.625 s using PWM and SVPWM, respectively. The simulation results reveal that the three-phase stator current using SVPWM has significantly lower ripples compared to PWM.

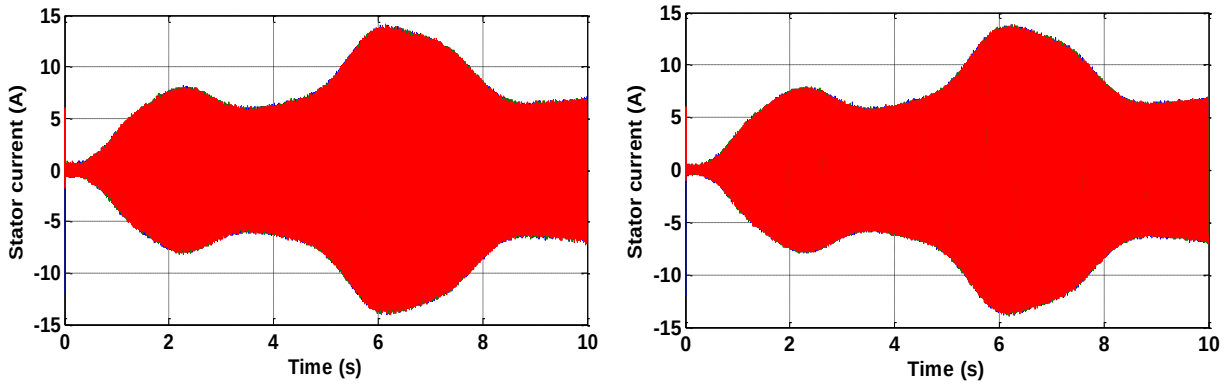

(a) (b)

Figure IV.16. Stator currents using (a) PWM and (b) SVPWM

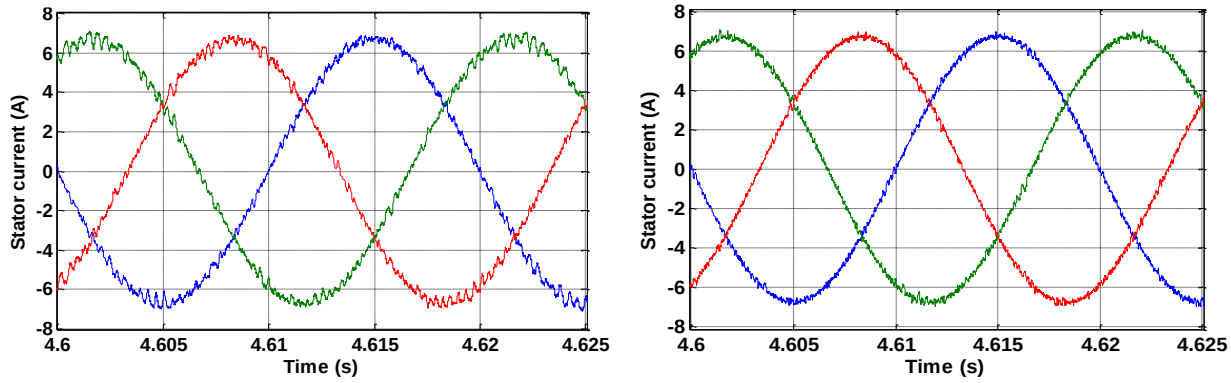

(a) (b)

Figure IV.17. Zoom of the stator currents using (a) PWM and (b) SVPWM

Figs. IV.18(a) and IV.18(b) illustrate the three-phase rotor currents using PWM and SVPWM, respectively. The frequency of the rotor currents relates to the rotor speed (ω_s). Figs. IV.19(a) and IV.19(b) show a zoom of the three-phase rotor currents ranging between 2.8 s and 2.9 s using PWM and SVPWM, respectively. The simulation results reveal that the three-phase rotor current using SVPWM has lower ripples compared to PWM.

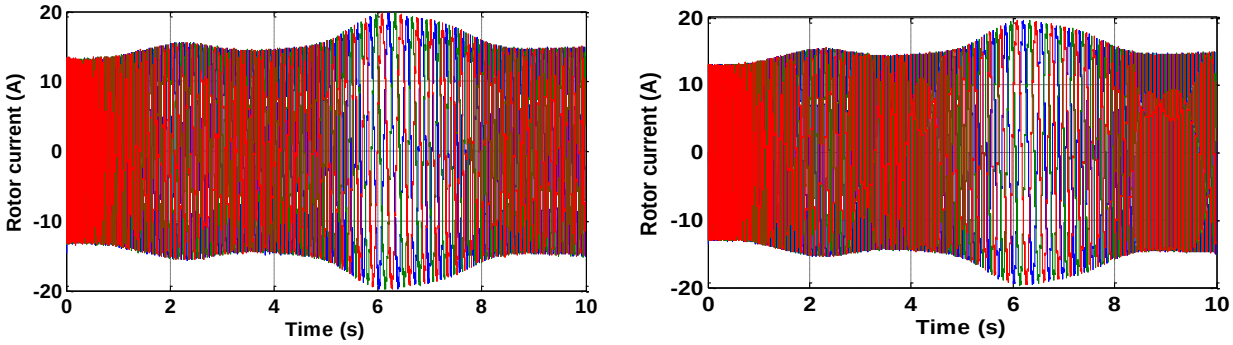

(a) (b)

Figure IV.18. Rotor currents using (a) PWM and (b) SVPWM

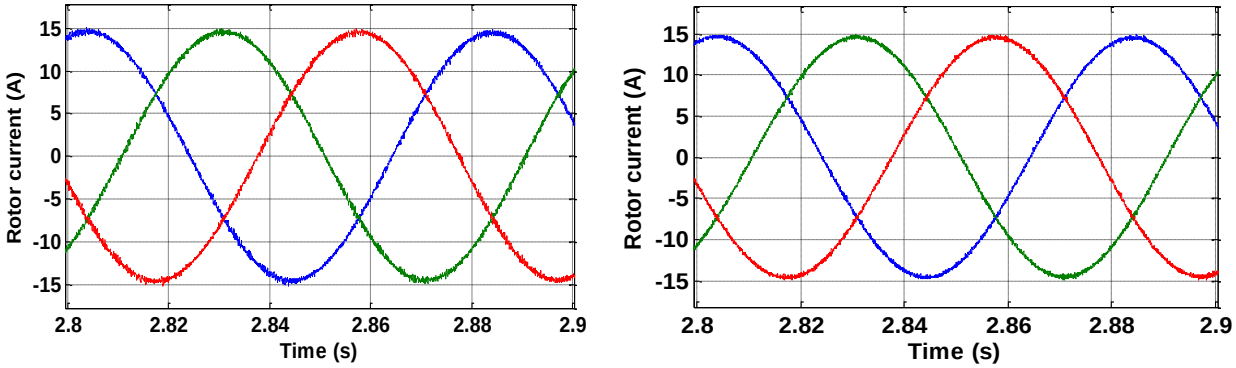

(a) (b)

Figure IV.19. Zoom of the rotor currents using (a) PWM and (b) SVPWM

Figs. IV.20(a) and IV.20(b) show the reference rotor voltage and carrier signal using PWM and SVPWM, respectively.

The simulation results reveal that the amplitude of the carrier signal is greater than or equal to the amplitude of reference signal in the permanent regime, and this should be taken into consideration to respect the control signals.

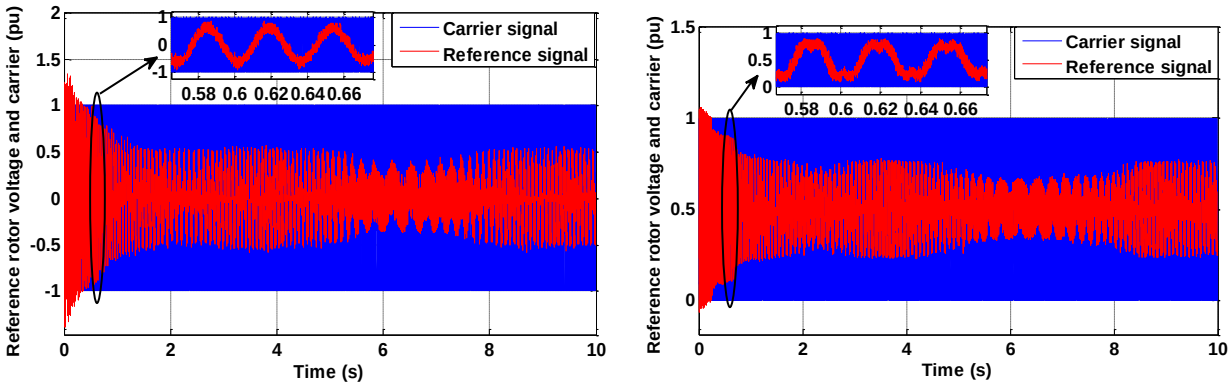

(a) (b)

Figure IV.20. Reference rotor voltage and carrier signal using (a) PWM and (b) SVPWM

Figs. IV.21(a) and IV.21(b) present the harmonic spectrum of one phase of the stator current using PWM and SVPWM, respectively, obtained using Fast Fourier Transform (FFT). Subsequently, SVPWM had a lower THD (1.94%) compared to PWM (THD = 3.92%).

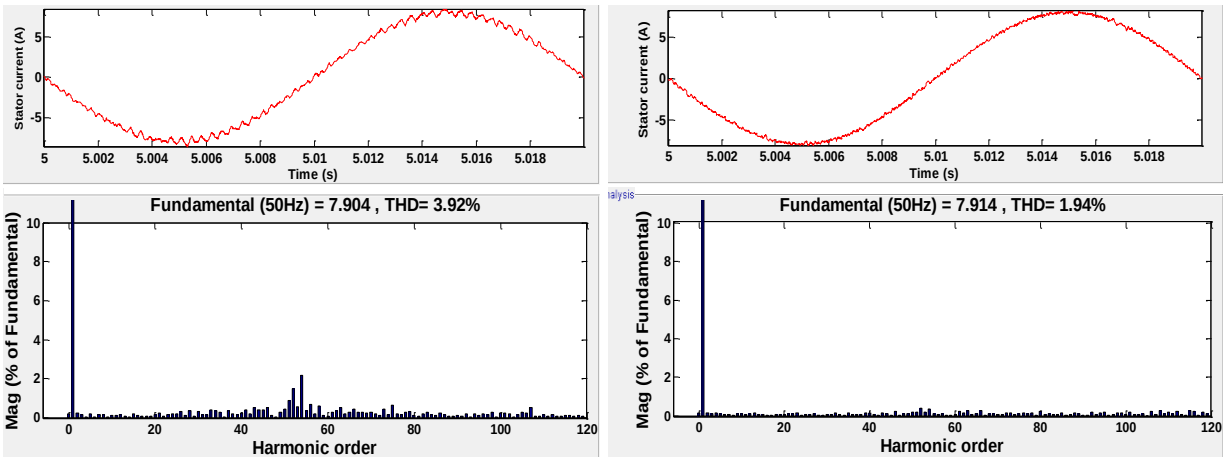

(a) (b)

Figure IV.21. Harmonic spectrum of stator current using (a) PWM and (b) SVPWM

In summary, it is clear that both techniques using FLC show good tracking and greater stability in transient and non-linear systems. Furthermore, SVPWM provides better performance due to the lower ripples of active and reactive powers and reduced THD of the stator current compared to PWM. Table IV. 2 summarizes the performance comparison between FLC-PWM and SVPWM.

Table IV. 2. Comparison of performance between PWM and SVPWM

Technique / Performance	FLC-PWM	FLC-SVPWM
Ripples of P_s (W)	428	241
Ripples of Q_s (Var)	407.7	251.6
THD (%)	3.92	1.94

The difficulties encountered in obtaining the simulation results relate to the selection of the gains from the FLC. This is because the FLC is not subject to an arithmetic rule, and unlike the classical controller, the gains (K_e, $K_{\Delta e}$) are selected by taking into account the error (e_{Irda}) and error change (Δe_{Irdq}) ripples that are confined to the range [−1, 1]. Moreover, the gain ($K_{\Delta V}$) is selected by taking into account the reference signal value (V_{rdq}^{*}), the amplitude of which is less than or equal to the amplitude of the carrier signal.

A comparison of the THD value between the FLC-SVPWM proposed in this paper and other control techniques suggested in several previous articles is presented in Table IV. 3.

Table IV. 3. Comparison study of THD value between Proposed method and other techniques

Reference	Control technique	THD (%)
[Bek 13]	SMC-PWM	6.62
	SMC-SVM	2.54
[Boudj 13]	SMC-MC	3.05
	FSMC-MC	2.85
[Amr 16]	FOC	3.7
[Ben 20-2]	DPC-PI-SVPWM	2.59
Proposed method	FLC-SVPWM	1.94

where SMC-PWM is the sliding mode control using a pulse width modulation inverter, SMC-SVM is the sliding mode control using a space vector modulation inverter, SMC-MC is the sliding mode control using a matrix converter, FSMC-MC is the fuzzy mode control using a matrix

converter, FOC is the field-oriented control, DPC-PI-SVPWM is the direct power control with a proportional integrator controller using a space vector pulse width modulation inverter.

By comparing the results in Table IV. 3, we found that the proposed method in this paper (FLC-SVPWM) provides better performance (lower THD (%)) compared to other control methods suggested in several previous articles.

IV.12 Conclusion

In this chapter, a theoretical study is presented on FLC to enhance the control of DFIG rotor, it is a flexible and robust control technique based on the integration of expert knowledge based on the Mamdani model. Then, a comparative study was conducted between pulse width modulation (PWM) and space vector pulse width modulation (SVPWM) based on FLC to control the rotor of DFIG driven by a variable speed wind turbine. After analyzing the results obtained using MATLAB/Simulink, it can be concluded that FLC using SVPWM inverter provides better performance than PWM inverter, such as lower ripples of stator active and reactive powers, and lower THD of the stator current.

Chapter V

Voltage Dips of DFIG with Dynamic Voltage Restorer

V.1 Introduction

DFIG-wind turbines are very sensitive to grid disturbances, such as voltage dips, therefore, a sudden drop in some or all phases of the grid voltage causes an overcurrent and overvoltage at the level of the rotor windings, which may lead to damage to the control devices installed at the level of the rotor and the separation of the wind turbine from the grid. For example, 2,800 MW of wind-origin power in Spain was disconnected on November 4, 2006 due to a European outage [Lop 08]. According to IEEE Std.1159-2009 [Qua 95], a voltage dip is a drop of the RMS voltage magnitude between 10% and 90% of the nominal value lasting from half a cycle (at the supply frequency) to 1 min. After some time, the voltage recovers and goes back to its initial value. In general, there are two types of voltage dips, symmetrical voltage dips and asymmetrical voltage dips [Dum 19]. Symmetrical voltage dips result from the symmetric drop in the three-phases of voltage, and its effect on sensitive loads is less harmful than asymmetrical voltage dips, as for the asymmetrical voltage dips are caused by a sudden asymmetric drop in one, two or more phases. The latter is very harmful to sensitive loads, especially the doubly fed induction generator, which leads to damage to the electronic circuits of the rotor control converters due to the rotor overcurrents and the rotor overvoltages, thus, this results in the separation of the DFIG-wind turbine from the grid. One must be careful that the reference voltage used to define the voltage sag is the RMS voltage as advised in [Dum 19] [Bol 00]. The difference between the words "voltage sag" and "voltage dip" is the following as explained in [Dumont 19] [Sinh 10]:

• A voltage sag refers to the remaining voltage, e.g. a voltage sag of 60% means that 60% of the RMS voltage remains.

• A voltage dip refers to the amount by which the voltage has dropped, e.g. a voltage dip of 60% means that 40% of the RMS voltage remains.

To solve this problem, a dynamic voltage restorer must be used to compensate for the lost voltage. A dynamic voltage restorer (DVR) is a power-electronic converter-based device that has been designed to protect critical loads from all supply-side disturbances other than outages. It is connected in series with a distribution feeder and is capable of generating or absorbing real and reactive power at its ac terminals. The basic principle of a DVR is simple: by inserting a voltage of required magnitude and frequency, the DVR can restore the load-side voltage to the desired amplitude and waveform even when the source voltage is unbalanced or distorted. Usually a DVR is connected to protect sensitive loads during faults in the supply system [Gho 02]. Dynamic Voltage Restorer (DVR) can provide the most cost effective solution to mitigate voltage dips by establishing the proper voltage quality level that is required by customer. When a fault happens in

a distribution network, sudden voltage sag will appear on adjacent loads. DVR installed on a sensitive load, restores the line voltage to its nominal value within the response time of a few milliseconds thus avoiding any power disruption to the load [Jur 04]. The major functions of the DVR controller are, detection of voltage disturbances events in the system, calculation of the compensating voltage and generation the reference signal for the PWM to trigger the voltage source inverter. Hence, the Dynamic Voltage Restorer is considered as a power efficient device compared to other custom power devices. The first DVR in the world was installed in the USA in the year 1996, it was engineered by Electrical Power Research Institute, this DVR was installed at the medium voltage level of 12kV and rated for 2MVA [Shu 21]. DVR is connected between the supply (grid) and the sensitive load (stator) so that it can inject a voltage of required waveform. Hence it can protect sensitive consumer loads from supply disturbances. In a capacitor supported DVR, the power absorbed/supplied is almost zero except small losses in the steady state and the voltage injected by the DVR should be in quadrature with the feeder current [Sing 11-2]. In this chapter, a comprehensive theoretical study is given for the symmetrical and asymmetrical voltage dips of the grid and their impact on the DFIG. These results are verified by using Matlab/Simulink.

V.2 Model of DFIG

DFIG is more commonly used in wind power generation compared to other types of generators. It employs a back-to-back converter system (Rotor-Side Converter, DC Link, Grid-Side Converter) at the rotor level, enabling it to operate within a variable speed range of approximately ±30% around its nominal synchronous speed. This flexibility allows for efficient power generation with varying turbine speeds. The excess power generated, estimated at around 30% of the nominal power, is referred to as the slip speed ratio, contributing to the economical nature of this generator [Azz 17] [Nia 11]. The DFIG's stator is directly connected to the electrical grid, which makes it highly susceptible to grid disturbances such as symmetrical and asymmetrical voltage dips. To mitigate the effects of these disturbances, DVR technology is proposed, a diagram of DFIG driven by a wind turbine with a back-to-back converter and DVR is presented in Figure V.1.

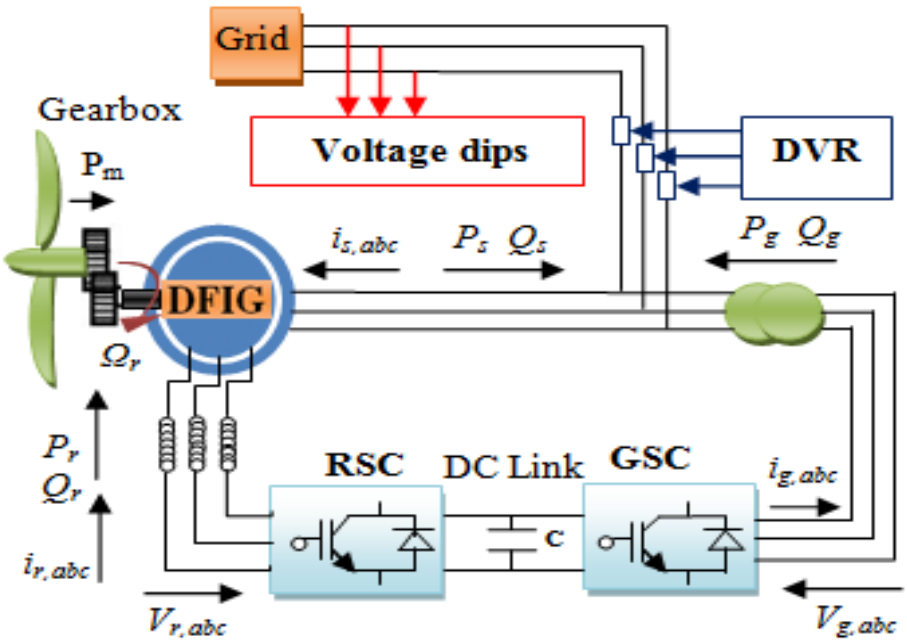

Figure V.1 Diagram of DFIG-wind turbine under voltage dips with DVR

Using the Clarke transformation, expressions for the stator and rotor voltage and flux can be obtained in the complex form as follows [Lop 08]:

$$\overrightarrow{V_s} = \vec{V}_{s\alpha} + j\vec{V}_{s\beta} = R_s \overrightarrow{I_s} + \frac{d\overrightarrow{\phi_s}}{dt} \tag{V.1}$$

$$\overrightarrow{\phi_s} = \overrightarrow{\phi_{s\alpha}} + j\overrightarrow{\phi_{s\beta}} = L_s \overrightarrow{I_s} + M\overrightarrow{i_r} \tag{V.2}$$

$$\overrightarrow{V_r} = \vec{V}_{r\alpha} + j\vec{V}_{r\beta} = R_r \overrightarrow{I_r} + \frac{d\overrightarrow{\phi_r}}{dt} - j\omega.\overrightarrow{\phi_r} \tag{V.3}$$

$$\overrightarrow{\phi_r} = \overrightarrow{\phi_{r\alpha}} + j\overrightarrow{\phi_{r\beta}} = L_r \overrightarrow{I_r} + M\overrightarrow{I_s} \tag{V.4}$$

The rotor flux can be determined using the rotor current, stator flux, and leakage coefficient, as shown below:

$$\overrightarrow{\phi_r} = \frac{M}{L_s}\overrightarrow{\phi_s} + \sigma L_r \overrightarrow{I_r} \tag{V.5}$$

By substituting (V.5) into (V.3), the rotor voltage equation can be expressed as follows:

$$\overrightarrow{V_r}(t) = \left(\frac{M}{L_s}\left(-j\omega + \frac{d}{dt}\right)\right).\overrightarrow{\phi_s}(t) + \left(R_r + \sigma L_r\left(-j\omega + \frac{d}{dt}\right)\right).\overrightarrow{I_r}(t) \tag{V.6}$$

There are two parts in (V.6), the first part is related to the stator flux vector and the second part relates to the rotor current. When the rotor currents are equal to zero (I_r=0), then (V.6) becomes as:

$$\overrightarrow{V_{rop}}(t) = \frac{M}{L_s}\left(-j\,\omega + \frac{d}{dt}\right)\overrightarrow{\phi_s}(t) \tag{V.7}$$

The second part of (V.6) only appears when the rotor current is present. This current is produced when a voltage dip occurs in both R_r and σL_r.

V.3 DFIG Operation with Grid Voltage

The operation of DFIG is affected by changes in the grid voltage state, which is studied as follows [Lop 08]:

V.3.1 Normal State without Voltage Dips

The stator voltage vector is characterized by synchronous angular speed (ω_s) and maintains a constant amplitude (V_{s0}) during normal operation, which is expressed as follows:

$$\overrightarrow{V_s}(t) = \vec{V}_{s0}\,e^{jw_s t} \tag{V.8}$$

The stator flux can be expressed using (V.1) and (V.8), assuming the stator resistance (R_s) is negligible, as follows:

$$\overrightarrow{\phi_s}(t) = \frac{\vec{V}_{s0}}{jw_s}e^{jw_s t} = \overrightarrow{\phi_{s0}}e^{jw_s t} \tag{V.9}$$

During a normal state, the stator flux is a vector of constant amplitude that is directly proportional to the network voltage. The flux vector can rotate synchronously with the network and indicates the system forced response. Thus, we can express it as the stator forced flux "φ_{sf}".

By substituting (V.9) in (V.7), the part of the rotor voltage produced by the stator flux can be written as:

$$\overrightarrow{V_{rop}}(t) = \frac{M}{L_s}\vec{V}_{s0}\left(1-\frac{w}{w_s}\right)e^{jw_s t} = \frac{M}{L_s}\vec{V}_{s0}\,s\,e^{jw_s t} \tag{V.10}$$

where, s is the slip frequency.

The rotor voltage induced by the stator flux is directly proportional to the slip frequency, this implies that the amplitude of the rotor voltage (V_{rop}) can be expressed as a function of the stator voltage amplitude as follows:

$$\vec{V}_{rop}(0) = \vec{V}_{s0} \cdot \frac{M}{L_s} \frac{w_r}{w_s} = \vec{V}_{s0} \cdot \frac{M}{L_s} . s \tag{V.11}$$

The equations mentioned earlier illustrate the rotor voltage in the absence of rotor current. Therefore, in the normal case, the rotor side converter regulates the rotor current for tracking the reference of active and reactive powers. Additionally, the expression of the rotor voltage is given as follows:

$$\overrightarrow{V_r}(t) = \frac{M}{L_s} . s . \overrightarrow{V_s}(t) + \left(R_r + \sigma L_r \left(-j\omega + \frac{d}{dt} \right) \right) . \overrightarrow{I_r}(t) \tag{V.12}$$

V.3.2 DFIG Under Symmetrical Voltage Dips

When a symmetrical stator voltage dip occurs, the nominal voltage amplitude V_1 is reduced to the faulty voltage amplitude V_2, as illustrated below [Lop 08]:

$$\overrightarrow{V_s} = \begin{cases} V_1 . e^{jw_s t}, \; for \; t < t_0 \\ V_2 . e^{jw_s t}, \; for \; t \geq t_0 \end{cases} \tag{V.13}$$

where, $V_2 = (1\text{-}d).V_1$, d is the profundity that occurs in the grid voltage.

Using (V.9) and (V.13), the stator flux expression is given as:

$$\overrightarrow{\phi_{sf}} = \begin{cases} \dfrac{V}{j\omega_s} . e^{jw_s t}, \; for \; t < t_0 \\ \dfrac{(1-d).V}{j\omega_s} . e^{jw_s t}, \; for \; t \geq t_0 \end{cases} \tag{V.14}$$

where t_0: moment of voltage dip, that occurred in the grid.

V.3.2.1 In Case of Open-Circuit of Rotor

The changes in the stator flux can be determined by solving the differential equation (V.15) which is derived from (V.1) and (V.2), while also considering that i_r equals zero due to its negligible influence on the rotor voltage, the stator flux equation in this case can be written as follows [Wes 10]:

$$\frac{d\overrightarrow{\phi_s}}{dt} = \overrightarrow{V_s} - \frac{R_s}{L_s} . \overrightarrow{\phi_s} \tag{V.15}$$

The solution of the differential equation (V.15) during symmetrical voltage dips in the grid, at $t \geq t_0$, can be divided into two parts: the homogeneous and the non-homogeneous solution. The

homogeneous solution represents the natural response of (V.15), and is also referred to as the "natural flux". It can be expressed as follows [Lop 08]:

$$\overrightarrow{\phi_{sn}} = \overrightarrow{\phi_{n0}} e^{-t.\frac{R_s}{L_s}} = \overrightarrow{\phi_{n0}} e^{-t/\tau_s} \tag{V.16}$$

where, ϕ_{n0} represents the initial value of the natural flux, which satisfies the initial condition ($t=t_0$), and τ_s represents the time constant of the stator.

The natural flux consists of both permanent and transient flux components, and ensures that there are no interruptions in the magnetic state of the machine when its operating point changes.

Considering at $t=t_0$, that the stator flux is identical immediately before and after the fault, therefore the expression is written as follows:

$$\overrightarrow{\phi_s}\left(t_0^-\right) = \overrightarrow{\phi_s}\left(t_0^+\right) \tag{V.17}$$

Thus, the equation for the decomposition of the flux at the beginning of the dip can be written as follows:

$$\overrightarrow{\phi_{sf}}\left(t_0^-\right) = \overrightarrow{\phi_{sf}}\left(t_0^+\right) + \overrightarrow{\phi_{sn}}\left(t_0^+\right) \tag{V.18}$$

The flux decomposition before and at the beginning of the voltage dip is illustrated in Figure V.2

Figure V.2 Diagram of flux decomposition before and at beginning of the voltage dip

The flux decomposition during the voltage dip is illustrated in Figure V.3.

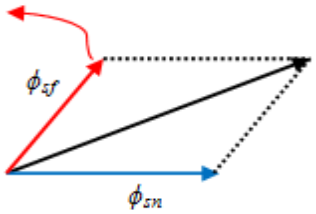

Figure V.3 Diagram of flux decomposition during the voltage dip

Using (V.14), (V.15), and (V.18), and the condition ($t \geq t_0$), the stator flux during grid voltage dips becomes as follows:

$$\overrightarrow{\phi_s} = \frac{(1-d)V}{j\omega_s} e^{jw_s t} + \frac{d.V}{j\omega_s} e^{(-t/\tau_s)} \tag{V.19}$$

Eq. (V.19) consists of two parts. The first part is a rotational term related to the grid voltage, while the second part is the normal flux, which consists of a term with a constant angle related to the time constant (τ_s). Before the grid voltage dip appears, the forced flux causes the constant flux area vector to follow the trajectory of a circle with a radius of one. However, when the natural flux occurs, it shifts the circuit away from the same radius and centers it at a fixed radius less than one during the symmetrical voltage dip. Both components of the total flux result in two components of the open-circuit rotor voltage, which can be written as follows:

$$\overrightarrow{V_{rop}} = \overrightarrow{V_{rf}} + \overrightarrow{V_{rn}} \tag{V.20}$$

V_{rf} is called the rotor voltage produced by the forced flux.
V_{rn} is called the rotor voltage produced by the natural flux.

Using (V.14), and (V.7), the rotor voltage produced by the forced flux becomes given as:

$$\overrightarrow{V_{rf}} = (1-\mathrm{d}).V.\frac{M}{L_s}.s.e^{-jw_s t} \tag{V.21}$$

By substituting the second part of (V.19) in (V.7), the rotor voltage produced by the natural flux is given as follows:

$$\overrightarrow{V_{rn}} = -\frac{M}{L_s}.\left(\frac{1}{\tau_s}+\mathrm{jw}\right).\frac{\mathrm{d.V}}{\mathrm{jw_s}}.e^{-t/\tau_s} \tag{V.22}$$

when $1/\tau_s$ is neglected, the voltage equation can be written on the new formula:

$$\overrightarrow{V_{rn}} = -\frac{M}{L_s}.\frac{\omega}{\omega_s}.\mathrm{d.V}.e^{-t/\tau_s} \tag{V.23}$$

The total equation of the open-circuit rotor voltage in the rotor reference frame is obtained by the detailed and approximate formula as follows:

$$\overrightarrow{V_{rop}} = V.\frac{M}{L_s}\left((1-d).s.e^{jw_r t} - d.(1-s).e^{-jwt}.e^{-t/\tau_s}\right) \tag{V.24}$$

The two terms in the preceding equation are dissimilar in nature. The first term originates from the new grid voltage and has a relatively small amplitude, as it is proportionate to the slip. Its frequency is the difference between the synchronous speed and the rotor speed. The second term, on the other hand, is a transient voltage caused by the natural flux. Its amplitude can be significant

since it is proportional to the depth of the dip. Additionally, its frequency is the rotor's electrical speed **(**ω**)**.

V.3.2.2 In Case of Rotor Connected to Converter

In this case, the rotor currents are non-zero, and therefore they affect the rotor voltage according to (V.6) and (V.7), which can be written as follows:

$$\overrightarrow{V_r}(t) = \overrightarrow{V_{rop}}(t) + \left(R_r + \sigma L_r \left(\frac{d}{dt} - j\,\omega \right) \right) \overrightarrow{I_r}(t) \tag{V.25}$$

The rotor voltage equation in a rotating reference frame can be written as follows:

$$\overrightarrow{V_r}(t) = \overrightarrow{V_{rop0}} e^{-jwt} + R_r . \overrightarrow{i_r^r}(t) + \sigma L_r . \frac{d\,\overrightarrow{i_r^r}(t)}{dt} \tag{V.26}$$

Eq. (V.26) can be used to determine the maximum depth of voltage dips that the inverter can withstand. When a significant voltage dip occurs in the grid, the voltage of the rotor generated by the stator flux may exceed the maximum voltage that the inverter can withstand, resulting in a loss of control over the rotor current. As a result, the deeper the voltage dip in the grid, the greater the increase in the rotor currents. However, if the depth of the voltage dip is small enough so that the voltage generated by the stator flux does not exceed the maximum voltage that the inverter can withstand, then the rotor currents can be easily controlled.

V.3.3 DFIG with Asymmetrical Voltage Dips

The study of asymmetrical dips in phase voltages can be facilitated by utilizing symmetrical components theory, which states that a three-phase voltage system can be represented as the combination of three sequences: positive, zero, and negative sequences. Consequently, three separate vectors may be formed from the stator voltage space vector, each corresponding to one of these components.

$$\vec{V_s}(t) = \vec{V_p} e^{jw_s t} + \vec{V_n} e^{-jw_s t} + \vec{V_z} \tag{V.27}$$

For example, when a classical machine has symmetrical impedances, the positive sequence voltage (V_p) generates a magnetic flux that rotates at the synchronous speed, while the negative sequence voltage (V_n) produces a magnetic flux that rotates in the opposite direction. In contrast,

the zero sequence voltage (V_z) does not produce any rotating magnetic flux, as it creates a magnetic field that remains stationary in the machine stator.

The forced flux can be expressed in the steady state, by two terms that correspond to the positive component and negative component of the stator voltage, denoted as ϕ_{sp} and ϕ_{sn}, respectively. Neglecting the stator resistance, these fluxes can be mathematically represented as:

$$\begin{cases} \overrightarrow{\phi_{sp}}(t) = \dfrac{\vec{V}_p}{jw_s}.e^{jw_s t} \\ \overrightarrow{\phi_{sn}}(t) = \dfrac{\vec{V}_n}{-jw_s}.e^{-jw_s t} \end{cases} \tag{V.28}$$

Each flux creates a voltage in the rotor based on its amplitude and relative speed to the rotor windings. The sum of the three terms yields the overall open-circuit rotor voltage:

$$\vec{V}_{rop}(t) = \vec{V}_{rp}(t) + \vec{V}_{rn}(t) + \vec{V}_{rnat}(t) \tag{V.29}$$

By substituting (V.28) in (V.7), the induced voltages resulting from the forced fluxes can be obtained. These voltages can be expressed in the reference frame of the rotor as follows:

$$\begin{cases} \vec{V}_{rp}(t) = \dfrac{M}{L_s}.s.\vec{V}_p.e^{jsw_s.t} \\ \vec{V}_{rn}(t) = \dfrac{M}{L_s}.(s-2).\vec{V}_n.e^{-j(2-s)w_s.t} \end{cases} \tag{V.30}$$

The first voltage in (V.30) is directly proportional to the slip, resulting in a relatively small magnitude. Additionally, the frequency of this voltage is equivalent to the slip frequency, typically ranging within the low frequency range of a few hertz. On the other hand, the second voltage in (V.30) has a factor near to 2, thus its amplitude can be significant if the asymmetrical ratio of the dip is large. Because the slip is generally minimal, its frequency is approximately double that of the grid, given that the slip is typically small. The voltage caused by the natural flux is dependent on its initial value:

$$\overrightarrow{V_{rnat}} = -\frac{M}{L_s}\left(jw + \frac{1}{\tau_s}\right).\overrightarrow{\phi_{nat\,0}}.e^{-jwt}e^{-t/\tau_s} \tag{V.31}$$

If we ignore the term $1/\tau_s$, the previous formula simplifies to:

$$\overrightarrow{V_{rnat}} = -jw \cdot \frac{M}{L_s} \cdot \overrightarrow{\phi_{nat\,0}} e^{-jwt} e^{-t/\tau_s} \tag{V.32}$$

V.3.3.1 Single Phase Voltage Dip

When a short circuit occurs in one-phase, such as phase a, the voltage at that phase will decrease. We assume that the impedance of the negative and positive sequence networks are equal, so the voltages of phase b and phase c will remain unchanged. The stator voltages of the three phases can be expressed as follows:

$$\begin{cases} \overrightarrow{V_{sa}} = (1-d)\overrightarrow{V_{s0}} e^{jw_s t} \\ \overrightarrow{V_{sb}} = \overrightarrow{V_{s0}} \bar{a}^2 e^{jw_s t} \\ \overrightarrow{V_{sc}} = \overrightarrow{V_{s0}} \bar{a} e^{jw_s t} \end{cases} \tag{V.33}$$

where, $\bar{a} = 1 \angle 120^\circ = e^{j\frac{2\pi}{3}}$, d is the dip depth in the grid voltage.

The components of negative sequence, positive sequence, and zero sequence are obtained as:

$$\begin{bmatrix} \overrightarrow{V_p} \\ \overrightarrow{V_n} \\ \overrightarrow{V_z} \end{bmatrix} = \frac{1}{3} \begin{bmatrix} 1 & \bar{a} & \bar{a}^2 \\ 1 & \bar{a}^2 & \bar{a} \\ 1 & 1 & 1 \end{bmatrix} \begin{bmatrix} \overrightarrow{V_{s0}}.(1-d) \\ \overrightarrow{V_{s0}}.\bar{a}^2 \\ \overrightarrow{V_{s0}}.\bar{a} \end{bmatrix} = \overrightarrow{V_{s0}}. \begin{bmatrix} 1-d/3 \\ -d/3 \\ -d/3 \end{bmatrix} \tag{V.34}$$

Using (20), it is feasible to compute the negative and positive fluxes through (V.28) and subsequently determine the voltages induced in the rotor through (V.30). By taking into account the continuity of the total flux, we can find the natural flux using the initial conditions.

$$\begin{cases} \overrightarrow{\phi_s}\left(t_0^-\right) = \overrightarrow{\phi_s}\left(t_0^+\right) \\ \overrightarrow{\phi_{sf}}\left(t_0^-\right) = \overrightarrow{\phi_{sfp}}\left(t_0^+\right) + \overrightarrow{\phi_{sfn}}\left(t_0^+\right) + \overrightarrow{\phi_{snat}}\left(t_0^+\right) \end{cases} \tag{V.35}$$

where, ϕ_{sfp} is the forced flux generated by the voltage positive component after the dip, ϕ_{sfn} is the forced flux generated by the voltage negative component after the dip.

In contrast to the state of a symmetrical dips, the magnitude of the natural flux in an asymmetrical dips situation is dependent on the time of the dip. If the dip starts at $t_0 = 0$, the natural flux becomes zero. This happens because, at that specific moment, the negative and positive fluxes align, causing their combined sum to be equal to the flux before the dip state. Consequently, the absence of a

natural flux results in the absence of transitory behavior, thereby maintaining the stator flux in a steady state.

The worst case for a single phase dip arises when the dip takes place at $t_0 = T/4$, where T represents the grid period. In this particular case, the normal flux initial value is at its maximum due to the conflict of negative and positive fluxes whose sum is at a minimum. The natural flux initial value can be obtained using (V.35) as follows:

$$\overrightarrow{\phi_{snat}} = \overrightarrow{\phi_{nat\,0}}.e^{-\frac{t}{\tau_s}} = \frac{2.\overrightarrow{V_{s\,0}}.d}{3.w_s}.e^{-\frac{t}{\tau_s}} \tag{V.36}$$

V.3.3.2 Tow-Phase Voltage Dips

There are two types of voltage dips in the three phases: phase-to-phase and tow-phase to ground.

- ***In case Phase to Phase Voltage Dips***

In order to investigate the phase to phase dips, a short circuit between phase b and phase c is now explored. The short circuit between them causes a dip in their voltages. we assume that the impedance of the negative and positive sequence networks are equal, so the voltage of phase a will remain unchanged. In light of these dips, the voltages of the three phases can be expressed as follows:

$$\begin{cases} \overrightarrow{V_{sa}} = \overrightarrow{V_{s\,0}}.\mathrm{e}^{jw_s t} \\ \overrightarrow{V_{sb}} = \overrightarrow{V_{s\,0}}.(\bar{a}^2 + j\,\frac{\sqrt{3}}{2}.d).\mathrm{e}^{jw_s t} \\ \overrightarrow{V_{sc}} = \overrightarrow{V_{s\,0}}.(\bar{a} - j\,\frac{\sqrt{3}}{2}.d).\mathrm{e}^{jw_s t} \end{cases} \tag{V.37}$$

From (V.37), the composite stator voltage (V_{bc}) can be expressed as follows:

$$\overrightarrow{V_{bc}} = \overrightarrow{V_{sb}} - \overrightarrow{V_{sc}} = \sqrt{3}.\overrightarrow{V_{s\,0}}.(1-d).\bar{a}^2.e^{j\left(w_s t + \frac{\pi}{6}\right)} \tag{V.38}$$

As stated in (V.37), the greater the dip depth, the closer the voltages of phase b and phase c will approach each other until they become identical in the full maximum dip case (d = 1).

The three components of the stator voltage can be written as below:

$$\begin{bmatrix} \overrightarrow{V_p} \\ \overrightarrow{V_n} \\ \overrightarrow{V_z} \end{bmatrix} = \overrightarrow{V_{s\,0}}.\begin{bmatrix} 1-d/2 \\ d/2 \\ d/2 \end{bmatrix} \tag{V.39}$$

Using the voltages given in (V.37), the various components of the rotor voltages and stator fluxes can be determined by utilizing (V.30) and (V.28), respectively.

In case phase to phase dips, the maximum natural flux is attained when the dips happen at $t_0 = 0$. Its initial value can be, computed using (V.39), is as follows:

$$\overrightarrow{\phi_{snat}}(0^+) = \overrightarrow{\phi_{nat\,0}} = \frac{\overrightarrow{V_{s0}}}{j.w_s}.d \tag{V.40}$$

- ***In case Tow Phase to Ground***

In this case, a short circuit has occurred between two phases (b, c) and ground. This short circuit of these two phases has resulted in voltage dips, as shown in (V.41).

$$\begin{cases} \overrightarrow{V_{sa}} = \overrightarrow{V_{s0}}.e^{jw_s t} \\ \overrightarrow{V_{sb}} = (1-d_b).\overrightarrow{V_{s0}}.\bar{a}^2.e^{jw_s t} \\ \overrightarrow{V_{sc}} = (1-d_c).\overrightarrow{V_{s0}}.\bar{a}.e^{jw_s t} \end{cases} \tag{V.41}$$

Therefore, the three components of the stator voltage can be written as below:

$$\begin{bmatrix} \overrightarrow{V_p} \\ \overrightarrow{V_n} \\ \overrightarrow{V_z} \end{bmatrix} = \frac{1}{3}\begin{bmatrix} 1 & \bar{a} & \bar{a}^2 \\ 1 & \bar{a}^2 & \bar{a} \\ 1 & 1 & 1 \end{bmatrix}\begin{bmatrix} \overrightarrow{V_{s0}} \\ (1-d_b).\bar{a}^2.\overrightarrow{V_{s0}} \\ (1-d_c).\bar{a}.\overrightarrow{V_{s0}} \end{bmatrix} \tag{V.42}$$

After performing the calculations, we obtain the following:

$$\begin{cases} \overrightarrow{V_p} = \overrightarrow{V_{s0}}.\left(1 - \dfrac{(d_b + d_c)}{3}\right) \\ \overrightarrow{V_n} = \overrightarrow{V_{s0}}.\left(\dfrac{(d_b + d_c)}{6} - j\,\dfrac{\sqrt{3}.(d_b - d_c)}{6}\right) \\ \overrightarrow{V_z} = \overrightarrow{V_{s0}}.\left(\dfrac{(d_b + d_c)}{6} + j\,\dfrac{\sqrt{3}.(d_b - d_c)}{6}\right) \end{cases} \tag{V.43}$$

V.3.3.3 Three-Phase Voltage Dips

There are two types of voltage dips in the three phases: phase-to-phase-to-phase, and three-phase to ground.

- ***In case Phase-to-Phase-to-Phase Voltage Dips***

In this case, a short circuit occurs between the three phases (a, b, c), and this short circuit causes voltage dips, which are expressed as follows:

$$\begin{cases} \overrightarrow{V_{sa}} = \overrightarrow{V_{s0}} \cdot \left(1 - \frac{3}{2} d\right) e^{jw_s t} \\ \overrightarrow{V_{sb}} = \overrightarrow{V_{s0}} \cdot \left(\bar{a}^2 + j\frac{\sqrt{3}}{2} d\right) e^{jw_s t} \\ \overrightarrow{V_{sc}} = \overrightarrow{V_{s0}} \cdot \left(\bar{a} - j\frac{\sqrt{3}}{2} d\right) e^{jw_s t} \end{cases} \quad \text{(V.44)}$$

From (V.44), the composite stator voltages can be expressed as:

$$\begin{cases} \overrightarrow{V_{ab}} = \overrightarrow{V_{sa}} - \overrightarrow{V_{sb}} = \sqrt{3}\overrightarrow{V_{s0}} \cdot (1-d) e^{j\left(w_s t + \frac{\pi}{6}\right)} \\ \overrightarrow{V_{bc}} = \overrightarrow{V_{sb}} - \overrightarrow{V_{sc}} = \sqrt{3}\overrightarrow{V_{s0}} \cdot (1-d) \cdot \bar{a}^2 e^{j\left(w_s t + \frac{\pi}{6}\right)} \\ \overrightarrow{V_{ca}} = \overrightarrow{V_{sc}} - \overrightarrow{V_{sa}} = \sqrt{3}\overrightarrow{V_{s0}} \cdot (1-d) \cdot \bar{a} e^{j\left(w_s t + \frac{\pi}{6}\right)} \end{cases} \quad \text{(V.45)}$$

From (V.44), the three components of the stator voltage can be found as follows:

$$\begin{cases} \overrightarrow{V_p} = \overrightarrow{V_{s0}} \cdot (1-d) \\ \overrightarrow{V_n} = \vec{0} \\ \overrightarrow{V_z} = \overrightarrow{V_{s0}} \cdot (-d) \end{cases} \quad \text{(V.46)}$$

From (V.46), we can conclude that symmetrical voltage dips of this case are less harmful than asymmetrical voltage dips because they contain negative sequence component are equal to zero.

- ***In case Three-Phase to Ground***

In this case, a short circuit has occurred between three phases (a, b, c) and ground, this short circuit of these three phases has resulted in a voltage dips, as shown in (V.47):

$$\begin{cases} \overrightarrow{V_{sa}} = (1-d_a)\overrightarrow{V_{s0}} e^{jw_s t} \\ \overrightarrow{V_{sb}} = (1-d_b)\overrightarrow{V_{s0}} \bar{a}^2 e^{jw_s t} \\ \overrightarrow{V_{sc}} = (1-d_c)\overrightarrow{V_{s0}} \bar{a} e^{jw_s t} \end{cases} \quad \text{(V.47)}$$

From (V.47), the three components of the stator voltage can be found as follows:

$$\begin{cases} \overrightarrow{V_p} = \overrightarrow{V_{s0}} \cdot \left(1 - \dfrac{(d_a + d_b + d_c)}{3} \right) \\ \overrightarrow{V_n} = \overrightarrow{V_{s0}} \cdot \left(\dfrac{(d_b + d_c - 2.d_a)}{6} - j \dfrac{\sqrt{3}.(d_b - d_c)}{6} \right) \\ \overrightarrow{V_z} = \overrightarrow{V_{s0}} \cdot \left(\dfrac{(d_b + d_c - 2.d_a)}{6} + j \dfrac{\sqrt{3}.(d_b - d_c)}{6} \right) \end{cases} \quad \text{(V.48)}$$

At symmetrical voltage dips, we set $d_a=d_b=d_c=d$. So the three components of the stator voltage will be as follows:

$$\begin{cases} \overrightarrow{V_p} = \overrightarrow{V_{s0}} \cdot (1 - d) \\ \overrightarrow{V_n} = \vec{0} \\ \overrightarrow{V_z} = \vec{0} \end{cases} \quad \text{(V.49)}$$

From (V.49), we can conclude that symmetrical voltage dips to ground are less harmful than asymmetrical voltage dips because they contain zero sequence component, and negative sequence component are equal to zero.

During asymmetrical dips, the inverter may face the problem of losing control of the rotor current due to the negative flux induced voltage. In such cases, the use of a crowbar does not resolve the issue since it would need to remain active throughout the entire dip, leading to disconnection of the generator from the grid. Hence, it is advisable to employ a DVR that can effectively and continuously inject the necessary voltage during asymmetrical voltage dips. A DVR is designed to monitor the grid voltage and compensate for any deviations or disturbances by injecting appropriate voltage to stabilize the system. By doing so, it ensures the sensitive loads receive a stable and reliable power supply, mitigating the impact of voltage dips and maintaining continuous operation.

The three sequence components under different dip cases are summarized in Table V.1.

Table V.1 Three Sequence Components Under Different Dip Cases

Component / Dip cases	V_p	V_n	V_z
ϕn	$V_{s0} \cdot \left(1 - \frac{d}{3}\right)$	$V_{s0} \cdot \left(-\frac{d}{3}\right)$	$V_{s0} \cdot \left(-\frac{d}{3}\right)$
$\phi\phi$	$V_{s0} \cdot \left(1 - \frac{d}{2}\right)$	$V_{s0} \cdot \left(\frac{d}{2}\right)$	$V_{s0} \cdot \left(\frac{d}{2}\right)$

asymmetrical $2\phi n$	$V_{s0}.\left(1-\frac{(d_b+d_c)}{3}\right)$	$V_{s0}.\left(\frac{(d_b+d_c)}{6}-j\frac{\sqrt{3}.(d_b-d_c)}{6}\right)$	$V_{s0}.\left(\frac{(d_b+d_c)}{6}+j\frac{\sqrt{3}.(d_b-d_c)}{6}\right)$
asymmetrical $3\phi n$	$V_{s0}.\left(1-\frac{(d_a+d_b+d_c)}{3}\right)$	$V_{s0}.\left(\frac{(d_b+d_c-2.d_a)}{6}-j\frac{\sqrt{3}.(d_b-d_c)}{6}\right)$	$V_{s0}.\left(\frac{(d_b+d_c-2.d_a)}{6}+j\frac{\sqrt{3}.(d_b-d_c)}{6}\right)$
$\phi\phi\phi$	$V_{s0}.(1-d)$	0	$V_{s0}.(-d)$
symmetrical $3\phi n$	$V_{s0}.(1-d)$	0	0

V.4 DVR

The DFIG equipped with a DVR, is protected by connecting the DVR in series between the network and the stator. Under normal grid conditions, the DVR does not compensate for the voltage, except for minimal dynamic voltage distortions. However, in the event of network voltage dips, the DVR mitigates the voltage dip using a voltage transformer. The secondary winding of the voltage transformer is connected in series between the network and the stator, while the primary winding is linked to the power inverter which is controlled by appropriate control method. This configuration enables the DVR to rectify deteriorated line voltages, thereby reducing potential issues on sensitive loads or generators. The active power formula of the DVR is shown as follows [Wes 10]:

$$P_{DVR} = (\frac{V_{nr} - V_d}{V_{nr}}).P_{load} \tag{V.50}$$

where:

$$V_{DVR} = V_{nr} - V_d \tag{V.51}$$

where: P_{DVR} is the power injected into the network using the DVR technique; P_{load} is the power absorbed or provided by the sensitive load or DFIG; V_{nr} is the normal network voltage before the dip; V_d is network voltage dip; V_{DVR} is the voltage injected into the network using the DVR technique.

The DVR technique is composed of the following parts [Alam 15]:

- Energy storage battery: The energy stored during asymmetrical dips provides the voltage needed to restore the grid voltage dips.
- Voltage Source Inverter (VSI): In this part, the stored DC voltage is converted into AC voltage using the inverter when grid voltage dips occur.

- Harmonic Filter: This strategy is used to reduce the harmonics emitted from the voltage source inverter during the conversion process from DC to AC voltage.
- Injection transformer: The primary winding of the transformer is connected to the inverter, while the secondary winding is connected in series between the grid and the sensitive load.
- DVR controller: This strategy includes dip voltage detection and compares it to the reference signal to generate a pulse width proportional to the injection voltage.

The general model of the DVR is illustrated in Figure V.4.

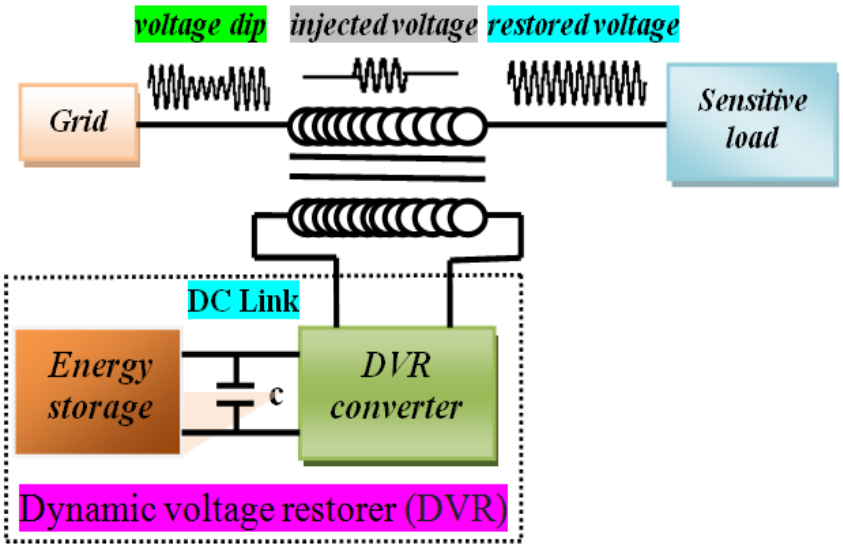

Figure V.4 General model of the DVR

The diagram of DVR strategy using FLC-SVPWM is illustrated in Figure V.5.

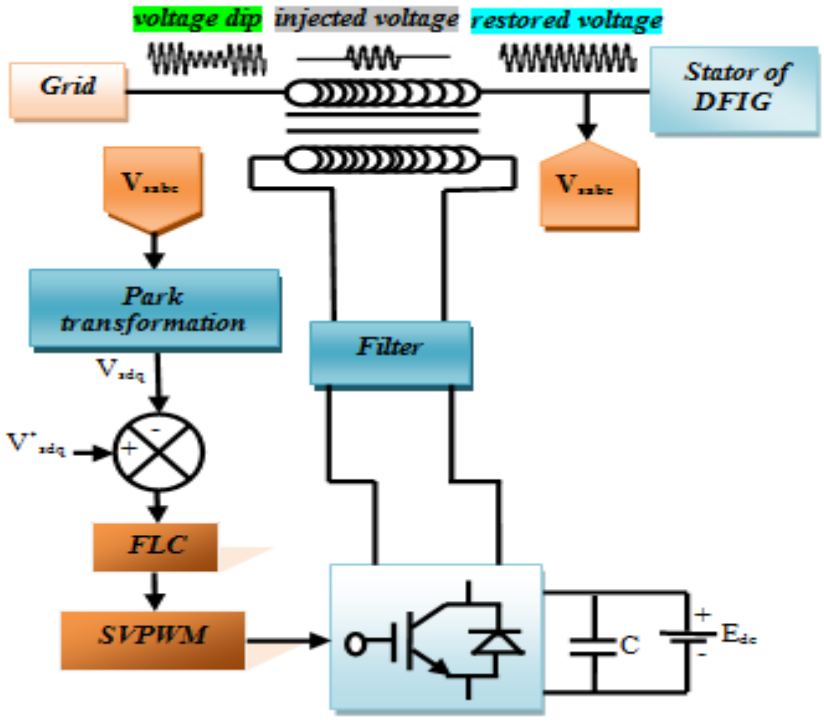

Figure V.5 Diagram of DVR strategy using FLC-SVPWM

V.5 Simulation Results

The wind speed curve is displayed in Figure V.6 (a), where its value changes randomly from 1.79 to 11.75 $m.s^{-1}$, during 3.5s. The rotor speed curve is displayed in Figure V.6 (b), where its value changes randomly from 0 to 154.1 $rad.s^{-1}$.

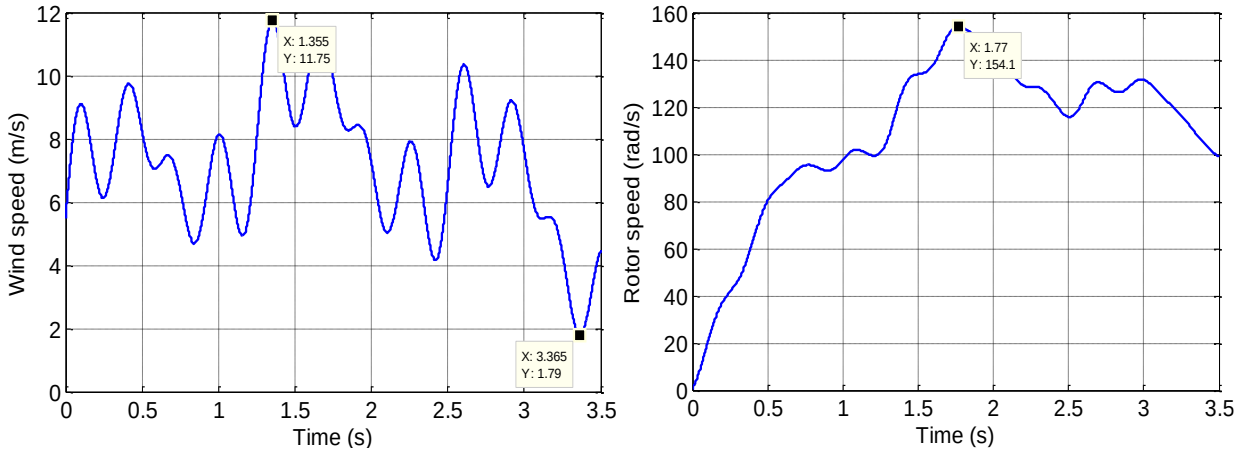

(a) (b)

Figure V.6 (a) Wind speed and (b) Rotor speed

V.5.1 DFIG-Variable Speed WT under Symmetrical Voltage Dips

Firstly, simulations of DFIG-Variable Speed WT under symmetrical voltage dips of the grid without a DVR were studied, and the impact of these dips on the DFIG was observed. The stator's active and reactive powers and their references, using PI-PWM and FLC-SVPWM, are shown in Figures V.7 and V.8, respectively.

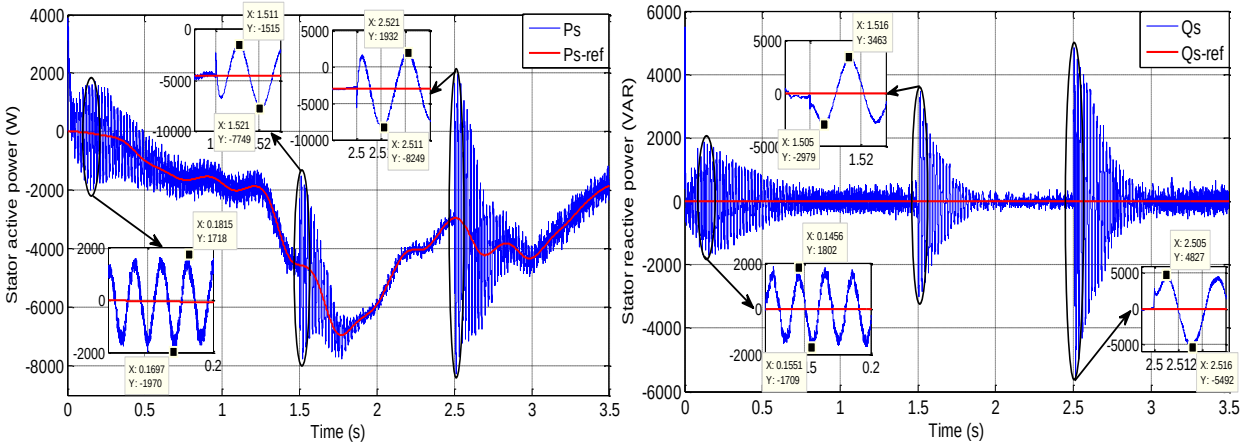

(a) (b)

Figure V.7 (a) Stator active and (b) reactive powers using PI-PWM

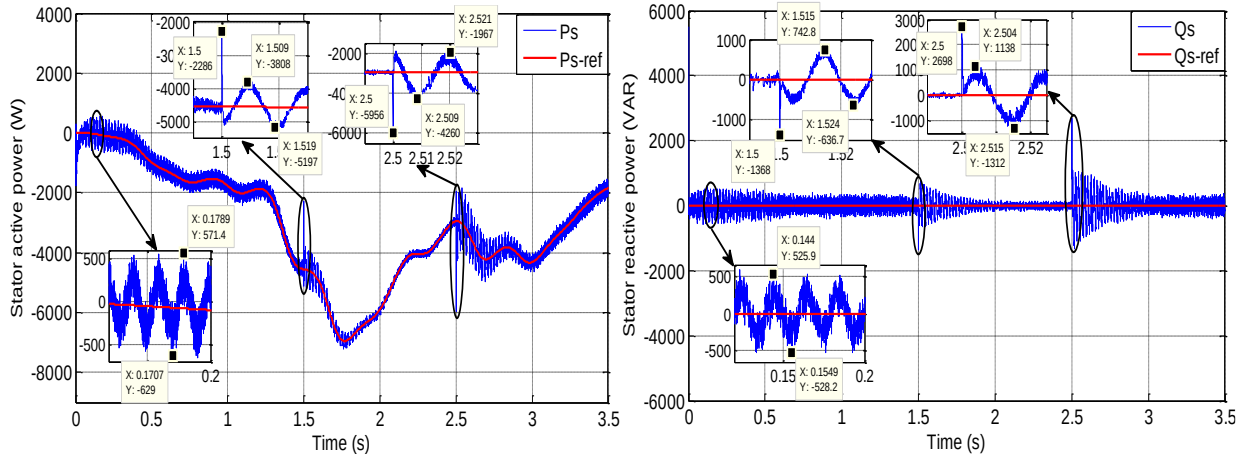

(a) (b)

Figure V.8 (a) Stator active and (b) reactive powers using FLC-SVPWM

The stator and rotor currents using PI-PWM and FLC-SVPWM under grid symmetrical voltage dips are shown in Figure V.9 and V.10, respectively.

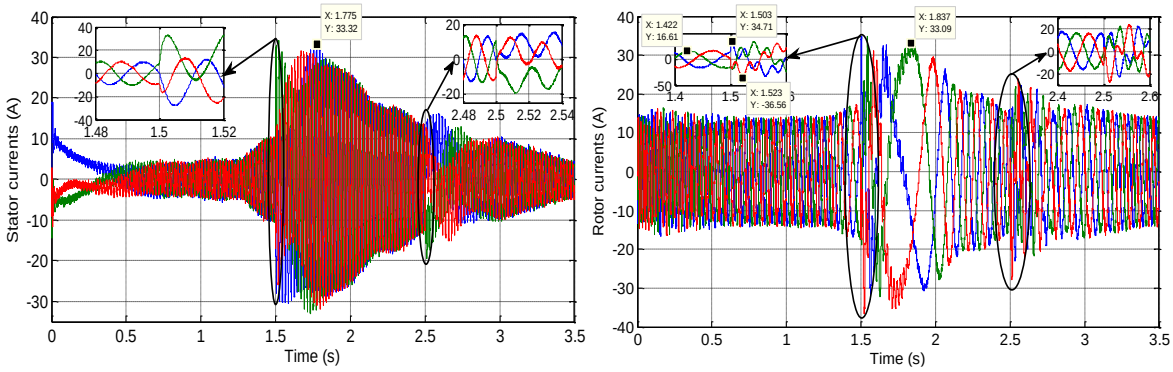

(a) (b)

Figure V.9 (a) Stator and (b) rotor currents using PI-PWM

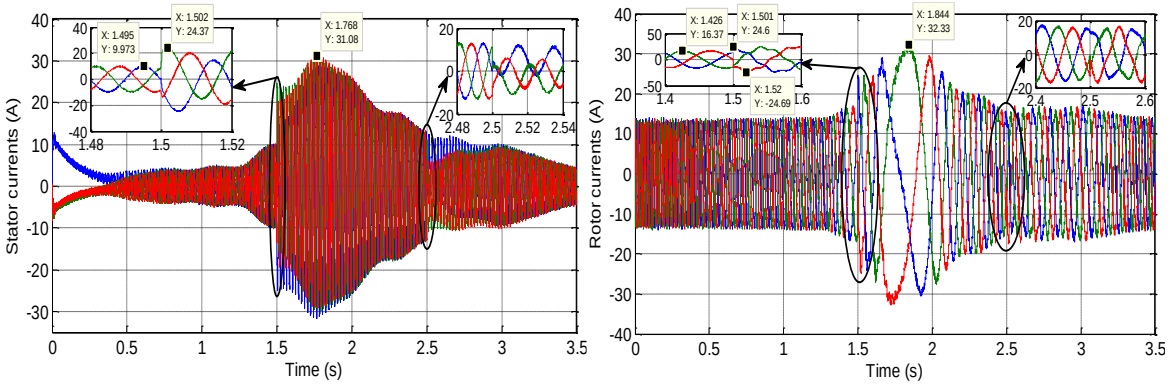

(a) (b)

Figure V.10 (a) Stator and (b) rotor currents using FLC-SVPWM

We note from Figures V.7, V.8, V.9 and V.10, that FLC-SVPWM provides better performance compared to PI-PWM, but grid voltage dips cause stator and rotor overcurrents.

V.5.2 DFIG-Variable Speed WT under Symmetrical Voltage Dips with DVR

Despite the risks posed to the DFIG by grid voltage dips, such as stator and rotor overcurrents, we can mitigate these risks by utilizing DVR technology. The three-phase grid voltage under symmetrical voltage dips, from 311.1 volt to 155.6 volt between 1.5 sec and 2.5 sec, is shown in Figure V.11. The three-phase injection voltage between 1.5 sec and 2.5 sec, using DVR controlled by PI-PWM and FLC-SVPWM are shown in Figure V.12. The three-phase restored stator voltage between 1.5 sec and 2.5sec, using DVR controlled by PI-PWM and FLC-SVPWM are shown in Figure V.13.

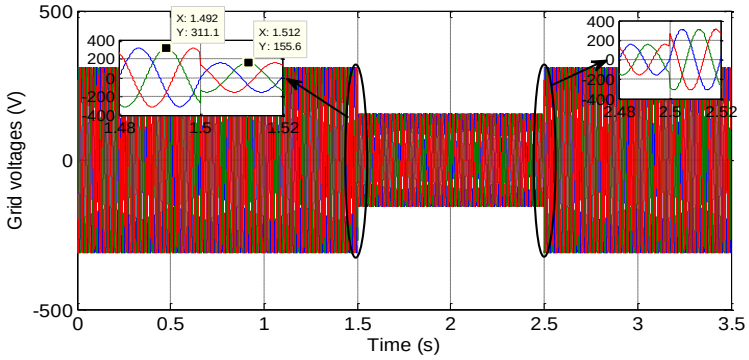

Figure V.11 Grid Side Voltage

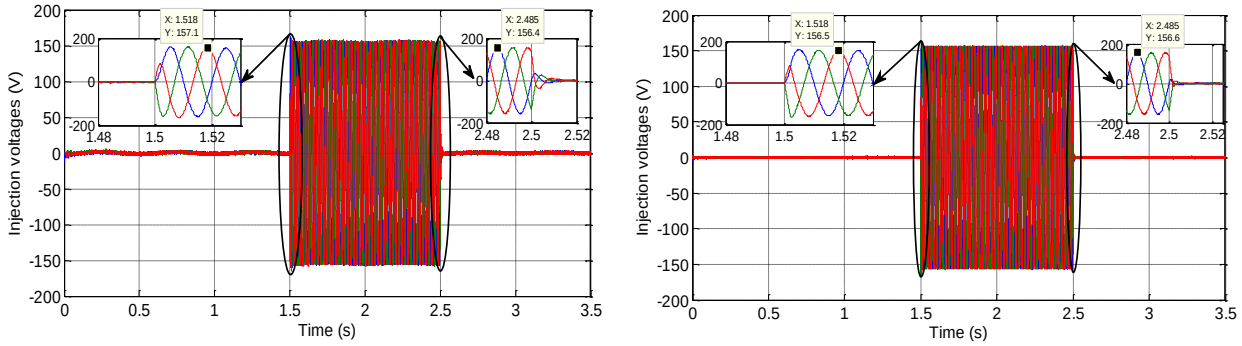

(a) (b)

Figure V.12 Injection voltage using DVR with (a) PI-PWM (b) FLC-SVPWM

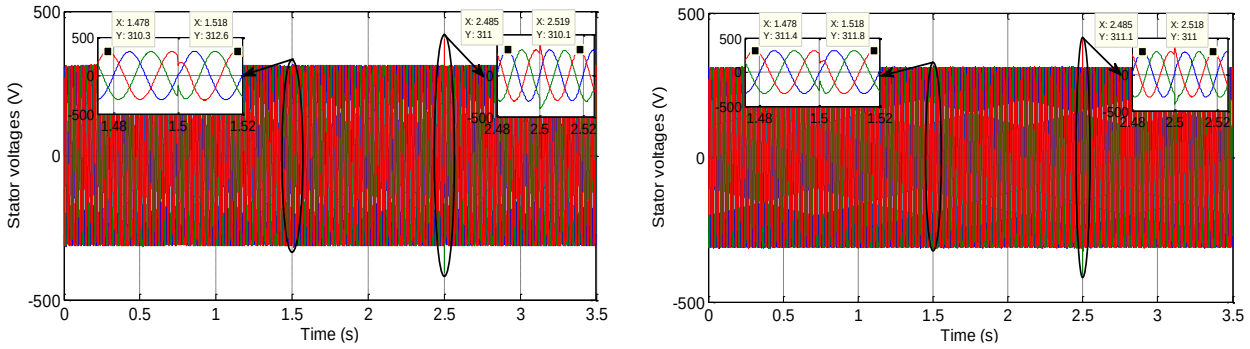

(a) (b)

Figure V.13 Stator voltage using DVR with (a) PI-PWM (b) FLC-SVPWM

THD of single-phase of the restored stator voltage using PI-PWM and FLC-SVPWM at 1.7 sec for one cycle, the period per cycle is 0.02 sec, are shown in Figures V.14 (a), and V.14 (b), respectively.

After showing Figures V.14 (a) and V.14 (b), we note that FLC-SVPWM to control the DVR gives reduced THD of single-phase stator voltage (THD = 0.19%) compared to PI-PWM (THD = 0.37%) at moment 1.7sec.

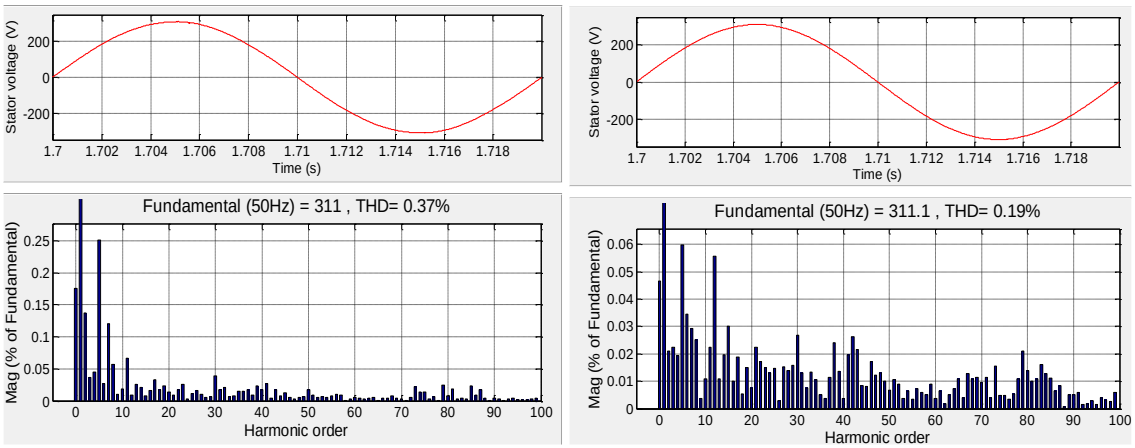

(a) (b)

Figure V.14 Harmonic spectrum of restored stator voltage using (a) PI-PWM, (b) FLC- SVPWM

DFIG is associated with the DVR, which is controlled each one of them in two methods:

- PI-PWM.
- FLC-SVPWM.

The DC-Link voltage and its zoom using PI-PWM and FLC-SVPWM to control the rotor and DVR are shown in Figures V.15 (a) and V.15 (b) respectively.

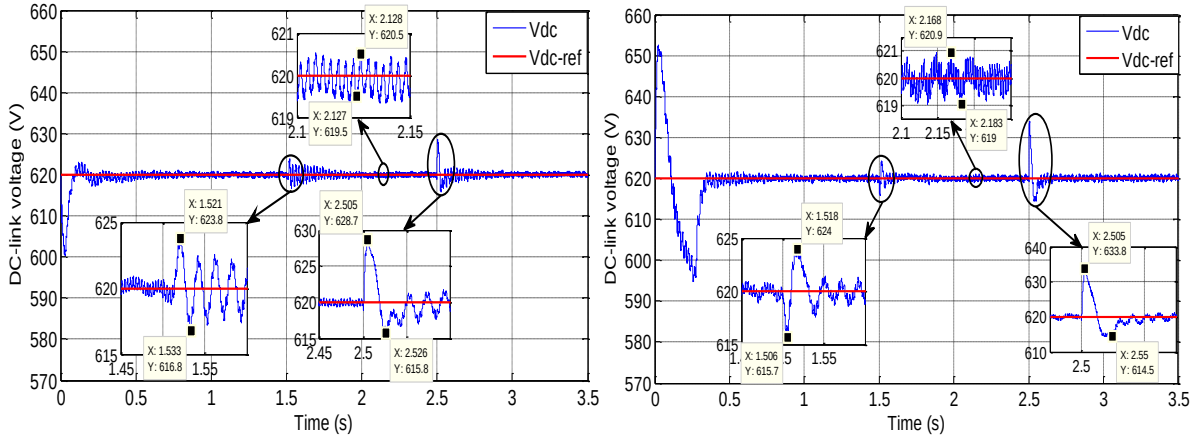

(a) (b)

Figure V.15 DC-Link voltage using (a) PI-PWM (b) FLC-SVPWM

The stator active and reactive powers and its reference using PI-PWM and FLC-SVPWM are shown in Figures V.16 and V.17, respectively.

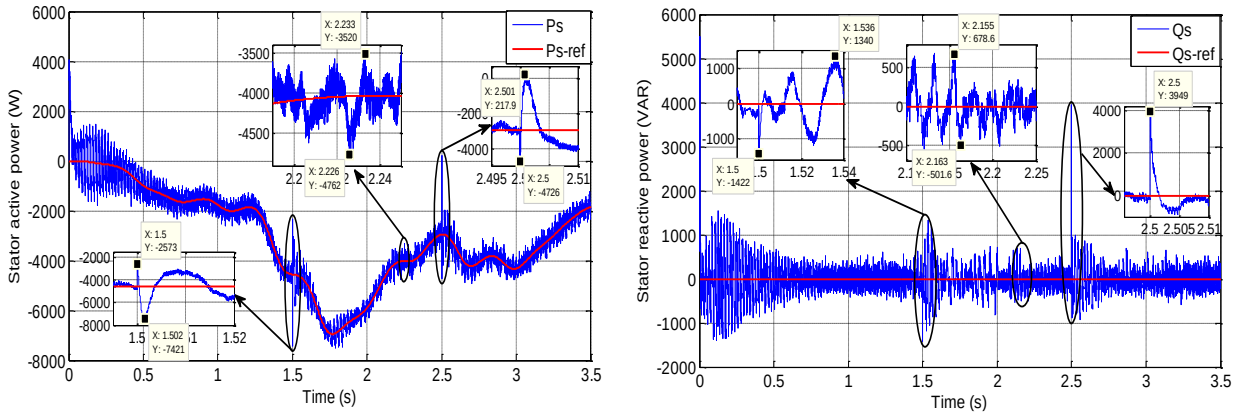

(a) (b)

Figure V.16 (a) Stator active and (b) reactive powers using PI-PWM

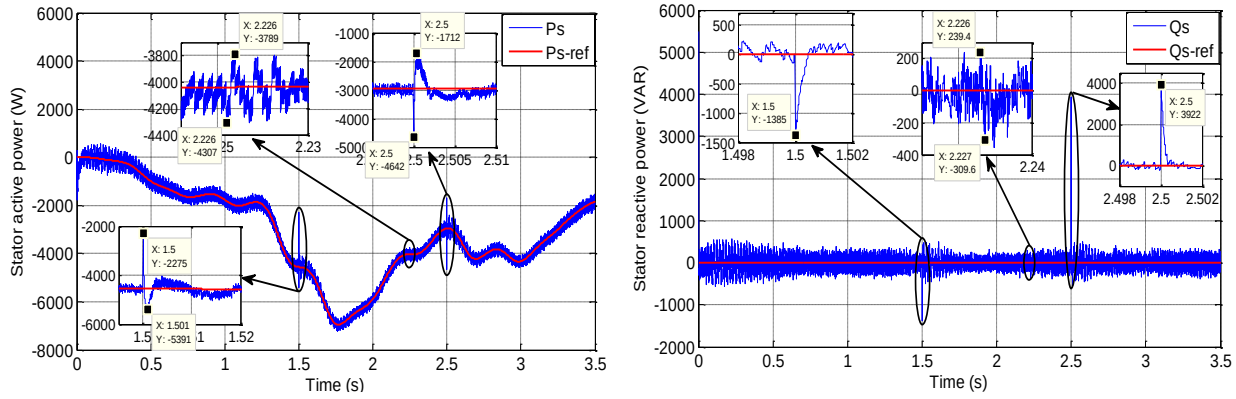

(a) (b)

Figure V.17 (a) Stator active and (b) reactive powers using FLC-SVPWM

The stator and rotor currents using PI-PWM and FLC-SVPWM are shown in Figures V.18 and V.19, respectively.

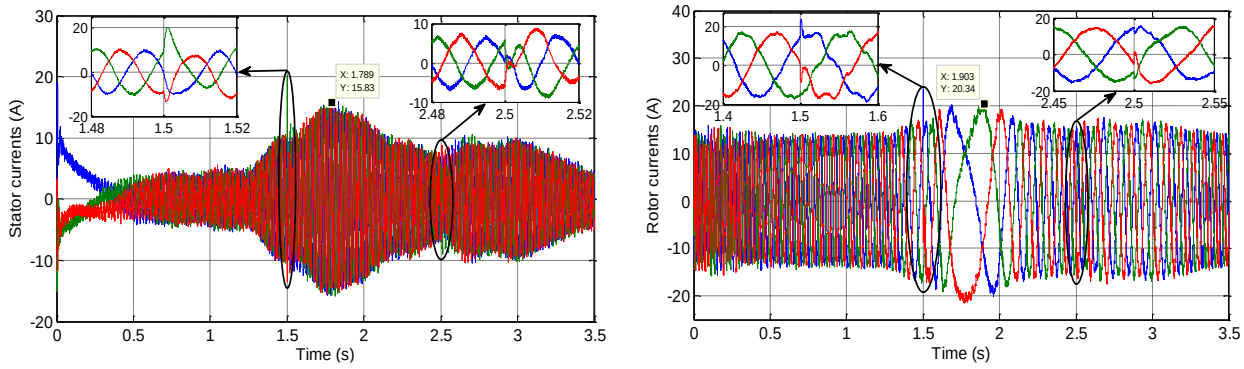

(a) (b)

Figure V.18 (a) Stator and (b) rotor currents using PI-PWM

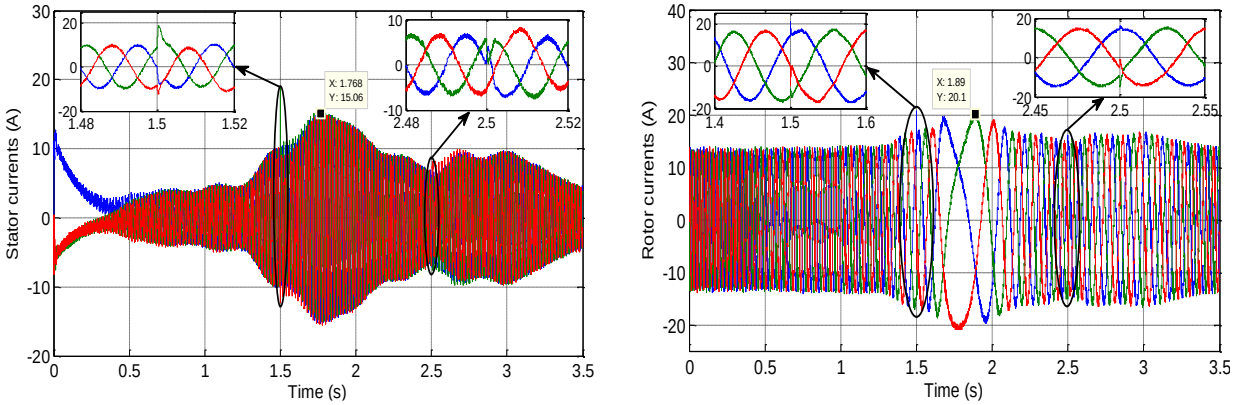

(a) (b)

Figure V.19 (a) Stator and (b) rotor currents using FLC-SVPWM

THD of single phase of the stator currents using PI-PWM and FLC-SVPWM at 1.7 sec for one cycle, the period per cycle is 0.02 sec, are shown in Figures V.20(a), and V.20(b).

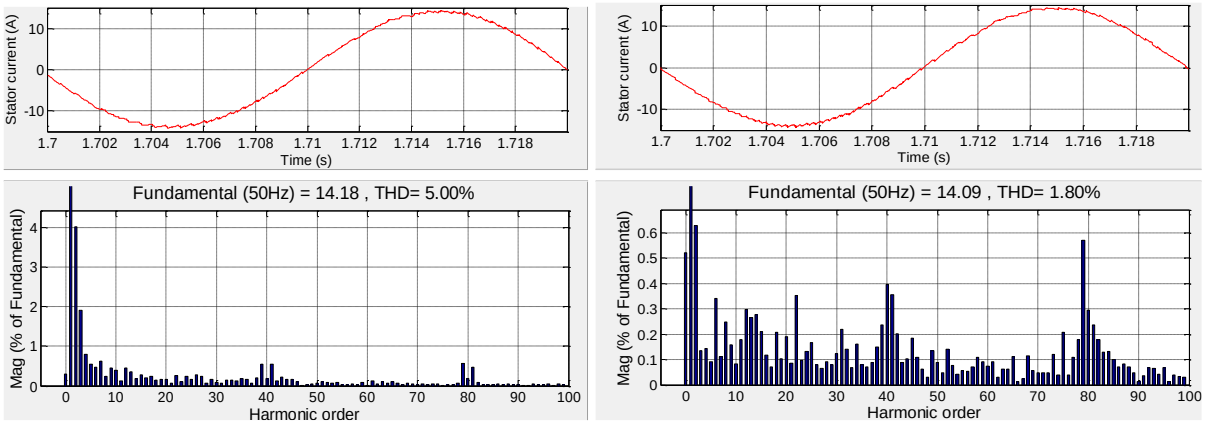

(a) (b)

Figure V.20 Harmonic spectrum of stator current using (a) PI-PWM and (b) FLC-SVPWM

After showing Figures V.20(a) and V.20(b), we note that FLC-SVPWM to control DFIG with DVR gives reduced THD of single-phase stator current (THD = 1.80%) compared to PI-PWM (THD = 5.00%) at 1.7sec.

The performance comparison between PI-PWM and FLC-SVPWM to control DFIG with DVR are summarized in Table V.2.

We note from Table V.2, that FLC-SVPWM provides better performance compared to PI-PWM.

Table V.2 Performance comparison between PI-PWM and FLC-SVPWM

Performance	Technique	
	PI-PWM	FLC-SVPWM
Overshoot of DC-Link voltage (V) at 1.5sec	4	3.8
Overshoot of DC-Link voltage (V) at 2.5sec	13.8	8.7
Undershoot of DC-Link voltage (V) at 1.5sec	4.3	3.2
Undershoot of DC-Link voltage (V) at 2.5sec	5.5	4.2
Ripples of V_{dc} (V)	1.90	1.00
THD of stator current (%)	5.00	1.80
THD of stator voltage (%)	0.37	0.19
Ripples of P_s (W)	1242	518
Ripples of Q_s (VAR)	1180.2	549
Transitional system ripple at start-up of P_s (W)	3688	1200.4
Transitional system ripple at start-up of Q_s (VAR)	3511	1054.1

V.5.3 DFIG-Variable Speed WT under Asymmetrical Voltage Dips

The rotor of DFIG is controlled, to control the active and reactive powers in two methods:

- PI controller with PWM inverter.
- FLC with SVPWM inverter.

The three-phase grid voltage under asymmetrical voltage dips, from 311.1 volt to 248.9 volt, 186.7 volt and 124 volt between moments 1.5 sec and 2.5 sec, is shown in Figure V.21.

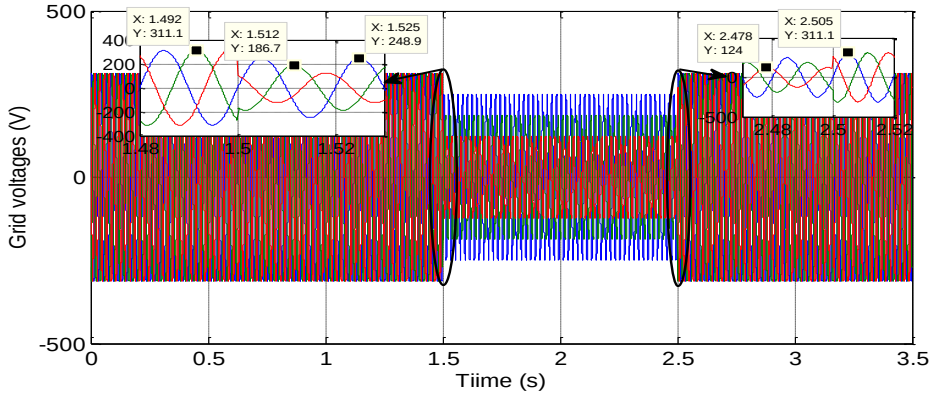

Figure V.21 Grid Side Voltage

The stator active and reactive powers and its reference using PI-PWM and FLC-SVPWM under asymmetrical voltage dips without DVR are shown in Figures V.22 and V.23.

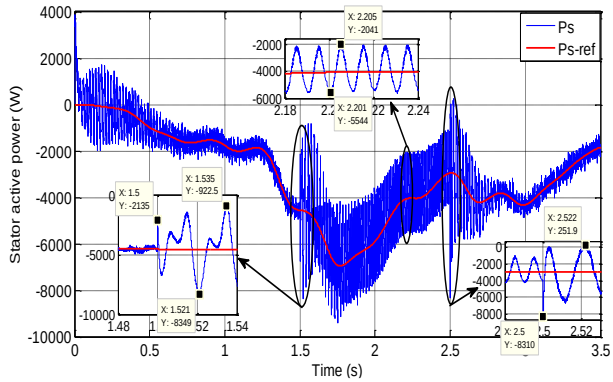

(a)

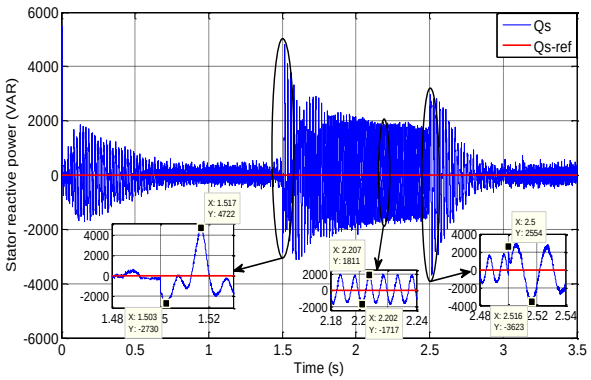

(b)

Figure V.22 (a) Stator active and (b) reactive powers using PI-PWM

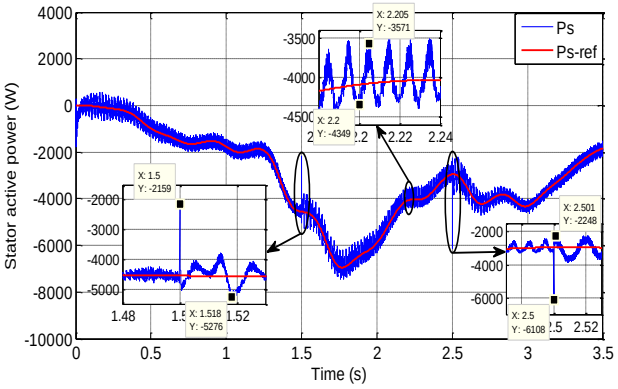

(a)

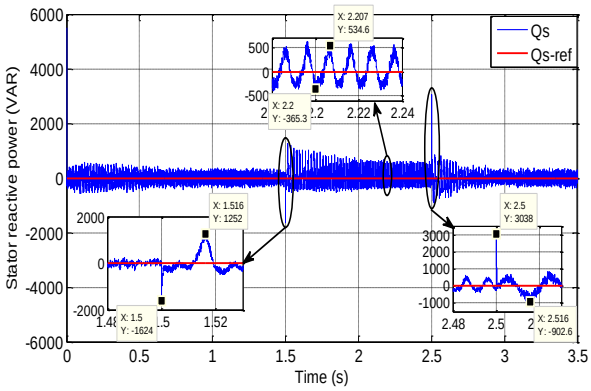

(b)

Figure V.23 (a) Stator active and (b) reactive powers using FLC-SVPWM

The stator and rotor currents using PI-PWM and FLC-SVPWM under asymmetrical voltage dips without DVR are shown in Figures V.24 and V.25, respectively.

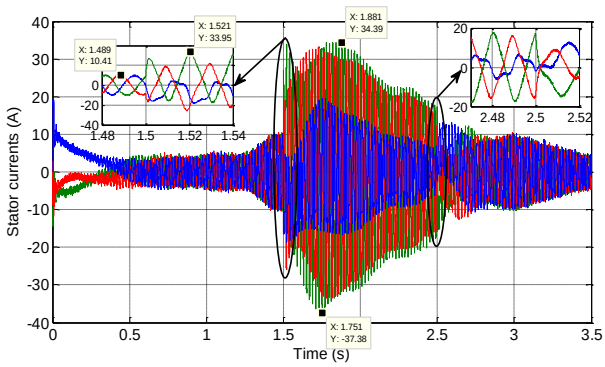

(a)

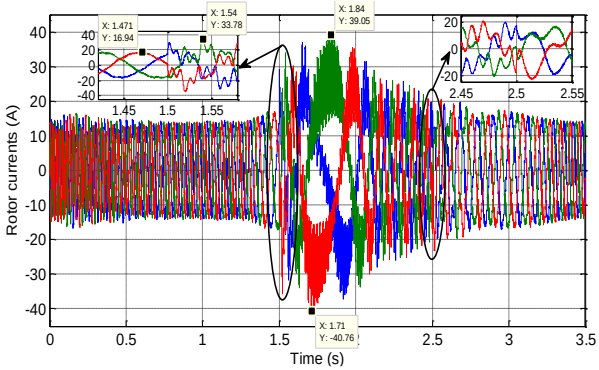

(b)

Figure V.24 (a) Stator and (b) rotor currents using PI-PWM

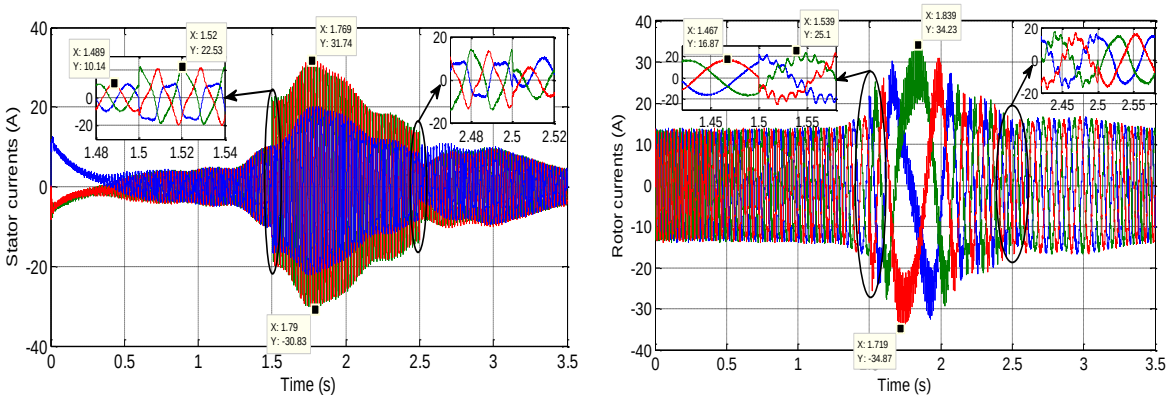

(a) (b)

Figure V.25 (a) Stator and (b) rotor currents using FLC-SVPWM

V.5.4 DFIG-Variable Speed WT under Asymmetrical Voltage Dips with DVR

V.5.4.1 DVR Simulation

Despite the risks to the DFIG due to the grid voltage asymmetrical dips, which is the stator and rotor overcurrents with an excessive increase in harmonics, we can treat the grid voltage dips using DVR technology, which is controlled by hysteresis voltage control (HVC). The three-phase injection voltage, from almost zero value to 187.1 volt, 125 volt, and 63.33 volt, between moments 1.5 sec and 2.5 sec, using DVR controlled by HVC is shown in Figure V.26(a). The three-phase restored stator voltage between moments 1.5 sec and 2.5sec, using DVR controlled by HVC is shown in Figure V.26(b).

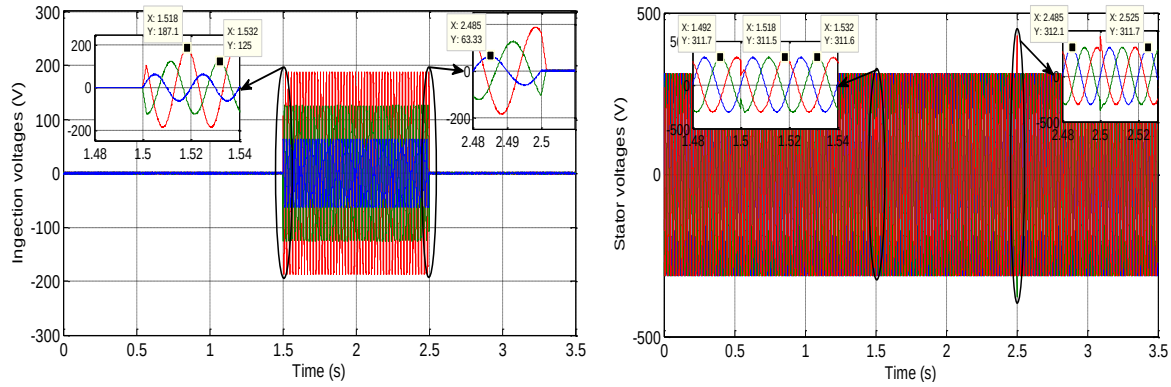

(a) (b)

Figure V.26 (a) Injection voltage and (b) Stator voltage using DVR controlled by HVC

THD of single-phase of the stator voltage using DVR controlled by HVC at moment 1.7 sec for one cycle, the period per cycle is 0.02 sec, is shown in Figure V.27.

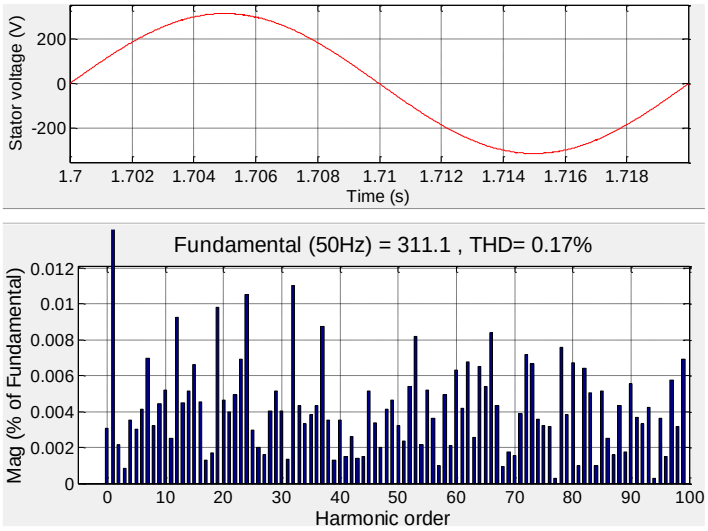

Figure V.27 Harmonic spectrum of stator voltage using DVR controlled by HVC

After showing Figure V.27, we note that DVR controlled by HVC gives very reduced THD of single-phase stator voltage (THD = 0.17%).

V.5.4.2 DFIG Simulation with DVR

The DFIG is associated with the DVR, where:

- The rotor of DFIG and DVR are controlled by PI-PWM.
- The rotor of DFIG and DVR are controlled by FLC-SVPWM.

The stator active and reactive powers and its reference using PI-PWM and FLC-SVPWM are shown in Figures V.28 and V.29, respectively.

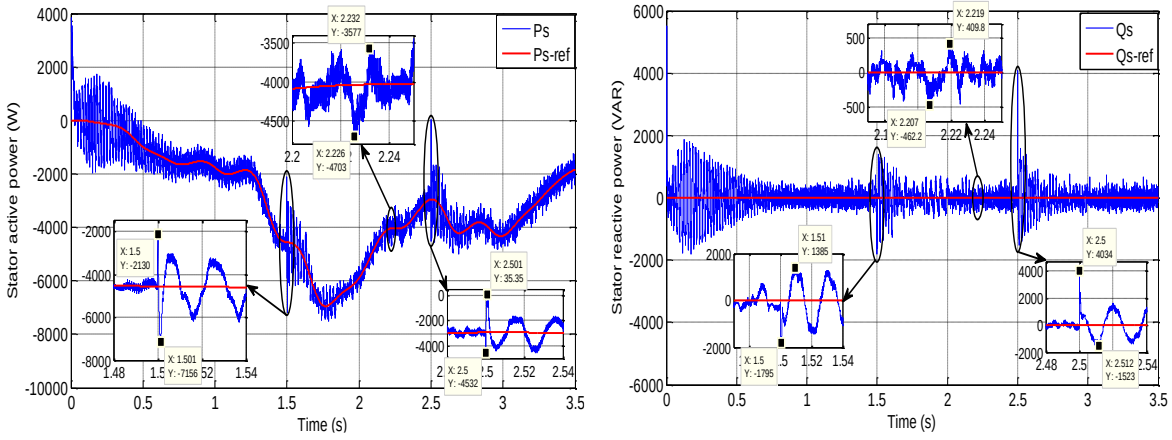

(a) (b)

Figure V.28 (a) Stator active and (b) reactive powers using PI-PWM

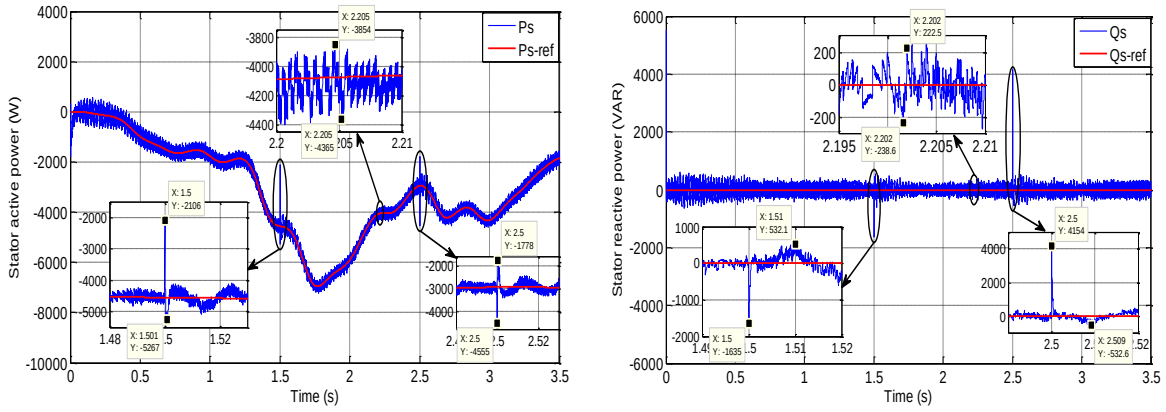

(a) (b)

Figure V.29 (a) Stator active and (b) reactive powers using FLC-SVPWM

The stator and rotor currents under asymmetrical voltage dips with DVR using PI-PWM and FLC-SVPWM are shown in Figures V.30 and V.31, respectively.

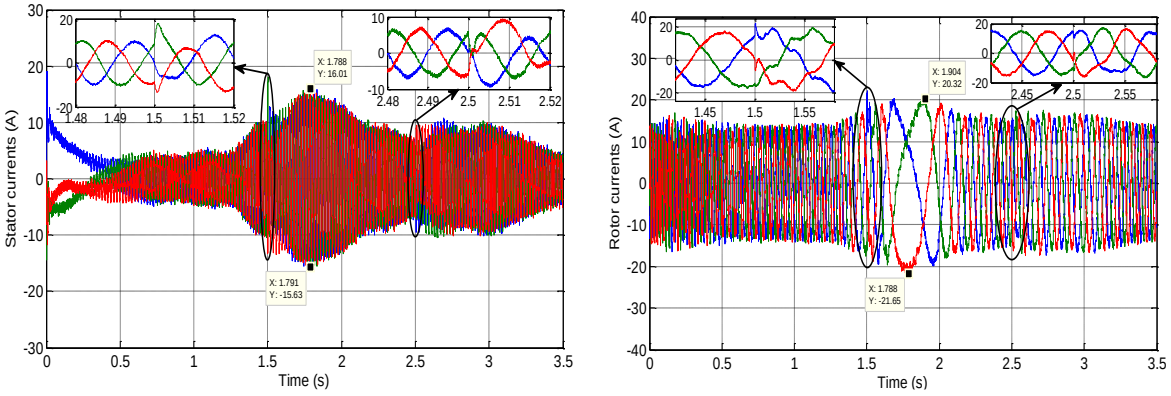

(a) (b)

Figure V.30 (a) Stator and (b) rotor currents using PI-PWM

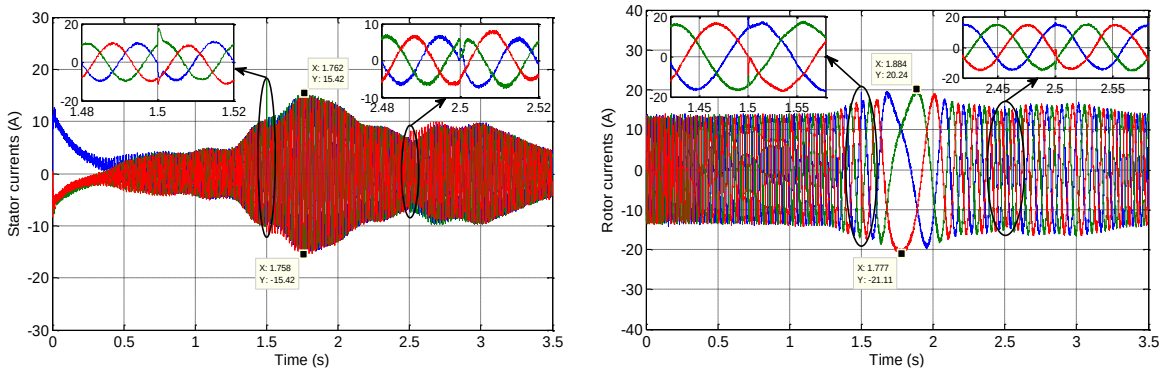

(a) (b)

Figure V.31 (a) Stator and (b) rotor currents using FLC-SVPWM

V.5.5 DFIG–Fixed Speed WT under Asymmetrical Voltage Dips

Firstly, simulations of DFIG subject to asymmetrical voltage dips of the grid without DVR were studied, and the impact of these dips on the DFIG was observed. The three-phase grid voltage under asymmetrical dips is shown in Figure V.32.

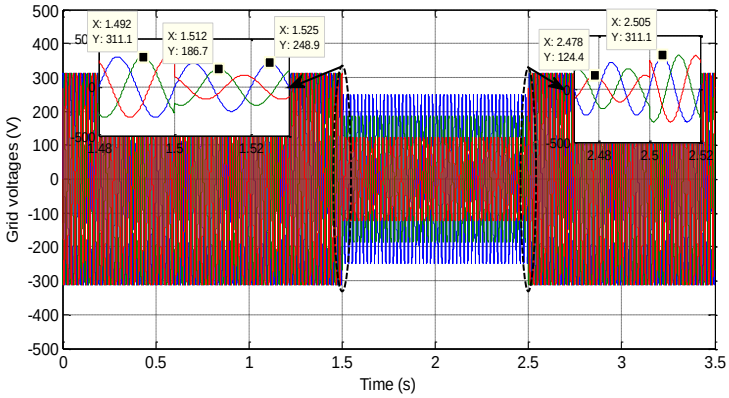

Figure V.32 Grid side voltage

The stator active and reactive powers and their reference, using PI controller, BSC, and FBSC under asymmetrical voltage dips without DVR, are illustrated in Figure V.33.

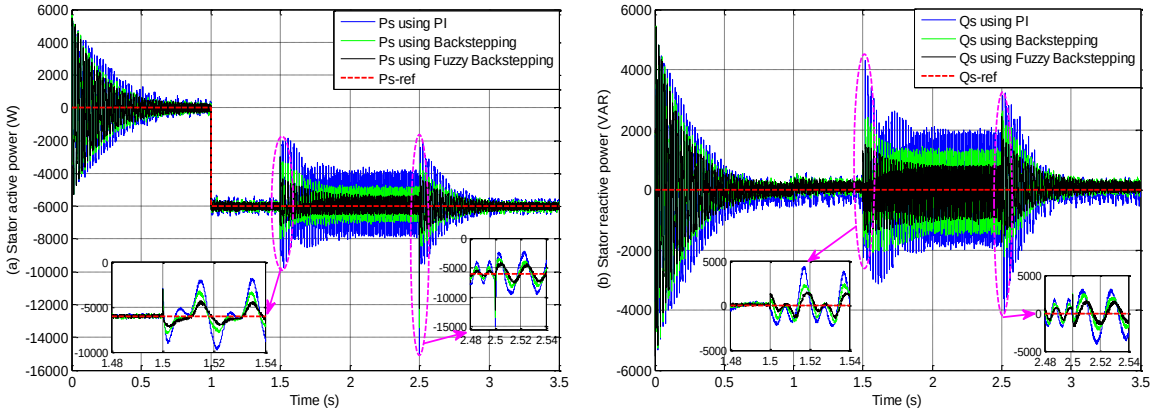

Figure V.33 (a) Stator active and (b) reactive powers using PI controller, BSC, and FBSC

We note from Figure V.33 that the asymmetrical dips in the grid voltage occurring between 1.5 sec and 2.5 sec lead to very high ripples in the active and reactive powers. In contrast, these ripples are lower using FBSC compared to BSC and PI controller.

The stator and rotor currents using PI controller, BSC, and FBSC under asymmetrical voltage dips occurring between 1.5 sec and 2.5 sec are shown in Figures V.34 and V.35, respectively.

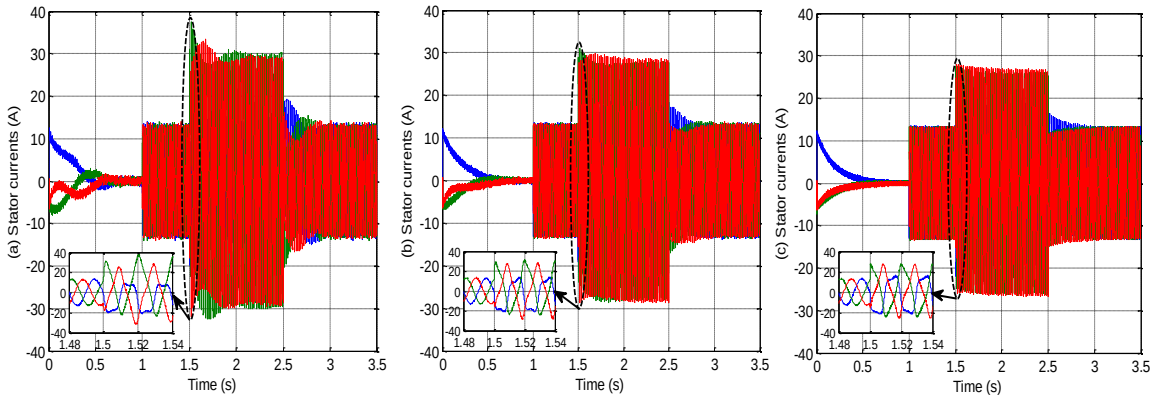

Figure V.34 Stator currents using (a) PI controller, (b) BSC, and (c) FBSC

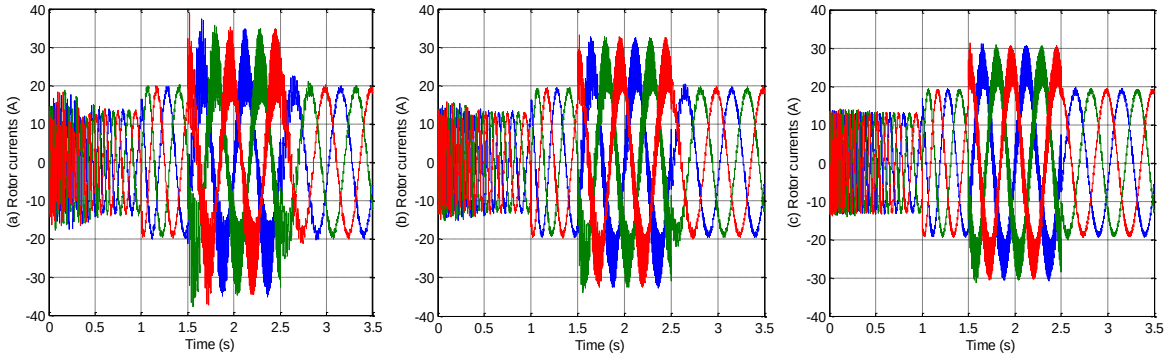

Figure V.35 Rotor currents using (a) PI controller, (b) BSC, and (c) FBSC

We note from Figures V.34 and V.35 that the asymmetrical dips in the grid voltage occurring between 1.5 sec and 2.5 sec, lead to stator and rotor overcurrents accompanied by high oscillations carried on them, which are directly proportional to the THD. which makes the asymmetrical dips be more harmful than the symmetrical dips that witness stator and rotor overcurrents with stability and no high oscillations carried on them. On the other hand, the oscillations are lower using FBSC than BSC and PI controller, though high in all control methods due to asymmetrical voltage dips.

V.5.6 DFIG–Fixed Speed WT under Asymmetrical Voltage Dips with DVR

Despite the risks faced by the DFIG due to asymmetrical voltage dips, such as stator and rotor overcurrents accompanied by high oscillations carried on them, we can mitigate these risks using DVR technique. The three-phase injection voltage and three-phase restored stator voltage using DVR-HVC are shown in Figure V.36.

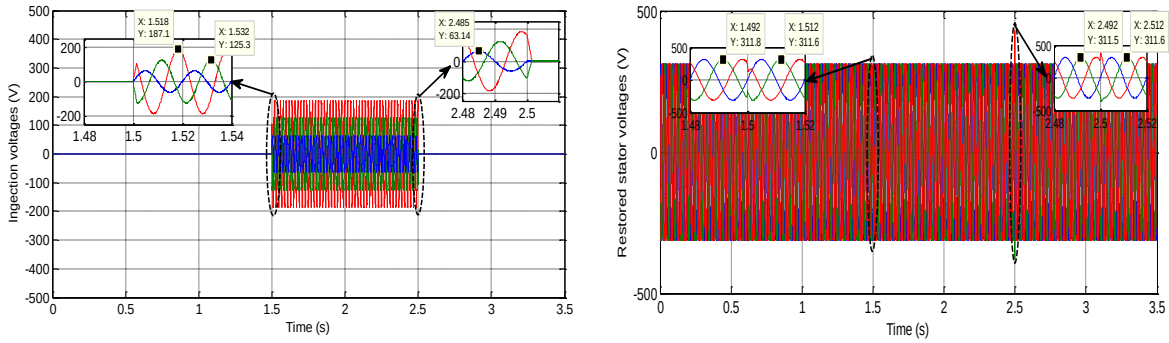

(a) (b)

Figure V.36 (a) Injection voltages and (b) restored stator voltages using DVR-HVC

The THD of single-phase of the restored stator voltage using DVR-HVC at 2.35 sec for one cycle, is shown in Figure V.37.

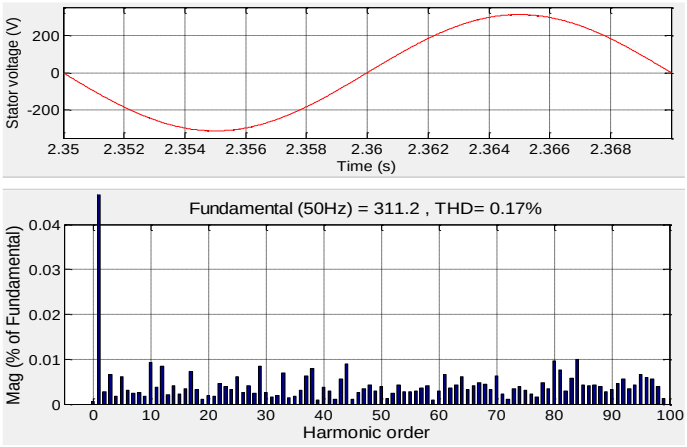

Figure V.37. Harmonic spectrum of the restored stator voltage

The stator active and reactive powers and their reference, using PI controller, BSC, and FBSC, under asymmetrical voltage dips with DVR-HVC are shown in Figure V.38.

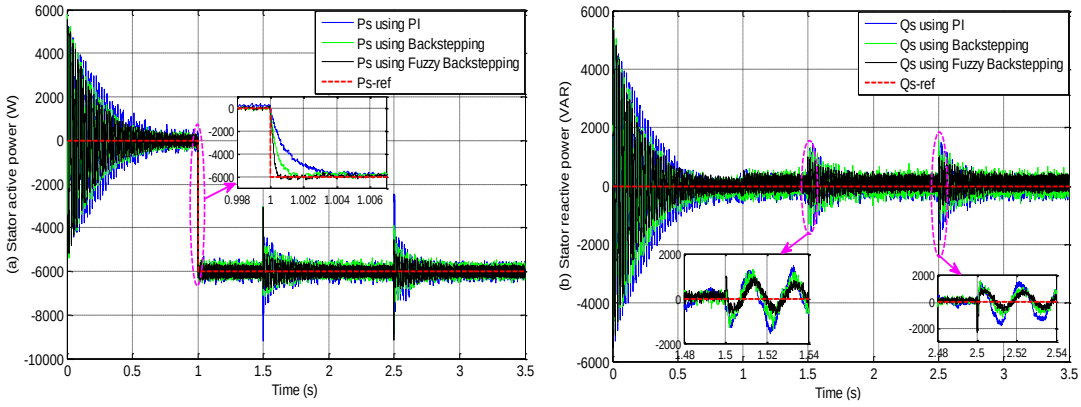

Figure V.38. (a) Stator active and (b) reactive powers using PI controller, BSC and FBSC

We note from Figure V.38 that when restoring the grid voltage that suffers from asymmetrical dips using DVR, the high ripples of active and reactive power are reduced to their normal state. In contrast, we note that the FBSC provides a faster response to the active power reference signal tracking compared to the BSC and PI controller.

The stator and rotor currents using PI controller, BSC and FBSC under asymmetrical voltage dips with DVR-HVC are shown in Figures V.39 and V.40, respectively.

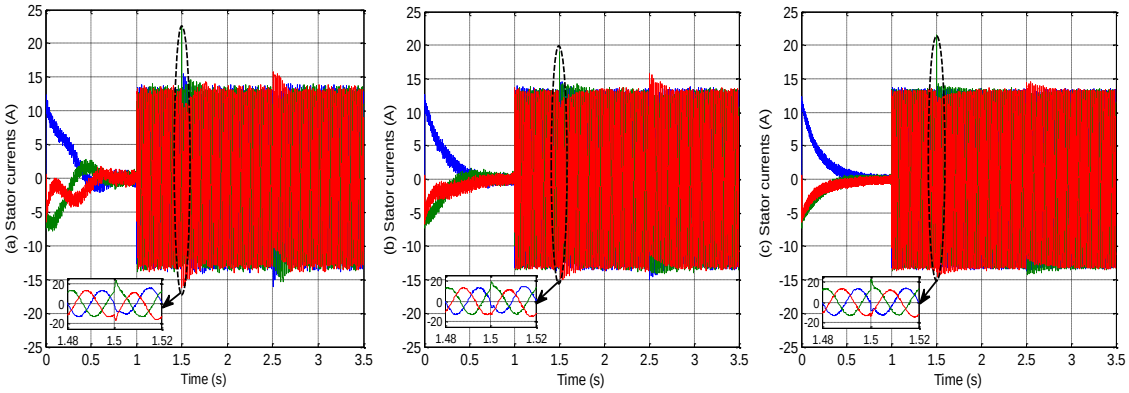

Figure V.39 Stator currents using (a) PI controller, (b) BSC and (c) FBSC

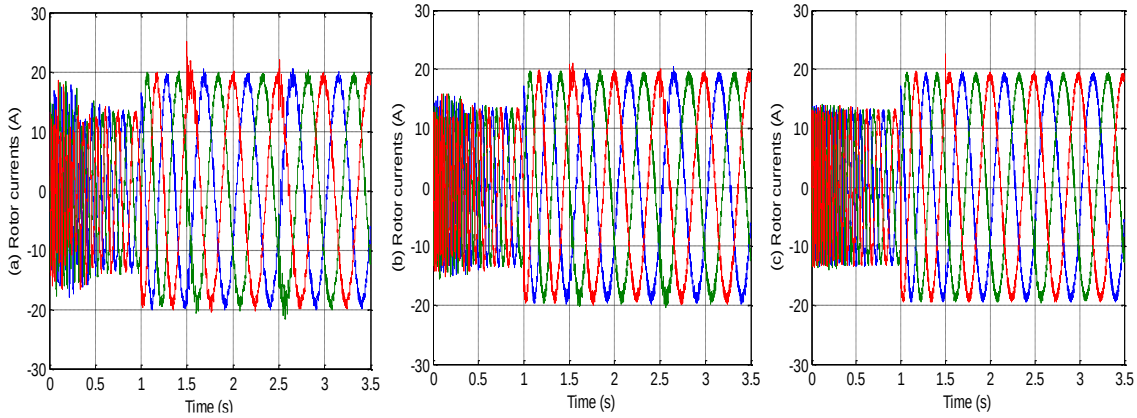

Figure V.40 Rotor currents using (a) PI controller, (b) BSC and (c) FBSC

We note from Figures V.39 and V.40 that when restoring the grid voltage that suffers from asymmetrical dips using DVR, the stator and rotor overcurrents and the oscillations carried on them are reduced to their normal state. In contrast, we note that FBSC provides better performance compared to BSC and PI controller. The THD of single-phase of the restored stator currents, at 2.35 sec for one cycle, using PI controller, BSC, and FBSC for controlling DFIG are shown in Figure V.41.

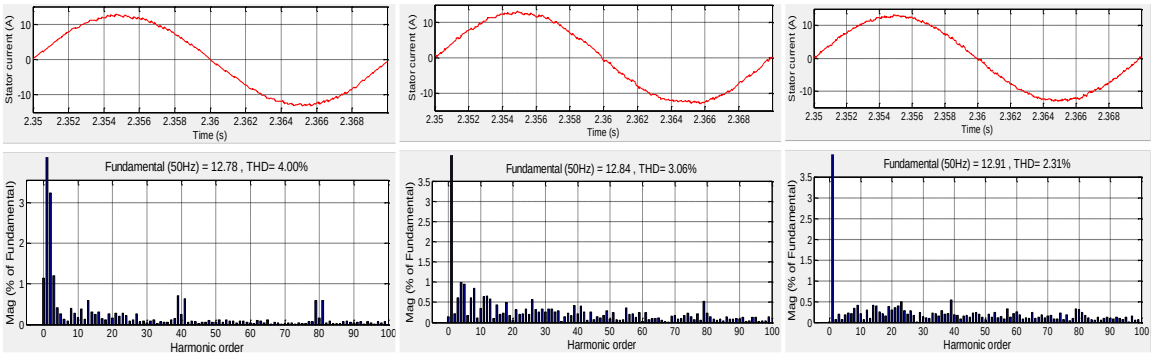

(a) (b) (c)

Figure V.41 Harmonic spectrum of the stator current using (a) PI controller, (b) BSC, and (c) FBSC

After Figures V.41(a), V.41(b) and V.41(c), we note that FBSC to control DFIG with DVR gives reduced THD of single-phase stator current (THD = 2.31%) compared to BSC (THD = 3.06%) and PI controller (THD = 4.00%) at 2.35sec.

V.5.7 Test of Parameter Variation of DFIG

In this test, the DFIG is driven by fixed-speed WT, where the rotor resistance (R_r) is increased by 100% of its rated value, and the rotor inductance (L_r) is increased by 50% of its rated value, to test the robustness of PI controller, BSC, and FBSC. The stator active power with the parameter variation of R_r (+100% of R_r) using PI controller, BSC, and FBSC is shown in Figure V.42.

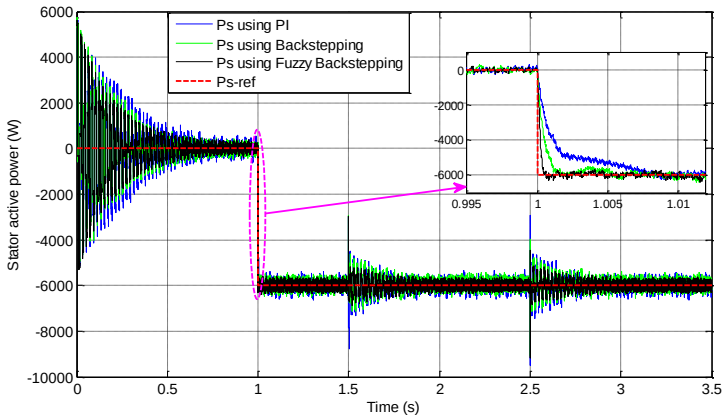

Figure V.42 Stator active power using PI controller, BSC and FBSC with +100% of R_r

After Figure V.42, we note that PI controller gives bad tracking of its reference and increases the power ripples, as for BSC illustrates good tracking and robustness with slight a few oscillations, whereas FBSC presents better tracking which ensures better robustness against the parameter variation (+100% of R_r) and lower ripple compared to PI controller

and BSC. The stator active and reactive powers with the parameter variation of L_r (+50% of L_r) using PI controller, BSC, and FBSC are shown in Figure V.43.

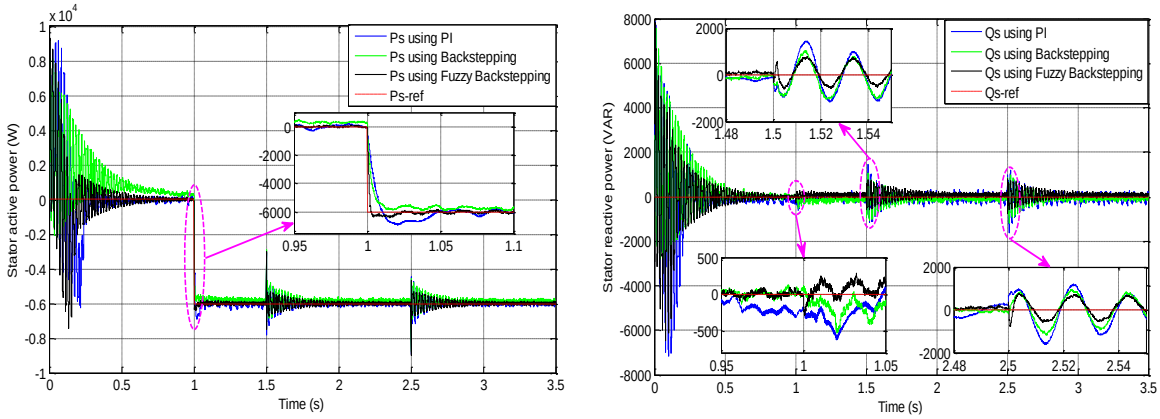

(a) (b)

Figure V.43 (a) Stator active and (b) reactive powers using PI controller, BSC, and FBSC with +50% of L_r

After Figure V.43, we note that PI controller gives bad tracking of its reference and high ripples, as for BSC illustrates bad tracking and low ripples, whereas FBSC presents better tracking which ensures better robustness against the parameter variation (+50% of L_r) and lower ripple compared to BSC and PI controller. In conclusion, the results extracted from the previous figures are summarized in Table III.

Table V.3 Performance Comparison between PI Controller, BSC, and FBSC

Technique / Performance		PI controller	BSC	FBSC
THD (%) of stator current		4.00	3.06	2.31
Falling time of stator active power without parameter variation (sec)		0.0055	0.0020	0.0006
Stator active power with +100% of R_r	Falling time (sec)	0.0078	0.0020	0.0006
	Ripples	High	Low	Low
	Tracking	Bad	Good	Good
Stator active power with +50% of L_r	Falling time (sec)	0.0477	0.0159	0.0026
	Ripples	High	Low	Low
	Tracking	Bad	Bad	Good

From Table V.3, we note that the proposed FBSC provides better performance, in terms of a faster falling time (0.0006s), and reduced THD (2.31%), in addition FBSC shows better robustness against the parameter variation, compared to BSC and PI controller.

V.6 Conclusion

DVR strategy is presented in this chapter and applied to restore grid voltage under symmetrical and asymmetrical voltage dips. Firstly, DFIG was studied under symmetrical voltage dips without a DVR, we found that there is stator and rotor overcurrents due to these dips, with stability in the oscillations carried on it and the THD, after that DFIG was subjected to asymmetrical voltage dips, leading to stator and rotor overcurrents, accompanied by high oscillations carried on it corresponds to a significant increase in THD, this makes asymmetrical voltage dips more harmful than symmetrical dips, due to the negative flux that contributes to increased oscillations and THD. To solve this problem, a DVR is implemented to compensate the symmetrical and asymmetrical dips in the network voltage and to protect the DFIG from stator and rotor overcurrents accompanied by high oscillations carried on them, and to return it to its normal condition as it was approximately before the voltage dips occurred. The proposed FBSC technique has also been presented and validated for controlling the rotor side converter of DFIG to enhance the performance of the generator control. The suggested FBSC is compared with BSC and PI controller. Simulation results obtained by MATLAB/Simulink demonstrate that the proposed FBSC improves the performance for optimum control of stator active and reactive powers. This improvement is appeared several performances in terms of faster falling time for tracking reference signals, lower ripple due to error reduction, high robustness against parameter variations, and reduced THD of the stator currents compared to BSC and PI controller. Overall, the combination of enhanced control of DFIG rotor and DVR can provide a reliable and robust solution for maintaining power quality and stability in power systems.

General Conclusion

General Conclusion

The configuration of the WT based on DFIM that was studied in this thesis is that the stator is connected directly to the grid without power converters to ensure a voltage free from harmonics, as for the rotor, it is connected to a relatively small power converter, whose capacity is estimated at 30% of the nominal power of the generator, which makes it less expensive and more economical, this proposed configuration is commensurate with the variable wind speed by controlling the rotor currents based on the stator active and reactive power to obtain a constant frequency and a constant voltage amplitude synchronized with the grid voltage. Several control techniques have been applied, including vector control using classical PI, to ensure separation between active and reactive power. The active power is set by the wind turbine based on MPPT strategy, as for the reactive power is always set at zero. The DC voltage was controlled using PI controller, which converts the DC voltage error into reference current of d- axis, while the reference current of q-axis is set at zero, all this to ensure permanent and continuous storage of energy in the inverter input. The change in the pulse width has a significant effect on the stator active and reactive power ripples and THD of the stator and rotor currents, as space vector pulse width modulation (SVPWM) gives lower ripple of the stator active and reactive powers and reduced THD of the stator and rotor currents compared to the classical PWM.

BSC contributes to the robustness and stability of the WT system by choosing the appropriate Lyapunov function gain for stability, this technique is effective with non-linear systems. FLC is characterized by input and output gains, where these gains are not related to the machine parameters and are not subject to a mathematical rule, which makes it robust and effective in non-linear systems and very robust against parameter variation and reduces the error of the measured signal included to reduce the ripple and THD. Symmetrical dips in the grid voltage cause stator and rotor overcurrents with stability in THD, and stability in active and reactive power ripples. As for the asymmetrical voltage dips, they are more harmful than the symmetrical dips due to the stator and rotor overcurrents accompanied by high oscillations carried on them corresponds to a significant increase in THD, and significant high in stator active and reactive power ripples, due to the negative flux generated by this asymmetrical dips. Symmetrical and asymmetrical grid voltage dips were restored using DVR. The main objective of this thesis is to improve the control of DFIG rotor using advanced control techniques (BSC, FLC, FBSC) to improve the quality of stator active and

reactive powers and to restore the grid voltage dips using DVR, to ensure the continuity of the generated power and its uninterrupted. Overall, the combination of enhanced DFIG control and DVR can provide a reliable and robust solution to maintain uninterrupted power quality.

Appendix

Appendix

Nominal values:

The nominal values of DFIG are given as follows:

P_s = 7.5kW, f_s = 50Hz, V_s = 220/380 V.

Parameters of DFIG are given as follows:

R_s = 0.455 Ω

R_r = 0.62 Ω

L_s = 0.084 H

L_r = 0.081 H

M = 0.078 H

P = 2

Mechanical constants:

J_g= 0.3125 kg.m^2

f_g= 6.73.10-3 N.m.s^{-1}

Parameters of wind turbine are given as follows:

P_{tur} = 10kw, G = 5.4, ρ = 1.22 kg.m^{-2}, R = 3, Number of blades = 3,

J_{tur} = 0.042 kg.m^2, f_{tur} = 6.73.10-3N.m.s^{-1}.

Parameters of RL filter and DC bus are as follows:

R_f = 0.3Ω, L_f=0.014H, C = 2.10-3F.

References

References

-A-

[Abb 12-13] Abbas,Y.K. (2012-2013). Backstepping Control Design Lab. For 4th Year Control Engineering Branch, Control Engineering Department, Iraq-Baghdad, 1-38.

[Abd 18] Abdelghafour, H., Abderrahmen, B., Samir, Z., & Riyadh, R. (2018). Backstepping control of a doubly-fed induction machine based on fuzzy controller. *European Journal of Electrical Engineering*, *20*(5-6), 645-657.

[Abo 18] Abouzeid, I., Badr, M. A., Sweif, R., & Helmy, D. (Jan. – Feb. 2018). Interpretation of the Operation Modes of the Doubly Fed Induction Machine in Wind Energy Systems. *IOSR Journal of Electrical and Electronics Engineering, 13(1), 30-36*.

[Alam 15] Alam, M. S., Siddiquee, S. S., Islam, M. K., Arafat, M. I. M., & Reza, M. H. (2015, May). Implementation and control of low voltage Dynamic Voltage Restorer using park's transformation for compensating voltage sag. In 2015 International Conference on Electrical Engineering and Information Communication Technology (ICEEICT) (pp. 1-4). IEEE.

[Alb 00] Albertos, P., Sala, A., & Olivares, M. (2000, December). Fuzzy logic controllers. Methodology. Advantages and drawbacks. In Proc. Congreso Español sobre Tecnologías y Lógica Fuzzy (pp. 1-11).

[Als 18] Alshibani, A. J., Hasanah, R. N., & Suyono, H. (2018). Grid Voltage Dip Impacts on the DFIG Wind Turbine and Its Main AC Contactor Performances. Jurnal EECCIS (Electrics, Electronics, Communications, Controls, Informatics, Systems), 12(2), 54-60.

[Ama 20] Amaitik, N. (2020). The Basics of Fuzzy Systems Technology: A Complete Tutorial.

[Ame 03] Amenedo, J. L. R., & Feito, J. S. (2003). Tecnología de los aerogeneradores. In *Sistemas eólicos de producción de energía eléctrica* (pp. 98-179). Rueda.

[Amr 16] Amrane, F., Chaiba, A., Babes, B. E., & Mekhilef, S. (2016). Design and implementation of high performance field oriented control for grid-connected doubly fed induction generator via hysteresis rotor current controller. Rev. Roum. Sci. Techn.-Electrotechn. Et Energ, 61(4), 319-324.

[Aou 18] Aounallah, T., Essounbouli, N., Hamzaoui, A., & Bouchafaa, F.(2018). Algorithm on fuzzy adaptive backstepping control of fractional order for doubly-fed induction generators. IET Renewable Power Generation, 12(8), 962-967.

[Ari 22] Arif, A., Bekakra, Y., & Attous, D. B. (2022). Fuzzy Logic Control Using SVPWM to Enhance the Control of the DFIG Driven by a Wind Turbine. ECTI Transactions on Electrical Engineering, Electronics, and Communications, 20(1), 39-50.

[Art 19] Artigao, E., Honrubia-Escribano, A., & Gomez-Lazaro, E. (2019). In-service wind turbine DFIG diagnosis using current signature analysis. *IEEE Transactions on Industrial Electronics*, *67*(3), 2262-2271.

[Azz 17] Azzaoui, M., & Mahmoudi, H. (2017). Fuzzy-PI control of a doubly fed induction generator-based wind power system. Int. J. Autom. Control., 11(1), 54-66. https://doi.org/ 10.1504/IJAAC.2017.080819

-B-

[Bai 06] Bai, Y., & Wang, D. (2006). Fundamentals of fuzzy logic control—fuzzy sets, fuzzy rules and defuzzifications. In Advanced fuzzy logic technologies in industrial applications (pp. 17-36). Springer, London.

[Bai 15] Bai, Y., Kou, B., & Chan, C. C. (2015). A simple structure passive MPPT standalone wind turbine generator system. *IEEE Transactions on Magnetics*, *51*(11), 1-4.

[Bed 14] Bedoud, K., Ali-Rachedi, M., Lakel, R., & Bahi, T. (2014). Modeling and control of the wind energy conversion systems based on DFIG under sub-and super-synchronous operation modes. Proceedings of Engineering & Technology (PET), 9(2015).

[Bek 09] Bekakra, Y., & Attous, D. B. (2009, November). A sliding mode speed and flux control of a doubly fed induction machine. In *2009 International Conference on Electrical and Electronics Engineering-ELECO 2009* (pp. I-174-I-178.). IEEE.

[Bek 12] Bekakra, Y., & Attous, D. B. (2012). Comparison between fuzzy sliding mode and traditional IP controllers in a speed control of a doubly fed induction motor. *ECTI Transactions on Electrical Engineering, Electronics, and Communications*, *10*(2), 189-197.

[Bek 13] Bekakra, Y., & Attous, D. B. (2013). DFIG sliding mode control driven by wind turbine with using a SVM inverter for improve the quality of energy injected into the electrical grid. *ECTI Transactions on Electrical Engineering, Electronics, and Communications*, *11*(1), 63-75.

[Ben 20-1] Benbouhenni, H., Boudjema, Z., & Belaidi, A. (2020). Mathematical Modelling of Engineering Problems. Journal homepage: http://iieta. org/journals/mmep, 7(2), 223-236.

[Ben 20-2] Benbouhenni, H., Boudjema, Z., & Belaidi, A. (2020). Power ripple reduction of DPC DFIG drive using ANN controller. *Acta Electrotechnica et Informatica*, *20*(1), 15-22.

[Ber 19] Berrezzek, F., Khelil, K., & Bouadjila, T. (2019, November). Estimation of wind energy potential and Weibull parameter extrapolation of the city of Annaba, Algeria. In *2019 International Conference on Advanced Electrical Engineering (ICAEE)* (pp. 1-5). IEEE.

[Bol 00] Bollen, M. H., & Styvaktakis, E. (2000, October). Tutorial on voltage sag analysis. In Ninth International Conference on Harmonics and Quality of Power. Proceedings (Cat. No. 00EX441) (Vol. 1, pp. 193-194). IEEE.

[Boude 19] Bouderbala, M., Bossoufi, B., Lagrioui, A., Taoussi, M., Aroussi, H. A., & Ihedrane, Y. (2019). Direct and indirect vector control of a doubly fed induction generator based in a wind energy conversion system. *International Journal of Electrical and Computer Engineering*, *9*(3), 1531.

[Boudj 13] Boudjema, Z., Meroufel, A., Djerriri, Y., & Bounadja, E. (2013). Fuzzy sliding mode control of a doubly fed induction generator for wind energy conversion. *Carpathian Journal of Electronic and Computer Engineering*, *6*(2), 7–14.

-C-

[Cas 19] Castellani, F., Astolfi, D., Peppoloni, M., Natili, F., Buttà, D., & Hirschl, A. (2019). Experimental vibration analysis of a small scale vertical wind energy system for residential use. *Machines*, *7*(2), 35.

-D-

[Dou 15] Doumi, M., Aissaoui, A. G., Tahour, A., Abid, M., & Tahir, K. (2015, November). Nonlinear backstepping control of a double-fed induction generator. In *2015 International Conference on Renewable Energy Research and Applications (ICRERA)* (pp. 665-670). IEEE.

[Dum 19] Dumont, A. (2019). Master thesis: Mitigation of voltage sags by a voltage conditioner.

-F-

[Fat 15] Fateh, F., White, W. N., & Gruenbacher, D. (2015). A maximum power tracking technique for grid-connected DFIG-based wind turbines. IEEE Journal of Emerging and Selected Topics in Power Electronics, 3(4), 957-966.

-G-

[Gho 02] Ghosh, A., & Ledwich, G. (2002). Compensation of distribution system voltage using DVR. IEEE Transactions on power delivery, 17(4), 1030-1036.

[Gov 14] Govindarajan, N., & Raghavan, D. (2014). Doubly fed induction generator based wind turbine with adaptive neuro fuzzy inference system controller. *Asian Journal of Scientific Research*, *7*(1), *45-55.*

-H -

[Hach 20] Hachemi, H., Allali, A., &Belkacem, B. (2020). Control of the power quality for a DFIG powered by multilevel inverters. *International Journal of Electrical and Computer Engineering (IJECE)*, *10*(5), 4592-4603.

[Har 19] Harandi, M. J., Liasi, S. G., Nikravesh, E., & Bina, M. T. (2019, February). An improved control strategy for DFIG low voltage ride-through using optimal demagnetizing method. In *2019 10th international power electronics, drive systems and technologies conference (PEDSTC)* (pp. 464-469). IEEE.

[Hash 18] Hashemi, A. (2018). Doubly-Fed Induction Machines: Model, Control and Applications.

[Haz 17] Hazari, M. R., Mannan, M. A., Muyeen, S. M., Umemura, A., Takahashi, R., & Tamura, J. (2017). Stability augmentation of a grid-connected wind farm by fuzzy-logic-controlled DFIG-based wind turbines. Applied Sciences, 8(1), 20.

[Hei 14] Heier, S. (2014). *Grid integration of wind energy: onshore and offshore conversion systems*. John Wiley & Sons.

-I-

[Idr 19] Idrissi, I., Chafouk, H., El Bachtiri, R., & Khanfara, M. (2019). Modeling and simulation of the variable speed wind turbine based on a doubly fed induction generator. In *Modeling of Turbomachines for Control and Diagnostic Applications*. IntechOpen.

[Izq 15] Izquierdo, L. R., Olaru, D., Izquierdo, S. S., Purchase, S., & Soutar, G. N. (2015). Fuzzy logic for social simulation using NetLogo. Journal of Artificial Societies and Social Simulation, 18(4), 1.

-J-

[Joh 29] Johannes, S. S. (1929). U.S. Patent No. 1,697,574. Washington, DC: U.S. Patent and Trademark Office.

[Jur 04] Jurado, F., & Valverde, M. (2004, May). Fuzzy logic control of a dynamic voltage restorer. In 2004 IEEE International Symposium on Industrial Electronics (Vol. 2, pp. 1047-1052). IEEE.

-L-

[Lag 11] Lagrioui, A., & Mahmoudi, H. (2011). Nonlinear adaptive backstepping control of permanent magnet synchronous motor (PMSM). *Journal of Theoretical and Applied Information Technology*, *29*(1), 1-9.

[Lui 17] Liu, H., Pan, Y., Li, S., & Chen, Y. (2017). Adaptive fuzzy backstepping control of fractional-order nonlinear systems. IEEE Transactions on Systems, Man, and Cybernetics: Systems, 47(8), 2209-2217.

[Lop 08] Lopez, J., Gubia, E., Sanchis, P., Roboam, X., &Marroyo, L. (2008). Wind turbines based on doubly fed induction generator under asymmetrical voltage dips. IEEE Transactions on Energy conversion, 23(1), 321-330.

[Lou 14] Luo, N., Vidal, Y., & Acho, L. (Eds.). (2014). *Wind turbine control and monitoring*. Basel, Switzerland: Springer International Publishing.

-M-

[Mak 15] Makhalas, K. A., & Alsehlli, F. (2015). Wind Power.

[Mar 03] Marques, J., Pinheiro, H., Gründling, H. A., Pinheiro, J. R., & Hey, H. L. (2003). A survey on variable-speed wind turbine system. *network*, *24*, 26.

[Mas 20] Masoumi, M., Hossani, S., Dehghani, F., & Masoumi, A. (2020). The Challenges and Advantages of Fuzzy Systems Applications. A Preprint, 1.

[Men 17] Mensou, S., Essadki, A., Minka, I., Nasser, T., & Idrissi, B. B. (2017, December). Backstepping controller for a variable wind speed energy conversion system based on a DFIG. In 2017 International Renewable and Sustainable Energy Conference (IRSEC) (pp. 1-6). IEEE.

[Men 18] Mensou, S., Essadki, A., Minka, I., Nasser, T., & Idrissi, B. B. (2018). Backstepping Controller for a Variable Wind Speed Energy Conversion System Based on a DFIG. *International Journal of Electrical and Computer Engineering*, *12*(9), 598-604.

[Moh 13] Mohammed, S. A., Abdel-Moamen, M. A., &Hasanin, B. (2013). Fuzzy logic controller based dynamic voltage restorer as voltage sag restorer and harmonics compensator. International Journal of Control, Automation and Systems, 2(3), 53-57.

-N-

[Nad 17] Nadour, M., Essadki, A., & Nasser, T. (2017). Comparative analysis between PI & backstepping control strategies of DFIG driven by wind turbine. *International Journal of Renewable Energy Research*, *7*(3), 1307-1316.

[Ngu19] Nguyen, A. T., Taniguchi, T., Eciolaza, L., Campos, V., Palhares, R., & Sugeno, M. (2019). Fuzzy control systems: Past, present and future. IEEE Computational Intelligence Magazine, 14(1), 56-68.

[Nia 11] Nian, H., Song, Y., Zhou, P., & He, Y. (2011). Improved direct power control of a wind turbine driven doubly fed induction generator during transient grid voltage unbalance. IEEE Transactions on Energy Conversion, 26(3), 976-986.

[Nit 18] Nitin. Tanwar. (2018). Fuzzy Sets and Their Applications in Pattern Recognition. Chapter-7, Project: Multidimensional poverty measurement in Haryana, 99-118.

-O-

[Omar 16] Omar, A. S. (2016). Application of fuzzy logic in qualitative performance measurement of Supply chain management (Doctoral dissertation, Computer Systems, JKUAT).

[Oua 20] Ouada, L., Benaggoune, S., & Belkacem, S. (2020). Neuro-fuzzy sliding mode controller based on a brushless doubly fed induction generator. *International Journal of Engineering*, *33*(2), 248-256.

-P-

[Per 05] Peri, V. M. (2005). Fuzzy logic controller for an autonomous mobile robot (Doctoral dissertation, Cleveland State University).

[Pra 07] Pratihar, D. K., & Hui, N. B. (2007). Evolution of fuzzy controllers and applications. In Advances in Evolutionary Computing for System Design (pp. 47-69). Springer, Berlin, Heidelberg.

[Puk 11] Pukdeboon, C. (2011). A review of fundamentals of Lyapunov theory. J. Appl. Sci, 10(2), 55-61.

-Q-

[Qua 95] Quality, O. P. (1995). Iscc. iieee recommended practice for monitoring electric power quality.

-R-

[Rad 15] Radha Krishna, T. Y., & Biswal, K. (2015). Speed Control of Separately Excited DC Motor using Fuzzy Logic Controller (Doctoral dissertation).

-S-

[Saa 14] Saad, M. M. M., & Asmuin, N. (2014). Comparison of horizontal axis wind turbines and vertical axis wind turbines. *IOSR Journal of Engineering (IOSRJEN)*, *4*(08), 27-30.

[Sad 22] Sadrehaghighi, I. (2022). Horizontal Axis Wind Turbines (HAWT) with Case Studies. *pp.1-111*.

[Sal 10] Salim, O. M., Zohdy, M. A., Dorrah, H. T., & Kamel, A. M. (2010). Application of Hyper-Fuzzy Logic in Field Oriented Control of Induction Machines. MEPCON'10, Cairo, Egypt, 356-363.

[Shu 21] Shukir, S. S. (2021). Comparison the performance of the dynamic voltage restorer based on PI, fuzzy logic, and fuzzy neural controller. International Journal of Engineering Management, 5(1), 1.

[Sinh 10] Sinha, R. K., Kumar, R., Venmathi, M., & Ramesh, L. (2010). Analysis of voltage sag with different DG for various faulty conditions. International Journal of computer communication and information system, 2(1), 189-193.

[Sing 11-1] Singh, M., & Santoso, S. (2011). *Dynamic models for wind turbines and wind power plants* (No. NREL/SR-5500-52780). National Renewable Energy Lab.(NREL), Golden, CO (United States).

[Sing 11-2] Singh, B., Jayaprakash, P., Kothari, D. P., & Chandra, A. (2011). New control algorithm for capacitor supported dynamic voltage restorer. Journal of Electromagnetic Analysis and Applications, 2011.

[Slo 91] Slotine, J. J. E., & Li, W. (1991). *Applied nonlinear control*. Englewood Cliffs, NJ: Prentice hall, *199*(1), 1-461.

[Soh 16] Sohoni, V., Gupta, S. C., & Nema, R. K. (2016). A critical review on wind turbine power curve modelling techniques and their applications in wind based energy systems. Journal of Energy, 2016.

[Sol 03] Soliman, S. A., El-Hawary, M. E., & Mantaway, A. H. (2003). Park's transformation application for power system harmonics identification and measurements. Electric Power Components and Systems, 31(8), 777-789.

[Sum 09] Sumper, A., Gomis-Bellmunt, O., Sudria-Andreu, A., Villafafila-Robles, R., & Rull-Duran, J. (2009). Response of fixed speed wind turbines to system frequency disturbances. *IEEE Transactions on Power Systems*, *24*(1), 181-192.

[Sur 19] Suresh, P., Pravin, A. A., Sreekanth, D. V., & Rajan, D. S. (2019). Numerical Analysis of Savonius Wind Turbine Using Fluid Dynamics. International Journal for Research in Applied Science & Engineering Technology (IJRASET), *7*(1),159-164.

-T-

[Tap 03] Tapia, A., Tapia, G., Ostolaza, J. X., & Saenz, J. R. (2003). Modeling and control of a wind turbine driven doubly fed induction generator. IEEE Transactions on energy conversion, 18(2), 194-204.

-W-

[Wan 15] Wang, C. (2015). A study of membership functions on mamdani-type fuzzy inference system for industrial decision-making. Lehigh University.

[Wes 10] Wessels, C., Gebhardt, F., & Fuchs, F. W. (2010). Fault ride-through of a DFIG wind turbine using a dynamic voltage restorer during symmetrical and asymmetrical grid faults. IEEE Transactions on power electronics, 26(3), 807-815.

-Y-

[Yu 18] Yu, S. S., Zhang, G., Fernando, T., & Iu, H. H. C. (2018). A DSE-based SMC method of sensorless DFIG wind turbines connected to power grids for energy extraction and power quality enhancement. *IEEE Access*, *6*, 76596-76605

-Z-

[Zhan 20] Zhang, S., Yong, E. M., Zhou, Y., & Qian, W. Q. (2020). Dynamic backstepping control for pure-feedback non-linear systems. IMA Journal of Mathematical Control and Information, 37(2), 674-697.